Fakultät für Physik der Technischen Universität München

Max-Planck-Institut für Physik
(Werner-Heisenberg-Institut)

Search for Neutral MSSM Higgs Bosons in $A/h/H \to \tau^+\tau^- \to e\mu + 4\nu$ Decays with the ATLAS Detector

Alessandro Manfredini

Vollständiger Abdruck der von der Fakultät für Physik der Technischen Universität München zur Erlangung des akademischen Grades eines

Doktors der Naturwissenschaften (Dr. rer. nat.)

genehmigten Dissertation.

Vorsitzender:		Univ.-Prof. Dr. B. Garbrecht
Prüfer der Dissertation:		
	1.	Priv.-Doz. Dr. H. Kroha
	2.	Univ.-Prof. Dr. L. Oberauer

Die Dissertation wurde am 22.7.2014 bei der Technischen Universität München eingereicht und durch die Fakultät für Physik am .... angenommen.

Abstract

In this thesis, a search for the neutral Higgs bosons of the Minimal Supersymmetric extension of the Standard Model has been performed with the ATLAS detector at the Large Hadron Collider (LHC). The search focuses on Higgs boson decays into a pair of τ leptons which subsequently decays via $\tau^+\tau^- \rightarrow e\mu + 4\nu$. The prospects for enhancing the sensitivity of this search by using jet reconstruction based on inner detector tracks has also been investigated.

The search for the neutral MSSM Higgs bosons A, h and H has been performed using proton-proton collision data at a centre-of-mass energy of 8 TeV corresponding to an integrated luminosity of $20.3\,\mathrm{fb}^{-1}$. To enhance the signal sensitivity, the events are split into two mutually exclusive categories without and with b-tagged jets indicating the two dominant Higgs boson production modes, via gluon fusion and in association with b-quarks, respectively. The results are interpreted in terms of the MSSM m_h^{mod} benchmark scenario. No significant excess of events above the estimated Standard Model background has been found. Upper limits have been derived in the plane of the two free MSSM parameters m_A and $\tan\beta$, where the latter is the ratio of the vacuum expectation values of the two MSSM Higgs doublets. Values of $\tan\beta \gtrsim 10$ are excluded in the mass range $90 < m_A < 200$ GeV. The most significant excess of events with a local p-value of 2.9% for the background only hypothesis is observed in the mass rage $250 < m_A < 300$ GeV, corresponding to a signal significance of $1.9\,\sigma$. In addition, less model-dependent upper limits on the cross section for the production of a generic scalar boson ϕ with mass m_ϕ via the processes $pp \rightarrow b\bar{b}\phi$ and $gg \rightarrow \phi$ have been derived.

The neutral MSSM Higgs boson production in association with b-quarks is characterised by the presence of low transverse momentum b-jets. The reconstruction and calibration of low transverse momentum jets based on energy deposits in the calorimeters is strongly affected by pile-up effects due to the multiple proton interactions per bunch crossing. An alternative approach employing jet reconstruction based on inner detector tracks have been investigated. For jets with low transverse momenta the track-based reconstruction provides a higher jet reconstruction efficiency compared to calorimeter-based one and is more suitable for the identification of low momentum b-jets. This preliminary study shows that the sensitivity of the search for neutral MSSM Higgs bosons, produced in association with b-quarks, can be improved by up to a factor of two if track-based jet reconstruction is employed instead of the canonical calorimeter-based one. However, additional studies are needed to fully evaluate the systematic uncertainties of track-based jets reconstruction. Furthermore a dedicated calibration of the b-jet identification and mis-identification rates is necessary to complete the study.

To my friends of Munich:

Sebastian N., Sebastian P.
Takeshi T., Shang-yu S.,
Ana S.B., Marlene E.
Sergey A.

Contents

1. Introduction

The Standard Model (SM) of particle physics describes the strong and electroweak interactions of quarks and leptons and has been confirmed extremely well by experiments at energy scales below about 1 TeV. The interactions between the elementary constituents of matter are mediated by gauge bosons based on the principle of local gauge invariance. Masses for all these particles are introduced without spoiling the electroweak gauge symmetry via the mechanism of spontaneous symmetry breaking. An additional complex scalar field is required for this purpose which give rise to a new scalar particle, the Higgs boson.

The recent discovery at the Large Hadron Collider (LHC) of a new boson of mass of about 125 GeV by the ATLAS and CMS experiments [1,2] is in agreement with the Higgs boson prediction by the SM. The measurements of its properties [3–6] are well compatible with those of the SM Higgs boson. However, the question remains whether this new particle is the only missing piece of the electroweak symmetry breaking sector or whether it is one of several Higgs bosons as predicted by many models beyond the SM. Supersymmetric extension of the SM are theoretically favoured since they offer an elegant solution to limitations of the SM. The minimal supersymmetric extension of the SM (MSSM) predicts the existence of five Higgs bosons, two of them neutral and CP-even (h and H), one neutral and CP-odd (A) and two charged ($H^{\pm}$). In this thesis, a search for the neutral MSSM Higgs bosons is performed with $20.3\,\text{fb}^{-1}$ of proton-proton collision data at a centre-of-mass energy of 8 TeV recorded by the ATLAS experiment at the LHC. Chapter 2 is devoted to an introduction to the MSSM focusing on the Higgs sector and on the neutral MSSM Higgs boson phenomenology.

An overview of the ATLAS experiment is given in Chapter 3. The ATLAS detector consist of four main sub-detectors, the inner detector, the electromagnetic and hadronic calorimeters and the muon spectrometer. These sub-detectors are installed cylindrically around the beam pipe in the central barrel part and in disks in the end-caps which are symmetrical in forward and backward direction with respect to the proton beams. The data recorded by the ATLAS experiment undergo several steps of offline reconstruction before being ready for analysis. The physics object reconstruction and data quality criteria used in this thesis are described in Chapter 4.

In Chapter 5, the search for the neutral MSSM Higgs bosons performed in $A/h/H \rightarrow \tau^+\tau^- \rightarrow e\mu{+}4\nu$ decays is discussed. This final state corresponds to 6% of the total decay rate of the two τ leptons. In spite of the rather small branching fraction, this final state provides a signal sensitivity which is competitive with the other channels, especially for low Higgs boson masses, because of the high background rejection. The events are split into two mutually exclusive categories based on the presence or absence of b-tagged jets indicating the two main Higgs production modes, in association with b-quarks and via gluon fusion, respectively.

The Higgs boson production in association with b-quarks is characterised by the presence of low transverse momentum b-jets. The reconstruction and calibration of low transverse momenta jets from energy deposits in the calorimeters are strongly deteriorated by pile-up effects of multiple proton interactions per bunch crossing, causing a large loss of efficiency for the $A/h/H$ search in the b-tagged category. As an alternative, jet reconstruction based on inner detector tracks has been studied for the purpose of b-tagging. The inner detector tracks are associated to their original interaction vertex which makes track-based jet reconstruction more robust against pile-up effects than calorimeter-based jets. A study on the prospects for enhancing the sensitivity of the neutral MSSM Higgs boson search by using track-based b-jet identification is presented in Chapter 6.

A summary of the neutral MSSM Higgs boson search and of the prospects for its improvement by employing track-based jet reconstruction is given in Chapter 7.

2. Higgs Bosons in Standard Model and MSSM

In this chapter, the theoretical concepts relevant for the experimental search presented in this thesis are introduced. A brief overview of the Standard Model of particle physics is given in Section 2.1 based on reference [7]. Among the extensions of the Standard Model, the minimal supersymmetric extension (MSSM) is theoretically favoured as one of the most predictive scenarios. The MSSM is introduced in Section 2.2 with emphasis on the Higgs boson sector based on references [8,9]. Finally, a review of the phenomenological aspects of the MSSM Higgs boson production and decays is given in Section 2.3 based on reference [10].

2.1. The Standard Model of Particle Physics

2.1.1. Introduction

A detailed description of the Standard Model (SM) of particle physics can be found in reference [12]. A brief overview is given below.

The SM of particle physics describes the interactions of the known fermionic matter particles, quarks and leptons, via the strong, the electromagnetic and the weak forces based on the principle of local gauge invariance, i.e. invariance under phase transformations depending on the space-time coordinates. The gravitational force is negligible in atomic and nuclear physics since quantum gravity effects are expected only at very high energies at the Planck scale of $\sim 10^{19}$ GeV.

The gauge symmetries of the SM are described by the group $SU(3)_c \otimes SU(2)_L \otimes U(1)_Y$ which has $8+3+1=12$ generators and gauge fields. The electromagnetic and weak interactions [13–15] are described by the $SU(2)_L \otimes U(1)_Y$ symmetry group, while $SU(3)_c$ is the group of the strong colour forces of Quantum Chromodynamics (QCD) [16]. A vector boson is associated to each generator of the gauge symmetry groups of the SM acting as mediator of the interaction. Eight gluons are associated to the $SU(3)_c$ colour group, while four gauge bosons, $W^{\pm}$, Z^0 and γ, are associated to the electroweak symmetry $SU(2)_L \otimes U(1)_Y$. The gluons and the photon are massless while the remaining weak gauge bosons have mass. These masses are introduced without spoiling the electroweak gauge symmetry via the mechanism of spontaneous symmetry breaking [17–21], an additional complex scalar field is required for this purpose and give rise to a new scalar particle, the Higgs boson, which interacts with other particles with a strength proportional to their masses.

Quarks are subject to all SM interactions. Each quark flavour is a colour triplet and carries electroweak charges including electric charges of $+2/3$ and $-1/3$ for up-type and down-type quarks respectively. Leptons are colourless but have electroweak charges. The electrons, muons and τ leptons carry electric charge -1, while the associated neutrinos ν_e, ν_μ and ν_τ are electrically neutral. Opposite sign electric charges are carried by the respective anti-particles. Quarks and leptons group in three “generations” with equal charge quantum numbers but increasing masses.

2.1.2. The Higgs Mechanism in the SM

The Higgs mechanism extends the Standard Model by a complex scalar field Φ, in its minimal realisation [17–21] one scalar $SU(2)_L$ doublet

$$\Phi = \begin{pmatrix} \phi^+ \\ \phi^0 \end{pmatrix} \tag{2.1}$$

with four degrees of freedom and weak hypercharge $Y = +1$ is introduced. The Higgs potential

$$V(\Phi) = \mu^2 \Phi^\dagger \Phi + \lambda (\Phi^\dagger \Phi)^2 \,, \tag{2.2}$$

with the mass parameter μ and self coupling λ is invariant under $SU(2)_L \otimes U(1)_Y$ symmetry transformations. For $\mu^2 < 0$ the scalar field has an infinite set of degenerate ground states. If a non vanishing vacuum expectation value is chosen for the neutral component of the scalar filed Φ, the $SU(2)_L \otimes U(1)_Y$ symmetry is spontaneously broken with the electromagnetic gauge symmetry $U(1)_Q$ remaining as a symmetry of the ground state. Therefore, three of the original four degrees of freedom of the scalar field are absorbed as longitudinal polarisation states of the $W^\pm$ and Z bosons, which in this way acquire their masses, while the photon remains massless. The remaining degree of freedom corresponds to a physical massive scalar particle, the Higgs boson.

The masses of the fermions can be generated by means of Yukawa couplings to the Higgs field Φ [22].

2.1.3. Precision Tests and Limitations of the SM

The Standard Model has been successfully tested in a vast number of experiments over a wide range of energies during the last decades. Precision tests of the electroweak theory performed at LEP, SLC and Tevatron accelerators [25] confirmed that the couplings of quark and leptons to the weak gauge bosons $W^\pm$ and Z fully agree with the predictions of the SM. Due to the high experimental accuracy of the per-mille level, not only the tree-level predictions, but also the impact of quantum corrections have been verified. Measurements of weak hadron decays together with several other experimental results [24] provide additional tests of the Standard Model at low energies. The recent discovery at the LHC of a Higgs boson with a mass of about 125 GeV [1, 2] is another success of the SM. The measured mass is in agreement with the allowed range from the combined measurement of electroweak observables [26]. The spin and coupling strength of the new boson are also in good agreement with the SM predictions for the measured mass.

Tension between the SM predictions and experimental data is found for only very few observables. The most significant discrepancies, of slightly above three standard deviations, are observed for the anomalous magnetic moment of the muon a_μ [27] and for the forward-backward asymmetry in bottom quark production at LEP [25] and in the top quark production at the Tevatron [28].

In spite of this success, the Standard Model is conceptually unsatisfactory due to a number of deficiencies and is widely believed to be an effective theory valid only for energies up to the electroweak scale. In addition to the fact that the SM does not include the gravitational force, it does not explain the pattern of fermion masses and, in its simplest version, does not allow for neutrino masses, the theory has other deficiencies indicating the need for new physics beyond the Standard Model (BSM). Some of the most important are discussed below.

Hierarchy and Fine-Tuning Problem The radiative corrections to the Higgs boson mass introduce quadratic divergences in the cut-off energy scale Λ up to which the theory is considered to be valid [29]. If the cut-off scale chosen is the Planck scale or the GUT scale (see below), a fine tuning of the higher order corrections is needed with an unnaturally high precision of $\mathcal{O}(10^{-30})$ to give a Higgs boson mass near the electroweak scale $\mathcal{O}(100\,GeV)$ as measured [30–32].

Dark Matter The SM does not contain a particle candidate for the observed large contribution of dark non-barionic matter to the energy density of the Universe [33–35]. Dark matter candidates have to be massive, stable and only weakly interacting particles.

Gauge Unification Problem Another unsatisfactory aspect of the SM is that the electroweak and strong gauge couplings do not evolve to the same value at high energies. Motivated by the successful unification of electromagnetic and weak interaction, the existence of a Grand Unified Theory (GUT) has been suggested [36, 37], which predicts the unification of the three gauge symmetries of the SM in a single gauge group with just one coupling constant at the GUT energy scale of about 10^{16} GeV.

Among many possible extensions of the SM, supersymmetry is theoretically favoured as it provides natural solutions to the above problems. As discussed in Section 2.2, it can solve the hierarchy problem, provide a suitable dark matter particle candidate and predicts unification of the three SM gauge couplings at the GUT scale.

2.2. The Minimal Supersymmetric Standard Model

2.2.1. Introduction to the MSSM

Supersymmetry (SUSY) [38–40] was first introduced in the 1970s as a new symmetry relating fermions and bosons. The SUSY generators $\mathcal{Q}$ transform fermion fields into boson and vice versa:

$$\mathcal{Q}|\text{Fermion}\rangle = |\text{Boson}\rangle, \quad \mathcal{Q}|\text{Boson}\rangle = |\text{Fermion}\rangle\,. \tag{2.3}$$

In a supersymmetric extension of the SM, each of the known fundamental particle states is either in a chiral or gauge *supermultiplet* together with a superpartner with spin differing by unit 1/2.

SUSY naturally solves the hierarchy problem since the quadratically divergent loop contributions to the Higgs mass from SM particles are cancelled by loop contributions from the superpartners. The quark and lepton superpartners are labelled by adding an “s” in front of the name, standing for scalar. The SM gauge bosons also have spin-1/2 partners named by adding “ino” as suffix to the name. The symbol of superpartners results from adding “(˜)” to the SM symbol. The SUSY particles share the same couplings with their SM partners. Since the left- and right-handed components of fermions shows to transform differently under the weak $SU(2)$ gauge symmetry, their superpartner inherit this feature.

The minimal supersymmetric extension of the Standard Model (MSSM) [41–46], is defined by requiring the minimal gauge group as in the SM and minimal particle content: the three generations of fermions (without right-handed neutrinos) and

Table 2.1.: The chiral supermultiplets of the first generation in the minimal supersymmetric Standard Model (see ref. [8]). The spin-0 fields are complex scalars and the spin-1/2 left-handed two-component Weyl spinors.

Names	Supermultiplets	Spin 1/2	Spin 0
quarks, squarks	Q	$(u_L\ d_L)$	$(\tilde{u}_L\ \tilde{d}_L)$
	$\bar{u}$	$u_R^\dagger$	$\tilde{u}_R^*$
	$\bar{d}$	$d_R^\dagger$	$\tilde{d}_R^*$
leptons, sleptons	L	$(\nu\ e_L)$	$(\tilde{\nu}\ \tilde{e}_L)$
	$\bar{e}$	$e_R^\dagger$	$\tilde{e}_R^*$
Higgs bosons, Higgsinos	H_1	$(\tilde{H}_1^0\ \tilde{H}_1^-)$	$(H_1^0\ H_1^-)$
	H_1	$(\tilde{H}_2^+\ \tilde{H}_2^0)$	$(H_2^+\ H_2^0)$

gauge bosons of the SM and two Higgs doublets with their superpartners. The chiral and gauge supermultiplets of the MSSM are listed in Tables 2.1 and 2.2, respectively. The superpartners of the Higgs bosons, the *higgsinos*, the *wino* and *bino* mix with each other resulting in the following mass eigenstates: two charginos $\chi_{1,2}^{\pm}$ and four neutralinos $\chi_{1,2,3,4}^{0}$.

R-parity conservation

The MSSM requires an additional discrete and multiplicative symmetry called R-parity [40] which ensures the baryon and lepton number conservation. The R-parity quantum number is defined by:

$$R_p = (-1)^{2s+3B-L}\,, \tag{2.4}$$

where L and B are the lepton and baryon numbers and s the spin quantum number. The R-parity quantum number has a value of +1 for ordinary SM particles and of −1 for their superpartners. This symmetry was originally introduced as

Table 2.2.: The gauge supermultiplets in the minimal supersymmetric Standard Model (see ref. [8]).

Names	Supermultiplets	Spin 1	Spin 1/2
gluons, gluinos	G_a (a =1,...,8)	g	$\tilde{g}$
W bosons, winos	W_a (a=1,...,3)	$W^{\pm}$, W^0	$\tilde{W}^{\pm}$, $\tilde{W}^0$
B boson, bino	B	B^0	$\tilde{B}^0$

a simple solution to prevent fast proton decay. Lepton and baryon number violation usually leads to proton decays via supersymmetric particle exchange with a life-time shorter than the experimental lower bound. R-parity conservation has also other important phenomenological consequences: SUSY particles are always produced in pairs and decay into an odd number of SUSY particles. Furthermore, the lightest SUSY particle, often chosen to be one of the neutralinos, is stable and therefore is a candidate for the dark matter.

The Soft SUSY Breaking

If supersymmetry is an exact symmetry of nature, the SM particles and their corresponding superpartners have the same mass. However, SUSY particles have not yet been observed, suggesting that these particles, if they exist, must be much heavier than their SM partners, leading the breaking of supersymmetry at low energies. To achieve SUSY breaking without reintroducing the quadratic divergences in the Higgs mass radiative corrections, so called “soft” SUSY breaking terms are introduced in the Lagrangian [47, 48]. These terms introduce explicitly the mass terms for the higgsinos, gauginos and sfermions as well as tri-linear coupling terms between sfermions and higgsinos. In general, if generation mixing and complex phases are allowed, the soft SUSY breaking terms introduce a large number of unknown parameters (about 125) [49]. However, in the absence of such phases and mixing, and by requiring the soft terms to obey certain boundary conditions [47,48], the number of free parameters can be strongly reduced by an order of magnitude.

2.2.2. The Higgs Sector of the MSSM

In the MSSM, two $SU(2)_L$ doublets of complex scalar fields of opposite hypercharge are required to break the electroweak symmetry. This requirement is necessary to separately generate the masses of up-type and down-type fermions [39, 50, 51] and to cancel chiral anomalies that otherwise would spoil the renormalizability of the theory [52]. The two Higgs doublets are

$$H_1 = \begin{pmatrix} H_1^0 \\ H_1^- \end{pmatrix} \text{ with } Y_{H_1} = -1, \quad \text{and} \quad H_2 = \begin{pmatrix} H_2^+ \\ H_2^0 \end{pmatrix} \text{ with } Y_{H_2} = +1\,. \tag{2.5}$$

The Higgs mechanism in the MSSM [41, 53] is similar to the one in the SM. Non vanishing vacuum expectation values of the neutral components of the two Higgs doublets

$$\langle H_1^0 \rangle = \frac{v_1}{\sqrt{2}}, \quad \text{and} \quad \langle H_2^0 \rangle = \frac{v_2}{\sqrt{2}}\,, \tag{2.6}$$

break the $SU(2)_L \otimes U(1)_Y$ symmetry while preserving the electromagnetic symmetry $U(1)_Q$. Three of the original eight degrees of freedom of the scalar fields are absorbed as longitudinal polarization states of the $W^\pm$ and Z bosons, which in this way acquire their masses. The remaining degrees of freedom correspond to five physical Higgs bosons: two neutral CP-even bosons h and H, a neutral CP-odd boson A and a pair of charged bosons $H^\pm$.

The MSSM Higgs sector is described by six parameters: the Higgs bosons masses m_h, m_H, m_A, $m_{H^\pm}$, the mixing angle α of the neutral CP-even Higgs bosons and the ratio between the two vacuum expectation values $\tan\beta = v_1/v_2$. At tree level, only two of these parameters are independent, commonly chosen to be $\tan\beta$ and m_A. Supersymmetry imposes a strong hierarchical structure of the Higgs boson mass spectrum: where h is the lightest boson with $m_h < M_Z$ at three level, while $m_A < m_H$ and $M_{H^\pm}^2 = m_A^2 M_W^2$. Furthermore, the following relation holds between the mixing angles:

$$\cos^2(\beta - \alpha) = \frac{m_h^2(M_Z^2 - m_h^2)}{m_A^2(m_H^2 - m_h^2)}\,. \tag{2.7}$$

These relations are broken by large radiative corrections to the Higgs bosons masses [54] which raise the upper bound on the h boson mass from M_Z to about 140 GeV. In addition, the requirement of gauge coupling unification restricts $\tan\beta$ to the range $1 \lesssim \tan\beta \lesssim m_t/m_b$ [55].

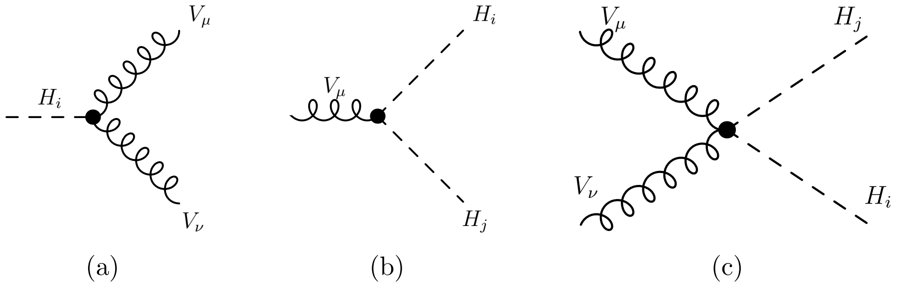

Figure 2.1.: Feynman diagrams for the couplings of (a) one Higgs boson and two gauge boson fields, (b) two Higgs bosons and one gauge boson and (c) two Higgs bosons and two gauge bosons in the MSSM [9].

2.3. Phenomenology of the Neutral MSSM Higgs Bosons

2.3.1. MSSM Higgs Bosons Couplings to SM Particles

The phenomenology of the MSSM Higgs bosons depends on their couplings to the Standard Model and to supersymmetric particles. A short overview of the former is given below based on the ref. [9]. Supersymmetric particles are assumed to be too heavy for direct Higgs bosons decays into them.

The possible couplings between the MSSM Higgs bosons and vector bosons are shown in Figure 2.1. There are the tri-linear couplings $V_\mu V_\nu H_i$ and $V_\mu H_i H_j$ of one Higgs boson and two gauge bosons and of one gauge boson and two Higgs bosons, respectively, as well as quartic couplings $V_\mu V_\nu H_i H_j$ between two Higgs bosons and two gauge bosons. The most relevant coupling for MSSM Higgs boson phenomenology is the tri-linear coupling $V_\mu V_\nu H_i$. Since the photon is massless, there are no Higgs-$\gamma\gamma$ and Higgs-$Z\gamma$ couplings at tree level. CP-invariance also forbids WWA, ZZA and $WZH^\pm$ couplings. Therefore, for the tri-linear coupling $V_\mu V_\nu H_i$ only the following terms remain:

$$Z_\mu Z_\nu h \sim ig_z M_Z \sin(\beta-\alpha) g_{\mu\nu}, \qquad Z_\mu Z_\nu H \sim ig_z M_Z \cos(\beta-\alpha) g_{\mu\nu}\,. \tag{2.8}$$

$$W_\mu^+ W_\nu^- h \sim ig_w M_W \sin(\beta-\alpha) g_{\mu\nu}, \quad W_\mu^+ W_\nu^- H \sim ig_w M_W \cos(\beta-\alpha) g_{\mu\nu}\,. \tag{2.9}$$

The coupling strengths G_{VVh} and G_{VVH} of the neutral CP-even Higgs bosons h and H to a pair of vector bosons are proportional to $\sin(\beta-\alpha)$ and $\cos(\beta-\alpha)$ respectively, where $\cos(\beta-\alpha)$ is given at tree level by equation (2.7). The following relationship holds

$$G^2_{VVh} + G^2_{VVH} = g^2_{VVH_{SM}} \tag{2.10}$$

with the SM Higgs boson coupling $g_{VVH_{SM}}$ and has interesting phenomenological consequences. Equations (2.8)-(2.10) imply that the coupling of h (H) to vector bosons increases (decreases) with $\tan\beta$. For relatively large values[1] of $\tan\beta$, h has SM-like couplings to vector bosons while H virtually decouples from them. An overview of the coupling properties of vector bosons with neutral and charged Higgs bosons, of the tri-linear and quartic couplings among Higgs bosons and of the couplings to SUSY particles is given in [9].

The couplings of the MSSM Higgs bosons to the up-type (u) and down-type (d) fermions also depend on $\tan\beta$ as follows:

$$\begin{aligned} G_{huu} &\propto m_u[\sin(\beta-\alpha)+\cot\beta\cos(\beta-\alpha)], & G_{hdd} &\propto m_u[\sin(\beta-\alpha)-\tan\beta\cos(\beta-\alpha)]\,, \\ G_{Huu} &\propto m_u[\cos(\beta-\alpha)-\cot\beta\sin(\beta-\alpha)], & G_{Hdd} &\propto m_d[\cos(\beta-\alpha)+\tan\beta\sin(\beta-\alpha)]\,, \\ G_{Auu} &\propto m_u\cot\beta, & G_{Add} &\propto m_d\tan\beta\,. \end{aligned}$$

The couplings of either the h or H boson to down-type (up-type) fermions is enhanced (suppressed) by a factor $\tan\beta$ depending on the magnitude of $\cos(\beta-\alpha)$ or $\sin(\beta-\alpha)$, while the coupling of the A boson to down-type (up-type) fermions is directly enhanced (suppressed) by $\tan\beta$.

2.3.2. MSSM Benchmark Scenarios

At tree level, the MSSM Higgs boson masses, decay branching fractions and production cross sections are all determined by two independent parameters, which by convention are chosen to be m_A and $\tan\beta$. As pointed out in Section 2.2.2, the MSSM Higgs bosons masses are strongly affected by radiative corrections which introduce dependence of physics observables on additional MSSM parameters [54]. The main corrections arise from the top-stop (s)quark sector. For large $\tan\beta$ values, also the bottom-sbottom (s)quark sector becomes increasingly important.

---

[1] For most scenarios this is valid for $\tan\beta \gtrsim 10$ large range of m_A.

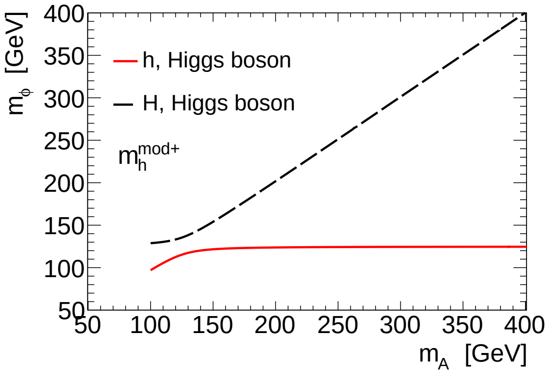

Figure 2.2.: Prediction for the mass of H and h bosons as a function of the mass of the A boson in the m_h^{mod+} scenario with $\tan\beta = 10$.

Furthermore, the corrections depend on the SUSY-breaking scale M_{SUSY}, the trilinear Higgs-stop and Higgs-sbottom Yukawa couplings and on the electroweak gaugino and gluino masses.

Due to the large number of free parameters, a complete scan of the MSSM parameter space is not practical. To cope with this difficulty, several benchmark scenarios have been proposed [10, 57], which define specific values of the SUSY parameters entering the predictions via radiative corrections and leading to characteristic phenomenological features. The parameters m_A and $\tan\beta$ are left free and the results are presented in the $m_A - \tan\beta$ plane.

The m_h^{max} benchmark scenario [56] has been used frequently in the past for neutral MSSM Higgs bosons searches at LEP, Tevatron and the LHC [71–74]. In this scenario, the MSSM parameters are fixed such that the mass m_h of the light CP-even Higgs boson assumes its maximum value as a function of m_A and $\tan\beta$. The m_h^{max} scenario allows for setting conservative lower bounds on the values of m_A, $m_H^{\pm}$ and $\tan\beta$ [57]. However, after the recent discovery of a Higgs boson with mass of about 125 GeV, this scenario predicts a too heavy SM-like Higgs boson h, thus becoming inconsistent with the Higgs boson observation in large regions of the MSSM parameter space. This scenario is now only used for comparison with the result of previous experiments.

Recently, several new benchmark scenarios have been proposed [10] to accommodate the experimental constraints from previous searches for neutral MSSM Higgs bosons and from the observation of a SM-like Higgs boson at the LHC.

An interesting updated benchmark scenario is the m_h^{mod} scenario which predicts $m_h \simeq 125.5 \pm 3$ GeV in a large region of the MSSM parameter space, Figure 2.2 shows the prediction for the mass of H and h bosons as a function of the mass of the A boson in the m_h^{mod} scenario. The m_h^{mod} scenario is obtained by reducing the amount of mixing in the stop sector (between the electroweak eigenstate) with respect to the m_h^{max} scenario. This is possible for both signs of the MSSM parameter X_t, which determinates the amount of stop mixing, giving rise to two complementary scenarios m_h^{mod+} and m_h^{mod-} . The difference between these two scenarios is found to be negligible for experimental searches and the m_h^{mod+} benchmark scenario has been used throughout this thesis as a reference. For simplicity, the m_h^{mod+} scenario is referred in the following to as m_h^{mod}.

Other interesting benchmark scenarios are the light-stop and the light-stau scenario. The first alters the gluon fusion production cross section, while the second leads to a modification of the branching fraction of the decays of the MSSM Higgs boson h into two photons. An overview of the different benchmark scenarios is given in reference [10].

2.3.3. Production and Decay of Neutral MSSM Higgs Bosons at the LHC

The MSSM predicts in large regions of its parameter space a Higgs boson with SM-like couplings. The requirement on this boson to have a mass of about 125 GeV and to be compatible with the previous searches puts stringent constraints on the MSSM parameter space. Scenarios interpreting the discovered SM-like Higgs boson as the lightest CP-even MSSM Higgs boson h are favoured since they have a relatively large region of parameter space still unexplored. This approach is adopted in this thesis.

From the discussion of the Higgs bosons couplings in Section 2.3.1, it turns out that the MSSM Higgs bosons H and A tend to be degenerate in mass and to decouple from gauge bosons. Furthermore their couplings to down-type (up-type) fermions are enhanced (suppressed) proportional to $\tan\beta$ depending on $\cos(\beta-\alpha)$. Therefore, for large $\tan\beta$, bottom-quarks and τ-leptons play an important role in the production and decays of the H and A Higgs bosons compared to the SM Higgs boson case.

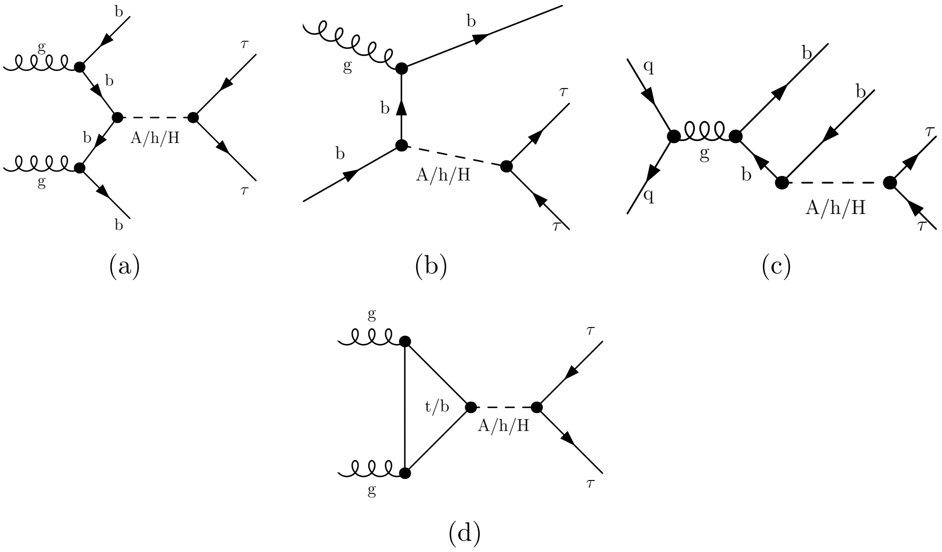

(a) (b) (c)

(d)

Figure 2.3.: Tree-level Feynman diagrams for the production of the neutral MSSM Higgs bosons in association with b-quarks (a,b,c) and via gluon fusion (d) with subsequent Higgs boson decays into a pair of τ leptons.

The production of the neutral CP-even MSSM Higgs bosons h and H at hadron colliders proceeds via the same processes as for the SM Higgs boson production [11]. The pseudoscalar boson A, instead, cannot be produced in association with gauge bosons or through vector boson fusion (VBF) at tree-level as the coupling gauge bosons is forbidden by CP-invariance. At the LHC, the dominant neutral MSSM Higgs boson production mechanisms are gluon fusion, $gg \to A/H/h$, and the production in association with b-quarks, $pp \to b(b)A/h/H$. The latter becomes important for relatively large values of $\tan\beta$ ($\tan\beta \gtrsim 10$). Figure 2.3 shows examples of tree-level Feynman diagrams for these processes. The corresponding production cross sections are shown in Figure 2.4 s a function of the A boson mass assuming the m_h^{max} benchmark scenario.

The branching fractions for decays of the neutral MSSM Higgs boson h are the same as for the SM Higgs boson (under the assumption that all supersymmetric particle are too heavy) while for H and A decays into τ leptons, studied in this thesis, dominate after decays to $b\bar{b}$ in large regions of the parameter space. Figure 2.5 shows the branching fractions for various decays of h, H and A as a function of m_A for two values of $\tan\beta$ in the m_h^{mod+} benchmark scenario.

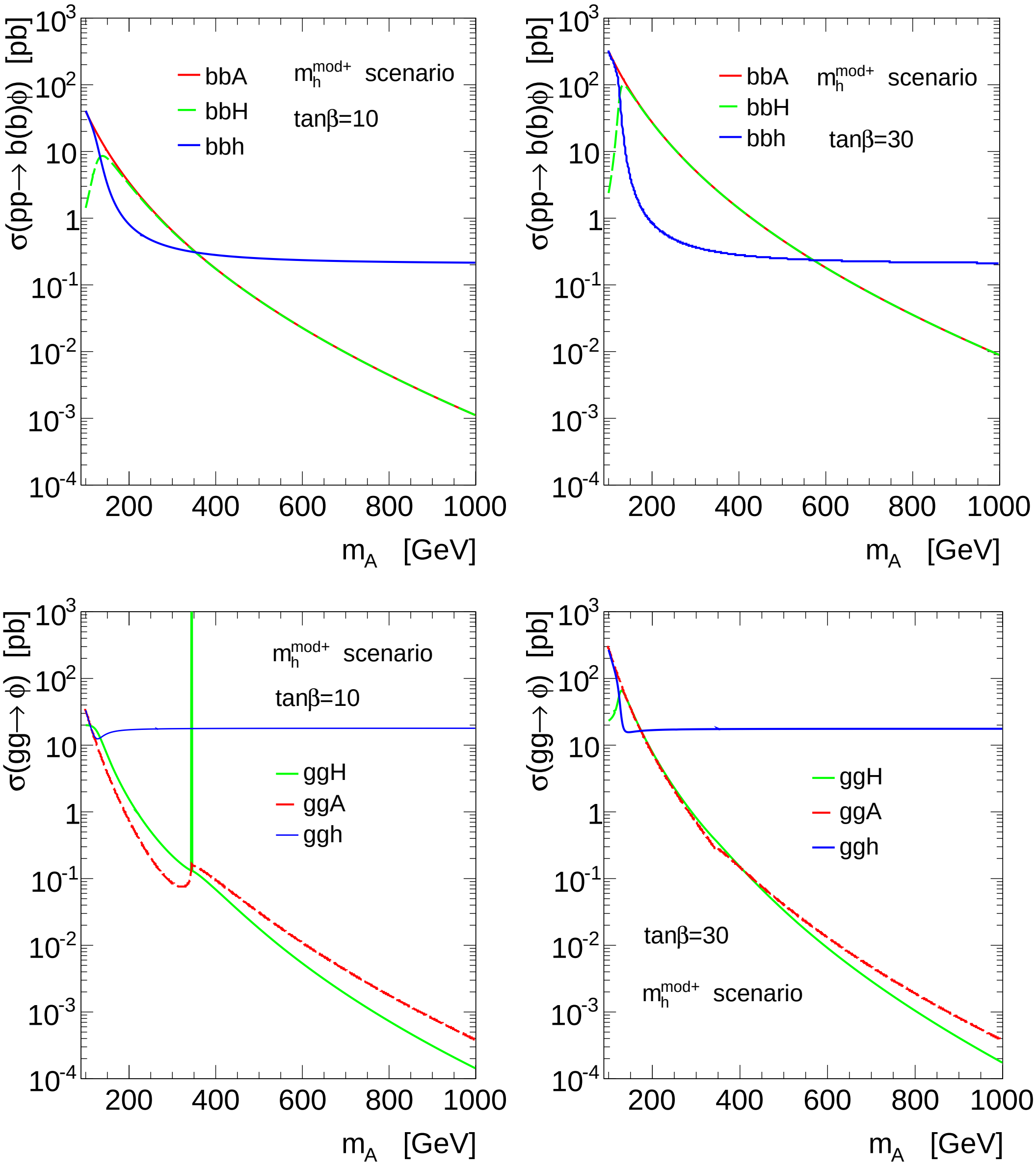

Figure 2.4.: Predictions of the total cross section for MSSM Higgs bosons production via gluon fusion and in association with bottom quarks at $\sqrt{s} = 8$ TeV using NNLO calculations and NLO MSTW2008 parton density functions of the proton, in the m_h^{mod} scenario for (left) $\tan\beta = 10$ and (right) $\tan\beta = 30$ [11].

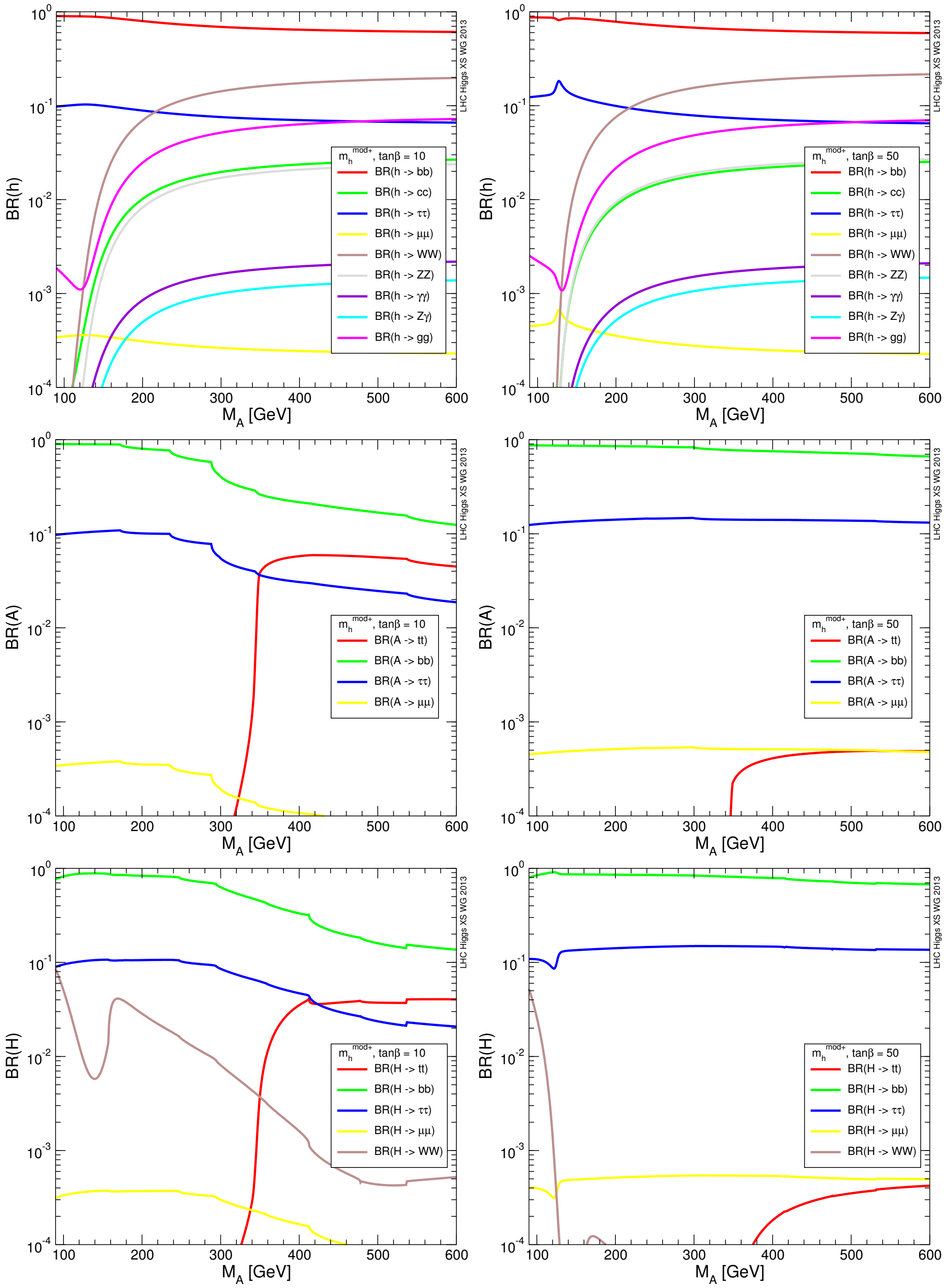

Figure 2.5.: Branching fractions of decays of the neutral MSSM Higgs bosons $h/H/A$ in the m_h^{mod+} scenario for $\tan\beta = 10$ (left) and $\tan\beta = 50$ (right) [10].

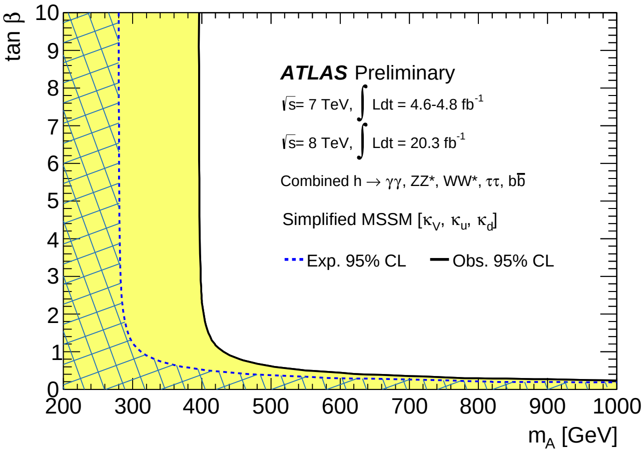

Figure 2.6.: Regions of the $m_A - \tan\beta$ plane of a simplified MSSM model [59, 60] excluded by fits of Higgs couplings (k_V and $k_{u,d}$ to vector bosons and up- and down-type fermions, respectively) to the measured Higgs boson production and decays rates. The the observed (shaded) and expected (hashed) exclusions limits at a 95% confidence level [58] are shown.

2.3.4. Status of the Search for Neutral MSSM Higgs Bosons

Constraint of the MSSM Higgs sector may be obtained in two ways: by the measure of the couplings of the observed SM-like Higgs boson to known SM particles or by direct searches for additional Higgs bosons in a well defined scenario.

In case the discovered SM-like Higgs boson with a mass of about 125 GeV is interpreted as the light CP-even Higgs boson of the MSSM, the couplings of the Higgs boson to vector bosons (k_V), up-type fermions (k_u) and down-type fermions (k_d), can be expressed as a function of m_A and $\tan\beta$ allowing to exclude certain region of the $m_A - \tan\beta$ plane [58]. Figure 2.6 shows the excluded parameter region for a so-called "simplified MSSM" model [59,60] obtained from the fits of the Higgs boson production and decay rates to the corresponding observed values.

The latest constraints on $m_A - \tan\beta$ plane from direct searches for neutral MSSM Higgs bosons searches at ATLAS [61] and CMS [73] are shown in Figure 2.7.

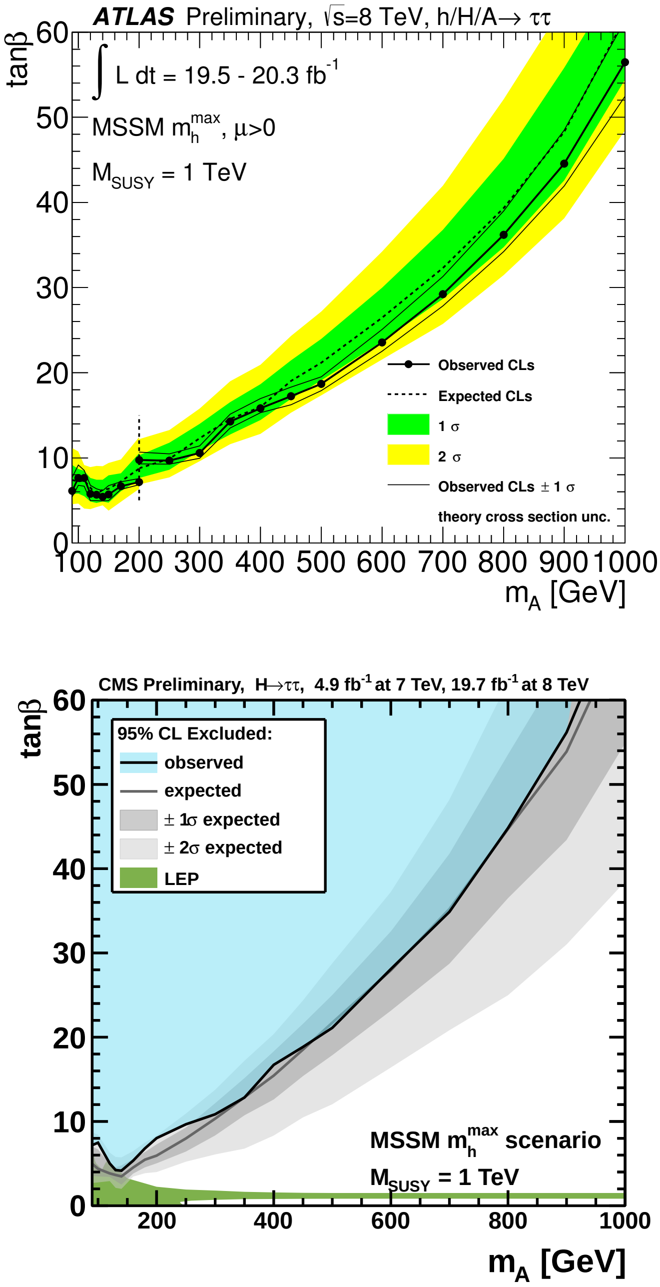

Figure 2.7.: Expected and observed limits 95% confidence level upper limits on $\tan\beta$ as a function of m_A in the m_h^{max} scenario from (top) the ATLAS [61] and (bottom) CMS [73] experiments.

3. The ATLAS Detector at the LHC

The Large Hadron Collider (LHC) located at the European Organisation for Nuclear Research (CERN) in Geneva, Switzerland, is the largest particle collider facility in the world, colliding protons and heavy ions at the so far largest centre-of-mass energies. The ATLAS experiment is one of the experiments at the LHC designed to search for a wide range of new physics phenomena and to perform precision measurements of Standard Model processes. Proton-proton collision data recorded by the ATLAS detector in 2012 has been used for the search for the neutral MSSM Higgs bosons presented in this thesis.

The chapter is organised as follows: the design and performance of the LHC are summarised in Section 3.1, based on [62], while the ATLAS detector is described in Section 3.2, based on [63].

3.1. The Large Hadron Collider

The LHC is a hadron synchrotron collider with superconducting magnets. It is installed in the tunnel of the former Large Electron-Positron collider (LEP) with a circumference of about 27 km. LHC is designed to collide proton beams at a centre-of-mass energy of 14 TeV and an unprecedented peak luminosity of 10^{34} $\text{cm}^{-2}\text{s}^{-1}$. It can also collide heavy ion (lead) beams carrying an energy of 2.8 TeV per nucleon at a peak luminosity of 10^{27} $\text{cm}^{-2}\text{s}^{-1}$.

Figure 3.1 shows the layout of the CERN accelerator complex. The protons undergo several acceleration steps before injection into the LHC machine. A linear accelerator (*Linac* 2) brings the protons to an energy of 50 MeV at which they are injected into the *Booster* where they are further accelerated to 1.4 GeV. The proton energy is successively increased to 25 GeV and to 450 GeV in the *Proton Synchrotron* (PS) and the *Super Proton Synchrotron* (SPS), respectively. Finally the protons are injected in two opposite directions into the LHC ring where they reach their final energy.

The proton beams are housed in two separate vacuum pipes and consist of up to 2835 proton bunches, each of them containing about 10^{11} protons. Radiofrequency cavities are employed to accelerate the protons while superconducting magnets bend and focus the beams. The nominal bunch spacing allows for bunch crossings every 25 ns which represents a challenge for the detector read-out electronics.

First proton-proton collisions took place at the LHC in 2009 at a centre-of-mass energy of 900 GeV followed by collision at 7 TeV in 2010. The LHC successfully delivered data with increasing instantaneous luminosity during the years 2011 and 2012. The centre-of-mass energy was increased to 8 TeV in 2012. Peak luminosities of about 4×10^{33} $\text{cm}^{-2}\text{s}^{-2}$ and 8×10^{33} $\text{cm}^{-2}\text{s}^{-2}$ have been reached in years 2011 and 2012, respectively. The physics program of the LHC is carried out by four major experiments, ATLAS [63], CMS [65], LHCb [66] and ALICE [67]. The ATLAS experiment recorded proton-proton collision data corresponding to an integrated luminosity of 4.57 fb^{-1} during 2011 and additional 20.3 fb^{-1} during 2012. The data recorded during these two years led to one of the major milestones in particle physics, the discovery of a Higgs boson with a mass of about 125 GeV.

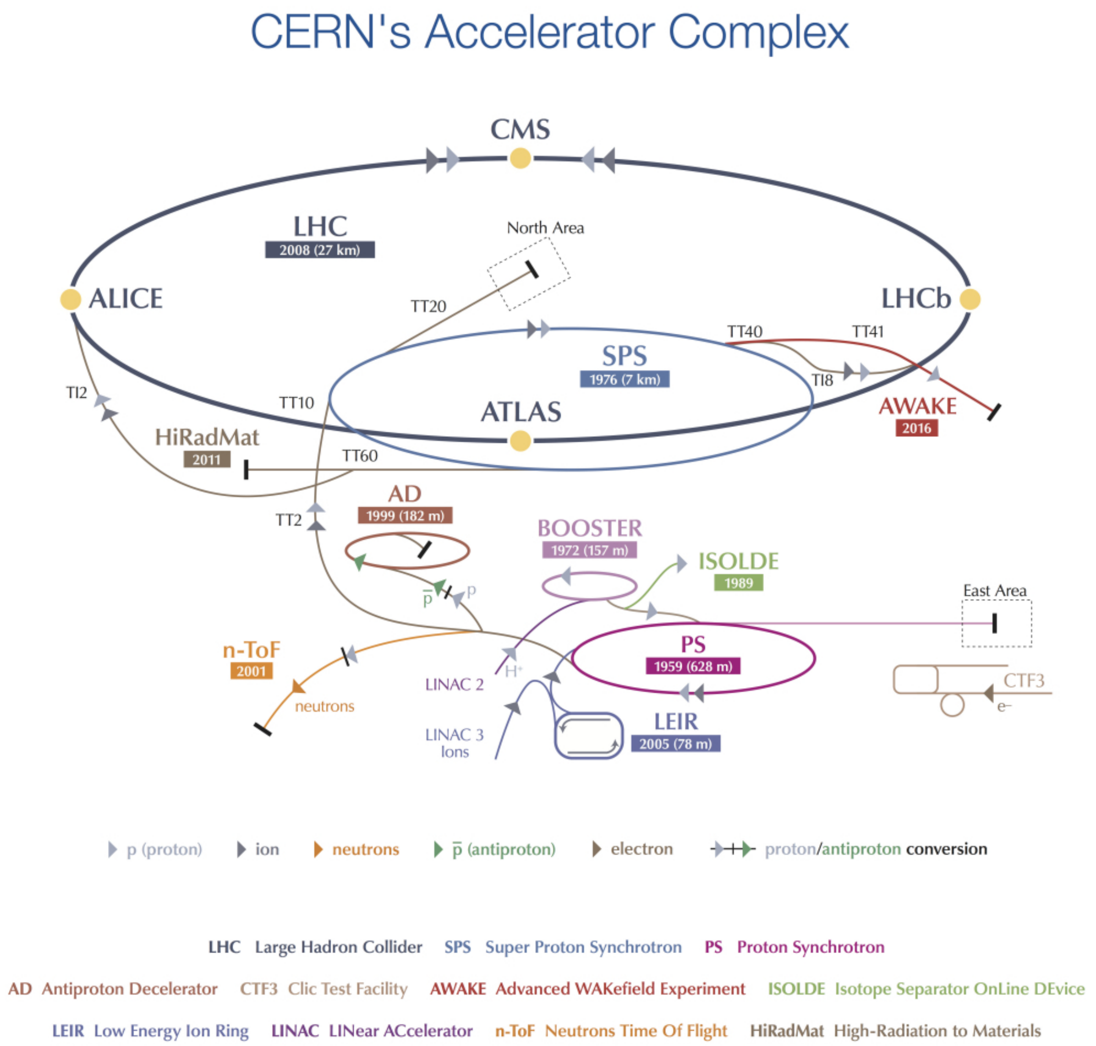

Figure 3.1.: Illustration of the CERN accelerator complex [64]. The acceleration of the protons starts in Linac2 followed by the Booster. The Proton Synchrotron (PS) and the Super Proton Synchrotron (SPS) further accelerate the protons until their final injection into the LHC, where they acquire their final collision energy.

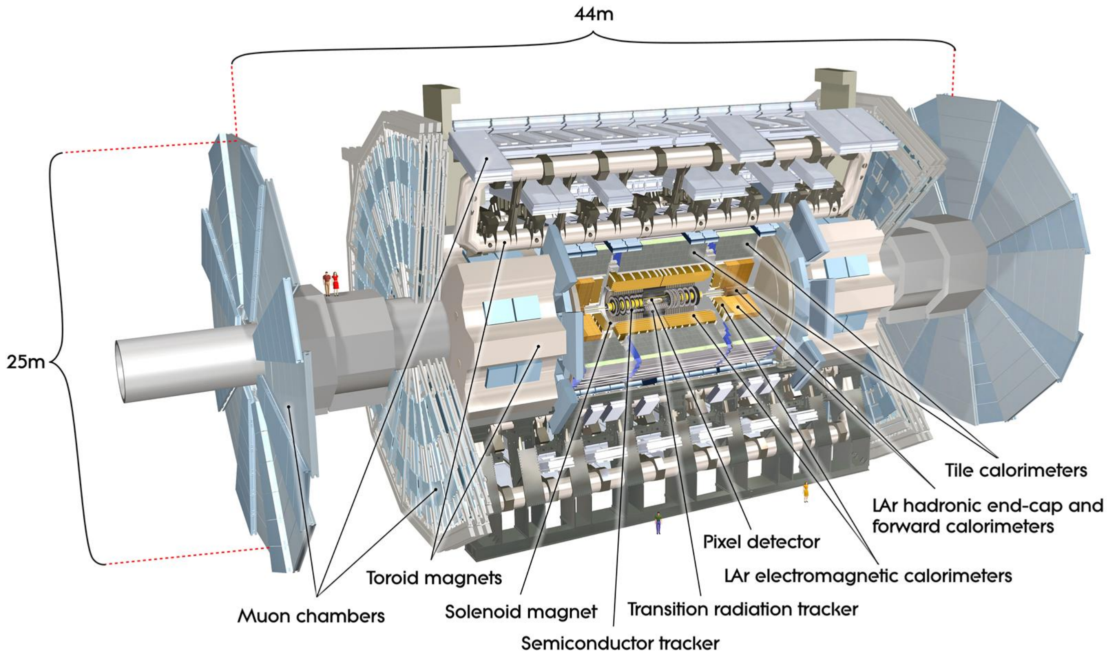

Figure 3.2.: Cut-away view of the ATLAS detector with its sub-detectors [63].

3.2. The ATLAS Detector

The ATLAS detector is a multi-purpose detector aiming to explore a wide range of physics phenomena at the Teraelectronvolt energy scale. The physics goals impose strong requirements on particle reconstruction efficiency and accuracy. A schematic view of the ATLAS detector is shown in Figure 3.2 . With a length of 44 m and a height of 25 m it is the largest detector at the LHC, it is installed at one of the LHC interaction points about 100 below ground. ATLAS consists of four sub-detectors which are installed cylindrically around the beam pipe in the central barrel part and in disks in the endcap parts which are symmetrically in the forward and backward direction with respect to the proton beams. The innermost sub-detector is the inner detector (ID), followed by the electromagnetic calorimeter, the hadronic calorimeter and finally the muon spectrometer (MS) in the outermost layer. Each of these sub-detectors is briefly described below based on reference [63].

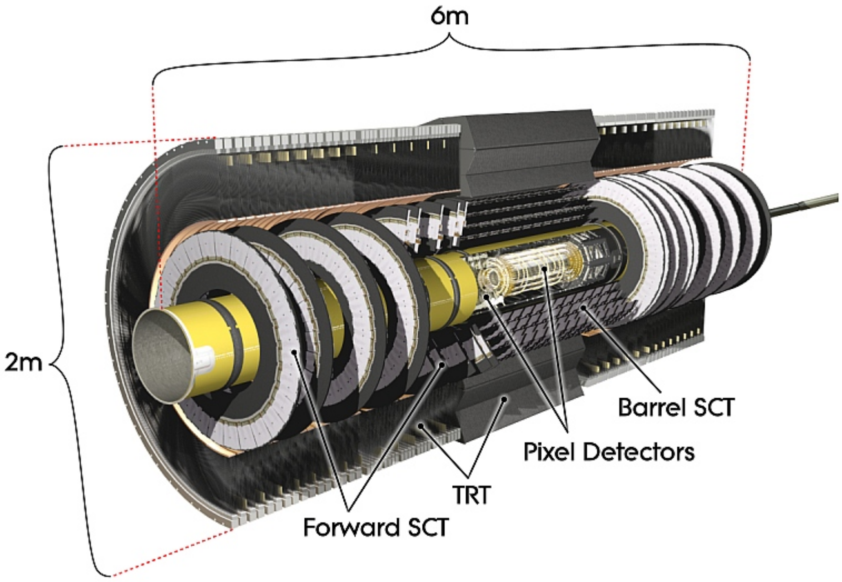

Figure 3.3.: Cut-away view of the ATLAS inner detector [63].

3.2.1. The ATLAS coordinate system

The right-handed ATLAS coordinate system has its origin at the interaction point. The $z-$axis is pointing along the beam direction, the $y-$axis upwards and the $x-$axis towards the centre of the LHC ring. The azimuthal angle ϕ is defined in the transverse plane orthogonal to the beam axis starting from the positive side of the $x-$axis. The polar angle θ is defined with respect to the $z-$axis.

A commonly used kinematical variable at collider experiments is the rapidity

$$y \; = \; 1/2 \cdot \ln \left(\frac{E + p_z}{E - p_z} \right) \;, \tag{3.1}$$

where E and p_z are the particle energy and the momentum component in z-direction, respectively. The difference in rapidity of two particles is independent of Lorentz boosts along the beam axis. In the limit where the particle velocity approaches the speed of light and for massless particles the rapidity can be approximated by the pseudo rapidity

$$\eta \; = \; 1/2 \cdot \ln \left(\frac{\theta}{2} \right) \;. \tag{3.2}$$

The ATLAS detector is divided into the *barrel* region with cylindrical geometry extending up to $|\eta| \lesssim 1.5$ (depending on the particular sub-detector) and the *endcap* regions with a disk structure at larger η values. The angular separation between two particles is commonly measured by $\Delta R = \sqrt{\Delta\eta^2 + \Delta\phi^2}$, where $\Delta\eta$ and $\Delta\phi$ are the difference in pseudo rapidity and azimuthal angle between the particles, respectively.

3.2.2. The Inner Detector

In the inner detector curved trajectories of charged particles are reconstructed in a 2 T solenoidal magnetic field providing measurements of the particle momenta and of the position of the interaction vertices. The layout of the inner detector is illustrated in Figure 3.3. It has a length of 5.3 m, a diameter of 2.5 m and consists of three independent detector modules with high granularity covering the pseudo rapidity region $|\eta| < 2.5$. The innermost inner detector module is the pixel detector which consists of three cylindrical layers of silicon pixel sensors in the barrel and three disks in the endcap regions. The pixel layer closest to the beam pipe is referred to as B-layer, since it provides crucial informations for the identification of b-quarks. The pixel sensors have a spatial resolution of 10 μm in the transverse and 115 μm in the longitudinal direction with respect to the beam.

The Semi-Conductor Tracker (SCT) surrounds the pixel detector in four cylindrical layers of silicon microstrip sensors in the barrel and nine disks in each of the endcap regions. The spatial resolution of the SCT sensors is 17 μm in the transverse and 590 μm in the longitudinal direction.

The outermost inner detector module is the Transition Radiation Tracker (TRT). It is composed of 4 mm diameter Kapton straw tubes with a tungsten wire in their centre. The tubes are filled with a gas mixture of 70% Xe, 27% CO_2 and 3% O_2 which allows for the detection of transition radiation photons. This detector measures the particle position only in the transverse plane.

3.2.3. The Calorimeter System

An illustration of the ATLAS calorimeter system is given in Figure 3.4. It consists of an electromagnetic calorimeter (EM) surrounded by a hadron calorimeter

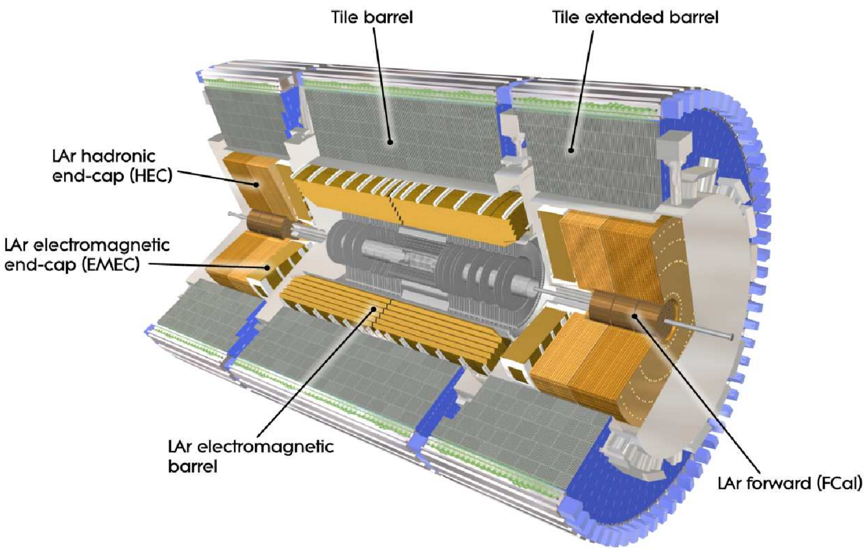

Figure 3.4.: Cut-away view of the ATLAS calorimeter system [63].

which cover the pseudorapidity range $|\eta| < 4.9$. Both calorimeters are sampling calorimeters alternating passive absorber plates to active material where the signals are produced. The total detector material at $\eta = 0$ corresponds to 9.7 hadronic interaction length λ.

The liquid-argon (LAr) EM calorimeter is ideally suited for precision measurement of electron and photon energies. Liquid argon is used as active material while lead is used as absorber. The EM calorimeter extends up to $|\eta| = 3.2$. The total thickness of the EM calorimeter is about 22 radiation lengths in the barrel and greater than 24 in the end-caps. In the barrel part, it is divided in depth into three cylindrical layers which are segmented into $\eta - \phi$ cells of varying size depending on the layer and on pseudorapidity. The ϕ cell sizes rage from 0.025 to 0.1, while the η sizes range from 0.0035 to 0.075 . The energy resolutions for electrons and for photons are ranges from $9 - 22\%/\sqrt{E}$ and from $8 - 14\%/\sqrt{E}$, respectively, depending on pseudorapidity.

The hadron calorimeter has a coarser granularity than the EM calorimeter and serves for the reconstruction of hadron jets and the measurement of the missing transverse energy. It is divided into three sub-detector systems which use different technologies to cope with the η-dependent radiation environment. The tile

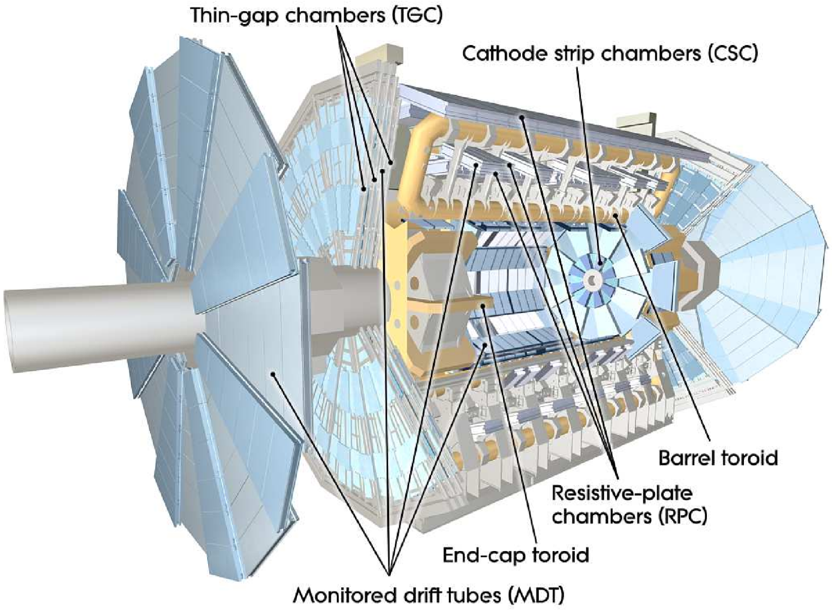

Figure 3.5.: Cut-away view of the ATLAS muon spectrometer system [63].

calorimeter covers the pseudorapidity range $|\eta| < 1.7$. Scintillating tiles are employed as active material and steel as absorber. In the end-cap regions, a LAr hadron calorimeter (HEC) is used which extends up to $|\eta| = 3.2$ and uses Argon as active and copper as absorber material. The forward regions at $3.1 < |\eta| < 4.9$ are instrumented with liquid-Argon Forward CALorimeters (FCAL) which are divided into three modules. In the module closest to the interaction point, copper is used as absorber material, while the other two modules employ tungsten. The jet energy resolution in the barrel is about 15% for jets with $p_T = 50$ GeV and about 7% for jets with $p_T = 1$ TeV [117].

3.2.4. The Muon Spectrometer

The muon spectrometer is instrumented with separate high-precision tracking and muon trigger chambers. The muon momenta are measured by reconstructing the curvature of the muon trajectory in a toroidal magnetic field of 0.3-1.2 T which is produced by large superconducting air-core toroid magnets. The layout of the muon spectrometer is shown in Figure 3.5.

Precision measurement of the track coordinates in the bending plane of the magnetic field is provided by three layers of Monitored Drift Tube (MDT) chambers covering the pseudo rapidity range $|\eta| < 2.7$. Because of the high background rates at large pseudo rapidities, $|\eta| > 2$, Cathode Strip Chambers (CSC) are used close to the beam-pipe in the inner end-cap layers. The CSC are multi-wire proportional chambers with cathodes segmented into strips. The muon spectrometer allows for a muon momentum resolution of better than 10% for momenta up to 1 TeV. The best momentum resolution of 3-4% is achieved for muons with transverse momenta of about 100 GeV.

The muon trigger chambers cover the pseudo rapidity range $|\eta| < 2.4$. Resistive Plate Chambers (RPC) are used in the barrel and Thin Gap Chambers (TGC) in the end-cap regions provide a relatively coarse but fast muon momentum measurement for the Level-1 muon trigger.

3.2.5. The Trigger System

At a nominal LHC bunch crossing rate of 40 MHz, it is impossible to record and store the data of each bunch crossing. A highly selective trigger system is designed to reduce the initial rate to about 300 Hz keeping the interesting events. The triggering is performed in three stages with increasing sophistication: the Level-1 (L1), the Level 2 (L2) triggers and the event filter (EF). Each trigger level refines the decisions made at the previous level.

The L1 trigger is hardware based and designed to reach a decision within a latency of less than 2.5 μs reducing the initial rate to about 75 KHz. It relies on coarse energy measurement in the calorimeters and on muon momenta information provided by the RPC and TGC chambers. It selects high transverse-momentum muons, electrons, photons, jets and τ leptons decaying into hadrons, as well as large missing and total transverse energy. The L1 defines in each triggered event regions of interest (RoI) in η and ϕ which are further investigated by the higher-level triggers.

The L2 trigger selection is seeded by the RoI information provided by the L1 trigger. Unlike the L1 trigger, the L2 trigger uses the full detector granularity within the RoIs allowing for a more precise reconstruction of particle properties. The L2 triggers reduce the event rate to approximately 3.5 kHz.

The final stage of the event selection is the event filter which reduces the event rate to 300 Hz. It uses the offline reconstruction algorithms described in Chapter 4 .

3.2.6. Luminosity Measurement

A precise measurement of the recorded instantaneous and integrated luminosity is essential for all physics studies. Several luminosity measurement techniques are employed as described in [69]. The detectors relevant for the luminosity monitoring are the inner detector, the beam conditions monitor (BCM) [69] and the LUCID detector [70]. The inner detector provides a luminosity measurement from the average number of reconstructed proton-proton interactions per bunch crossing. The LUCID detector surrounds the beam pipe on both sides of the interaction point at a distance of 17 m. It consist of Cherenkov detectors which measure the particle flux from the interaction point in very forward direction. The BCM detector consists of four small diamond sensors arranged around the beam pipe in a cross pattern on each side of the interaction point. It is a fast detector primarily designed to monitor the beam condition which also provides an independent luminosity determination. The overall uncertainty in the luminosity measurement using these methods is about 3%.

4. Reconstruction of Physics Objects

The raw ATLAS data containing signals of all detector read-out channels, need to undergo several reconstruction steps before they can be analyzed. The event reconstruction software is implemented in the ATLAS software framework ATHENA [97]. This chapter describes the procedure for the reconstruction of physics objects relevant for the analysis presented in this thesis. For a detailed overview of the ATLAS detector reconstruction software see [98].

4.1. Reconstruction of Charged Particle Tracks

The reconstruction of charged particles tracks and interaction vertices is based on the measurements in the inner detector which allow for the reconstruction of tracks within the pseudorapidity range of $|\eta| < 2.5$. A track is characterized by its four-momentum vector and two impact parameters: d_0, i.e., the distance of closest approach between the track and the interaction point in the transverse plane and z_0, i.e. the z coordinate of the track calculated at the same point of closest approach.

Tracks are reconstructed by the inner detector track reconstruction software [99]. First raw data from the pixel and SCT detectors are transformed into three-dimensional space points (so called “hits”), while the TRT detector information is translated into drift circles. Subsequently, track seeds are formed from a combination of space-points in the three pixel layers and the first SCT layer. These seeds are then extrapolated through the SCT to form track candidates from all hits on the track path. The track candidates are obtained by a fit trough all hits using a *Kalman filter* algorithm [100]. Ambiguities in the association of the hits to the track are resolved by this fitting procedure and tracks produced by a random association of hits are rejected. The selected tracks are then extrapolated to the TRT and finally refitted using the full information of all three tracking detectors. In order to improve the tracking efficiency for secondary tracks from photon conversion or decays of long-lived particles (like kaons), a complementary algorithm [99] searches for unassociated track segments in the TRT, these segments are then extrapolated towards the SCT and the pixel detector in a similar manner as in the default algorithm. All tracks with $p_T > 100$ MeV are considered for physics analysis.

4.2. Vertex Reconstruction

The vertex reconstruction algorithm and its performance are described in detail in [98, 101] and only briefly summarized here. The vertex finding algorithm selects a set of well reconstructed tracks and generates a vertex seed according to the average value of the tracks z coordinate. The z coordinate of the tracks is computed relative to the expected average position of the collision point. An *adaptive vertex fitting* algorithm [102] determines the vertex position based on the vertex seed and on the tracks around it via a χ^2 fit. Based on this fit, tracks that are incompatible with the found vertex by more than seven standard deviations are used to seed the next vertex. The procedure is performed iteratively until either all tracks are associated to a vertex or no additional vertex can be found. The performance of this procedure depends on the expected position of the average interaction point which is monitored during LHC data taking and is computed in intervals of a few minutes as described in [103].

The vertex with the largest sum of transverse momentum of all associated tracks is identified as the *primary vertex* (PV), corresponding to the interaction point of the hard scattering process in the event. All other vertices in the event are assumed to result from minimum bias interactions and are called *pile-up* vertices. In data recorded during 2012, there were on average 21 multiple interactions occurring per bunch crossing. Such a high vertex multiplicity strongly affects the ambient energy density in the event, such that an accurate pile-up description in simulation is crucial for the modelling of physics processes. In ATLAS, events are simulated assuming various pile-up conditions and weighted such to reproduce the observed average number of interactions per bunch crossing.

4.3. Electron Reconstruction and Identification

Electron are reconstructed and identified by combining EM calorimeter and inner detector measurements. The corresponding dedicated algorithm is described in [104]. The electron candidate is reconstructed as a clusters of EM calorimeter cells which is matched to a track in the inner detector. Special care during the matching is taken to account for Bremsstrahlung losses of the charged particle. The electron energy is computed as a weighted average between the cluster energy and the track momentum. Several corrections are applied to take into account energy losses in the material of the inner detector and effect of electromagnetic shower leakage. The electron direction is defined by the corresponding track parameters.

Further identification criteria are applied to electron candidates to reduce contaminating contribution of photon conversions and hadronic jets. Three different identification criteria are provided based on a multi-variate analysis program (TMVA [105]) and several selection criteria :

- Loose electron identification: variables related to the shape of the electromagnetic shower and to the amount of the hadronic leakage are used in a multi-variate analysis program.
- Medium electron identification: the total shower width and the difference between the largest and second largest energy deposit are considered in a multi-variate analysis program in addition to the loose variables. Furthermore stricter track matching requirements are imposed.
- Tight electron identification: in addition to medium requirements, converted photons are rejected by requiring a hit in the innermost layer of the inner detector. Furthermore, the number of TRT hits associated to the electron is employed as additional variable in the multi-variate analysis program.

The performances of the electron identification are measured with several calibration data samples (using events with leptonic decays of W, Z bosons and J/ψ meson) and compared to simulation [106]. Corresponding corrections of the simulated electron identification efficiency are measured and applied as p_T and η dependent weight to each simulated electron candidate. Additional corrections are applied to the energy scale and energy resolution of simulated electrons to match the one in data according to [107]. Systematic uncertainties on the measure of the identification efficiency ranges from 1-2% depending on the transverse momentum of the electron, while uncertainties on the measure of the energy scale and resolution range approximately from 0.3-3% depending on η. Finally, the electrons used in the presented analysis are rejected if they are detected in a region of the calorimeter with readout problems or suffering from high noise.

Prompt electrons, originating from the decay of a resonance like the Z^0 boson or the Higgs boson are very likely to be *isolated*, i.e. there is little particle activity expected in their surroundings. This is in contrast to electrons originating from hadron decays, which instead will be likely to be surrounded by a jet of particles. Two isolation variables are defined to account for the activity in a cone of size $\Delta R = \sqrt{\Delta\phi^2 + \Delta\eta^2}$ around the electron candidate:

- Track isolation, $p_T^{cone} = \sum_{\Delta R<0.4} p_{T,i}$, is the scalar sum of the transverse momenta $p_{T,i}$ of all tracks i in a cone $\Delta R \leq 0.4$ around the electron direction. The electron track itself is not counted here.
- Calorimeter isolation, $E_T^{cone} = \sum_{\Delta R<0.2} E_{T,i}$, is the scalar sum of transverse energies $E_{T,i}$ of each topological cluster i in a cone $\Delta R \leq 0.2$ around the

electron direction. Clusters associated to the electron itself are not counted. The value of this variable is corrected as a function of the vertex multiplicity in the event in order to account for the pile-up effects and therefore to assure a constant electron selection efficiency for each event.

4.4. Muon Reconstruction

ATLAS employs a variety of strategies for the reconstruction and identification of muons, relying primarily on the tracking in the muon spectrometer and supplemented in most cases with the tracking in the inner detector and the energy deposit in the calorimeter. A detailed description of the muon reconstruction algorithms and their performance is reported in [98]. In the following only the muon reconstruction strategy relevant for this thesis is described.

The STACO *combined* muon algorithm [108] associates tracks found in the muon spectrometer with the corresponding inner detector track and calorimeter energy deposit. At first, track segments are reconstructed in each of the three muon stations and are linked together to form a track. The muon spectrometer track is extrapolated to the inner detector taking into account the energy loss and multiple scattering in the calorimeters. The extrapolated track is matched with an inner detector track via χ^2-matching. Finally, a statistical combination of the inner detector and muon spectrometer tracks is performed to obtain a combined muon track.

Muon identification efficiency, momentum scale and momentum resolution are evaluated in [109] where performance is compared with prediction from simulation. A set of corrections on the muon momentum scale, resolution and identification efficiency is applied to simulation to ensure a good agreement with data. Uncertainties on these corrections are of the order of a fraction of percent.

Isolation variables, are derived and employed in a similar manner as for electrons. The only difference is the use of calorimeter clusters with fixed size (so-called towers) instead of the topological cells in the definition of E_T^{cone}. Pile-up corrections similar to those employed for electrons are used for muons as well.

4.5. Jet Reconstruction and Energy Calibration

Jets are reconstructed by means of the FastJet package [110], which provides a broad range of jet finding algorithms and analysis tools. In the following jet reconstruction methods relevant for the analysis presented in this theses are briefly described, for more detail see [98].

In general, jets may be reconstructed out of any set of four vector objects. In ATLAS, the jet reconstruction relies most commonly on energy deposit measured by the calorimeters. Calorimeter cells are grouped together by a clustering algorithm forming the so called *topological clusters* [111], i.e. three-dimensional clusters representing the energy depositions of the shower particles. The clustering procedure starts with seed calorimeter cells with a signal-to-noise ratio greater than a certain threshold. All nearby cells are combined with the seed cells if they pass a second, lower, signal-to-noise ratio threshold.

Each topological cluster is then used as input to the *anti-k_t* algorithm [112]. The algorithm defines a metric to assess distances between the clusters i and j:

$$d_{ij} = \min(\frac{1}{k_{t,i}^2}, \frac{1}{k_{t,j}^2}) \cdot \frac{\Delta R_{ij}^2}{R^2} \quad \text{and} \tag{4.1}$$

$$d_i = \frac{1}{k_{t,i}^2}\,, \tag{4.2}$$

where $k_{t,i}$ is the p_T of the cluster i and $\Delta R_{ij}^2 = \sqrt{\Delta\phi_{ij}^2 + \Delta\eta_{ij}^2}$ is the angular distance between the two cluster i and j. For the presented analysis the distance parameter R is chosen to be $R = 0.4$. If the distance d_{ij} between two cluster i and j is smaller than d_i, the clusters are grouped together and their four momenta are summed. Otherwise they are kept as a single entity. The clustering procedure is iterated until no further cluster can be merged. The metric is designed such that high-p_T clusters will accumulate the soft activity surrounding them, therefore leading to conical jet shapes.

Given the high pile-up environment of the LHC, it is important to distinguish jets originating from the hard scattering process and those related to pile-up interactions. For this purpose, each jet is characterized by a so-called *jet vertex fraction* (JVF). The value of the JVF is defined as the p_T-weighted fraction of inner detector tracks pointing to the primary vertex among all tracks associated to the corresponding jet:

$$\mathrm{JVF} = \frac{\sum\limits_{PV-tracks} p_{T,i}}{\sum\limits_{tracks} p_{T,i}} \,. \tag{4.3}$$

The jet vertex fraction can only be defined for jets within inner detector coverage of $|\eta| < 2.5$, while the calorimeter jet reconstruction itself is possible up to $|\eta| < 4.5$.

Energy Calibration The ATLAS calorimeters are calibrated using test beam electrons [113]. However, the response of the calorimeters to electromagnetic showers differs from the response to hadronic showers. A dedicated jet energy scale (JES) calibration is therefore performed based on simulation [114]: the jet energy is corrected to correspond, on average, to the simulated energy of the corresponding hadronizing parton. The jet direction is also corrected such to point to the primary vertex instead to the origin of the ATLAS detector coordinate system. A set of corrections is evaluated to take into account for pile-up effects [115, 116]. Simulated jet resolution is also corrected to better describe the data [117]. Finally, several jet energy scale corrections are applied for a better agreement between data and simulation. These corrections are determined with 2011 ATLAS data using several techniques exploiting the transverse momentum balance between a jet and a reference object such as a photon, Z boson or another jet [114, 118]. Systematic uncertainties on the jet energy scale and resolution due to imperfect Monte Carlo modelling are evaluated to range from 1-6% depending on the jet p_T and pseudorapidity.

4.6. Identification of b-Jets

The typical decay length of a b-hadron in the ATLAS detector is of the order of few millimetres. Exploiting the high precision of the inner detector tracker it is possible to discriminate between the jets originating from b-quarks and those from other quarks or gluons (also referred to as light-jets). The identification technique used for this purpose is called *b-tagging* and the identified b-tagged jets are referred to as b-jets.

Several b-tagging algorithms have been developed in ATLAS. The relevant algorithms for this thesis are briefly described in what follows, for a more detailed

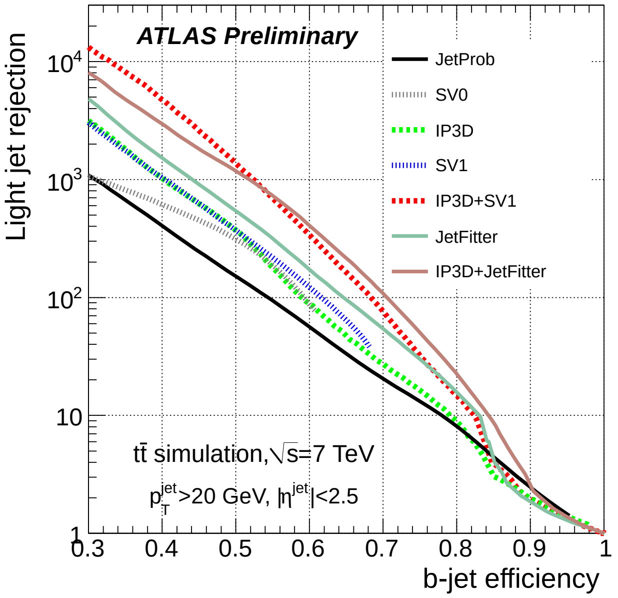

Figure 4.1.: Light-jet rejection as a function of the b-jet tagging efficiency for several different tagging algorithms [121], obtained with simulated $t\bar{t}$ events. The rejection is defined as the inverse of mistagging rate of light jets.

description see [98]. The b-tagging algorithm starts by associating tracks to the jets based on their angular distance ΔR to the jet. the mentioned tracks should satisfy strict selection criteria aimed to ensure a good track quality and to reject tracks likely to come from strange hadron decays or photon conversions. The discrimination between the b-jet and other jets is based on simulated distributions of several discriminating variables. Given the relatively high mass of b-hadrons, the tracks associated to a b-jet will have a relatively wide spread of impact parameter values. This feature is used by the IP3D b-jet tagging algorithm, where a corresponding discriminating variable is defined based on impact parameter significance[1] of all tracks associated to the jet. An alternative approach, used by the $SV1$ algorithm, is instead to search for inclusive secondary vertex formed by the decay products of the b-hadron. The search includes also the subsequent charm hadron decays. Another algorithm, called JetFitter [120], relies instead on the direction of the jet to fully reconstruct the decay chain of a b-hadron, under the

---

[1] The significance is defined as the value of the impact parameter divided by the error on its measurement.

assumption that the decayed particles will be emitted along the jet axis. The outputs of each of these three algorithms gives a measure of the probability that the reconstructed jet originates from a b-quark. Finally, the outputs of the three described algorithms are combined based on an artificial neural network multivariate program [105] to maximise the discriminating power. The output of this neural network is referred to as $MV1$ tagger and is used for the Higgs boson search presented in this thesis.

The performance of the mentioned algorithms is evaluated in data selecting $t\bar{t}$ events and compared to simulation [121]. Figure 4.1 shows the b-tagging efficiency as a function of the inverse of the light-jet mistagging rate for different b-tagging algorithm on $t\bar{t}$ simulated events. The tagging efficiency $\epsilon_b^{t\bar{t}}$ obtained from $t\bar{t}$ events is used to define several b-tagging working points. Corrections due to non perfect modelling of the b-tagging performance are evaluated by means of several methods in [122, 123] and used to determine event weights for simulated events. The uncertainties on these corrections range from 5-10% depending on the p_T and pseudorapidity of the jet.

4.7. Tau-Jet Reconstruction

The reconstruction of jets originating from hadronically decaying τ leptons (in the following τ-jets) is described in detail in [98]. A τ-jet candidate is seeded by reconstructed calorimeter jets with $p_T > 10$ GeV and $|\eta| < 2.5$. Tracks are then associated to the jet and a combination of the tracking and calorimeter information is performed. τ-jets can be distinguished from other jets by their low track multiplicity and a narrower clustering of energy deposit in the electromagnetic and hadronic calorimeters. The τ-jet identification in ATLAS is based on a Boosted Decision Trees (BDT) multivariate procedure [126]. One BDT discriminant has been developed to discriminate τ-jets from quark and gluon initiated jets and a separate one was developed to reject electrons.

4.8. Missing Transverse Energy

The missing transverse energy, E_T^{miss}, is the the vectorial sum of the transverse momenta of all the physics objects and calorimeter cells in the event changed of sign. Undetected particles, such as neutrinos, lead to an unbalance of the total transverse momentum, thus, to a non zero value of E_T^{miss}.

Reconstruction and calibration of E_T^{miss} with the ATLAS detector is described in detail in [124]. The missing transverse energy measurement relies on the reconstruction of all physics objects in the event, it includes: muons and their energy deposits in the calorimeter, electrons, jets (weighted by their corresponding JVF), inner detector tracks (to take into account low-p_T particles which are not well reconstructed in the calorimeters), photons and τ leptons. The calorimeters cells are calibrated depending on the pjysics object with which they are associated. The transverse energy of cells not associated to any object is taken into account in the so called “CellOut” contribution. This contribution, together with the one related to jets with $10 < p_T < 20$ GeV are referred to as the *soft term* of the missing transverse energy. The soft term is found to be very sensitive to pile-up. In order to reduce the impact of pile-up, the soft term is scaled by the corresponding soft-term-vertex-fraction (STVF), which is calculated in the same way as JVF for jets.

A detailed description of the performance of the E_T^{miss} reconstruction and calibration may be found in [125].

4.9. Overlap Removal

Reconstruction of physics objects defined in the previous section may sometimes be ambiguous. For example, a τ-jet is always reconstructed also as a common jet. To avoid double counting of the physics objects originating from the same particle, an overlap removal procedure is performed. A match between physics object of different sort is seeded in a cone of $\Delta R < 0.2$. If the matching occurs, the object with the lowest ranking is removed from the event. Physics object are ranked according to the following order, starting with the highest rank: muon, electron, τ-jet and finally common jets.

4.10. Trigger

The ATLAS trigger system [127] consists of three stages. The Level-1 (L1) trigger is an hardware trigger which reduces the event rate to approximatively 100 kHz and selects the Regions of Interest (RoI) to be further investigated by the High Level Trigger (HLT). The HLT comprises the Level-2 (L2) trigger employing fast reconstruction algorithms and the Event Filter (EF) exploiting the full ATLAS event reconstruction.

In the presented search two triggers are employed: an electron EF trigger, which selects events containing an electron with $p_T > 24$ GeV and a combined muon-electron EF trigger, which requires the presence of a muon with $p_T > 8$ GeV and an electron with $p_T > 12$ GeV in the event. Detailed description of the muon and electron triggers can be found in [128, 129]. Trigger efficiency for both triggers is evaluated in data selecting Z candidate events and compared with prediction from simulation. Corrections are derived as function of the lepton pseudorapidity and transverse momentum to match the simulated trigger efficiency with the one in data [128, 129].

4.11. Truth Particles

For simulated events, the ATLAS reconstruction software provides information about the generated particles (called *truth particles*). The irrticle type, the kinematic properties, decays and interactions are recorded following the conventions in [130]. A particle is defined as stable if $c\tau > 1$ m, where τ is its mean life time. Particles emerging from interactions in the detector are excluded from this definition. Each particle in the event has a unique identifier (so-called “bar-code”). Jets reconstructed from stable particles are called *truth jets.*

5. Search for neutral MSSM Higgs Bosons in $A/h/H \to \tau^+\tau^- \to e\mu + 4\nu$ decays

In the light of the recent discovery of a Higgs boson with mass of about 125 GeV at the LHC [1, 2], it remains an open question whether this new particle is the only missing piece of the electroweak symmetry breaking sector of the Standard Model or whether it is one of several Higgs bosons predicted in theories that go beyond the SM. The most recent measurements [3–6] of properties of the new boson show that they are fully compatible with the ones of the SM Higgs boson. Nevertheless, such a new particle can still be accommodated within theories beyond the standard model (BSM). Among them, supersymmetric extensions of the Standard Model are theoretically favoured, in particular the minimal supersymmetric extension (MSSM) which predicts five Higgs bosons, three of them electrically neutral.

In this chapter the search with the ATLAS detector for the neutral MSSM Higgs bosons decaying into pairs of tau leptons in the fully leptonic final state is discussed. The result have been published in ref. [61] as a part of the ATLAS search for the neutral MSSM Higgs bosons in all final states of the tau lepton decays. The search is based on 20.3 fb^{-1} of data at a centre-of-mass energy of $\sqrt{s} = 8$ TeV recorded by the ATLAS experiment during 2012. This chapter is organised as follows: a brief summary of the MSSM Higgs sector and an introduction to the analysis strategy are given in Section 5.1, while the event selection and categorisation are described in Section 5.2. Section 5.3 describes the estimation of the backgrounds and in Section 5.4 methods for the evaluation of the systematic uncertainties are discussed. Finally, in Section 5.5 the result of the search are presented together with an overview of the statistical methods employed.

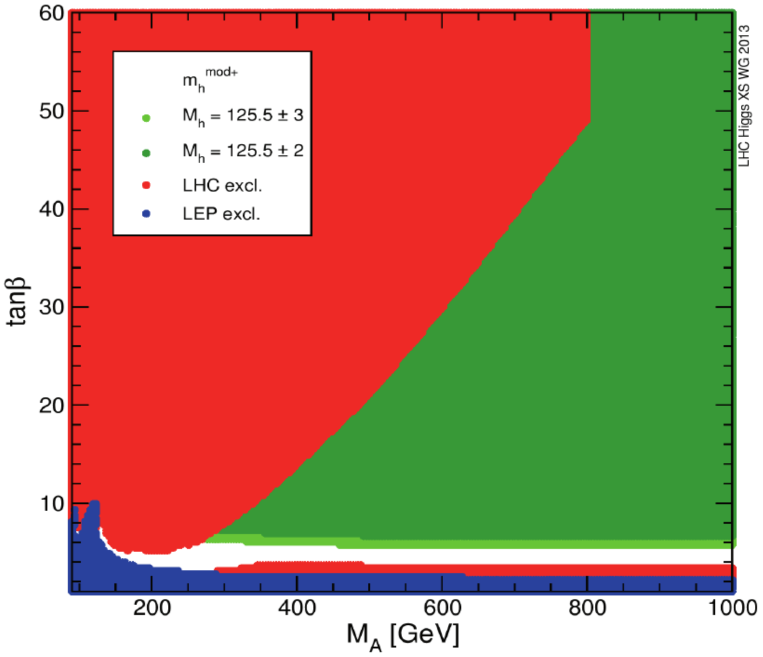

Figure 5.1.: Excluded and allowed regions of the MSSM $m_A - \tan\beta$ parameter space in the m_h^{mod+} benchmark scenario [10], based on direct Higgs boson searches at LEP (blue) and LHC (red). The two green regions are compatible with the assumption that the lightest MSSM Higgs boson, h, has a mass of 125.5 GeV with an uncertainty of 2 GeV (dark green) or 3 GeV (light green).

5.1. Introduction

5.1.1. The Higgs Sector in the MSSM

In the minimal supersymmetric extension of the Standard Model (MSSM) [41,42], the Higgs sector is composed of two electroweak Higgs doublets of opposite hypercharge resulting in five observable Higgs bosons, where two of them are neutral and CP-even (h,H), one is neutral and CP-odd (A) and two are charged ($H^{\pm}$). At tree level, their properties such as masses, widths and branching ratios are predicted depending on only two parameters, often chosen to be the mass of the CP-odd Higgs boson m_A and the ratio of the vacuum expectation values of the two Higgs doublets $\tan\beta$ (for more details see chapter 2). The MSSM predicts the existence of a Higgs boson with properties that resemble those of the SM Higgs boson in large regions of its parameter space. This is usually the case for the lightest Higgs boson, h, while the other two, H and A, tend to be degenerate in mass and decouple from gauge bosons. On the other hand, the couplings of the latter two Higgs bosons to down (up) type fermions are enhanced (suppressed) depending on the value of $\tan\beta$, such that for large $\tan\beta$ bottom-quarks and τ leptons play an important role for Higgs bosons production and decay.

The two dominant neutral MSSM Higgs boson production mechanisms at the LHC are gluon fusion, $gg \to A/H/h$, and the production in association with b-quarks, $pp \to b(b)A/h/H$, the latter becoming increasingly important for large values of $\tan\beta$. These are the only production mechanisms considered in this analysis. Assuming there are no decays into supersymmetric particles (since they are too heavy) and assuming that the lightest neutral CP-even Higgs boson h is identified with the observed Higgs boson of mass ~ 125 GeV, the dominant decay mode for the neutral MSSM CP-odd A and CP-even H Higgs bosons is the decay into a b and anti-b quark pair, followed by the decay into τ leptons pairs. Since it is very difficult to distinguish the former decay from the large $b\bar{b}$ background, the decay mode $A/h/H \to \tau^+\tau^-$ provides the highest sensitivity in the search for neutral MSSM Higgs bosons.

Searches for neutral MSSM Higgs bosons have been performed at LEP [71], the Tevatron [72] and the LHC [73, 74]. In the following, the search for the neutral MSSM Higgs bosons in the final state $A/h/H \to \tau^+\tau^- \to e\mu{+}4\nu$ is presented. This search is complementary to the searches in other $\tau^+\tau^-$ final states characterised by the presence of one or two hadronically decaying τ leptons. For low m_A values the $\tau^+\tau^- \to e\mu + 4\nu$ search channel provides a sensitivity to the signal comparable to the other final states, in spite of the fact that the $\tau\tau$ branching ratio to $e\mu + 4\nu$ is only 6%. This is mainly due to the high transverse momentum threshold at the trigger level for hadronically decaying τ leptons, which is necessary to keep the jet contamination rate at an acceptable level.

As it is virtually impossible to explore the full parameter space of the MSSM, which has a large number of free parameters, several benchmark scenarios have been introduced fixing all parameters except m_A and $\tan\beta$ to typical values for the most interesting physics cases. With the recent Higgs boson discovery, benchmark scenarios of the MSSM have been updated to accommodate the new experimental constraints. As an example, Figure 5.1 shows the currently excluded and allowed regions of the MSSM $m_A$$-$$\tan\beta$ parameter space for the updated m_h^{mod+} benchmark

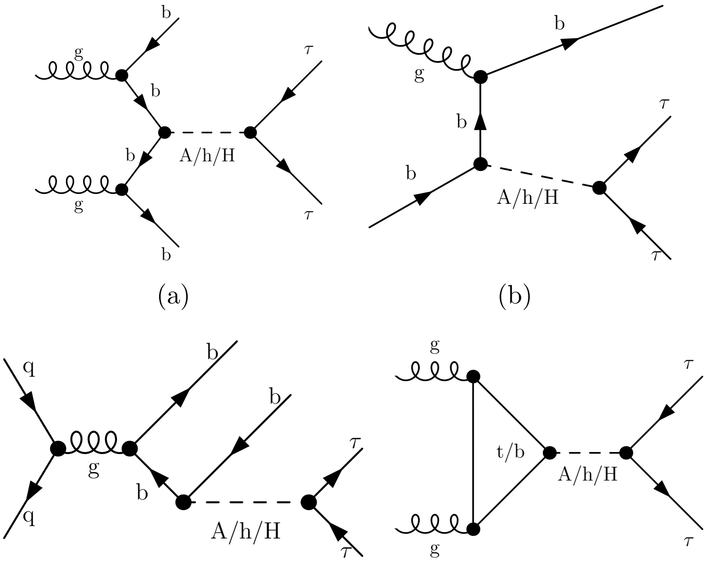

(a) (b)

(c) (d)

Figure 5.2.: Feynman diagrams for the production of the neutral MSSM Higgs bosons in association with b-quarks (a,b,c) and via gluon fusion (d) with subsequent decay into tau lepton pairs.

scenario (see Section 2.3.2). In this scenario, a large region of the $m_A - \tan\beta$ parameter space is compatible with the assumption that the observed Higgs boson is in fact the neutral CP-even Higgs boson h. A relatively large part of this parameter space is still experimentally unexplored, which is a strong motivation to pursue the search for additional neutral MSSM Higgs bosons.

5.1.2. Signal and Background Processes

Signal events in which the neutral MSSM Higgs bosons decay through $A/h/H \to \tau^+\tau^- \to e\mu + 4\nu$ are characterised by the presence of one electron and one muon of opposite charge. These two leptons are isolated and have relatively high transverse momenta. In addition, four neutrinos generate high missing transverse energy in the event. Figure 5.2 shows leading order Feynman diagrams for the two signal production modes considered, gluon fusion and associated production with b-quarks. The presence (absence) of a b-jet in the final state serves as main characteristic for the categorisation in the latter (former) events as described below.

Table 5.1.: The cross sections times by the relevant branching ratios (BR) for signal and the considered background processes, with $\ell = (e, \mu, \tau)$. Signal cross sections are calculated for the m_h^{mod} scenario assuming $m_A = 150$ GeV and $\tan\beta = 20$. The masses of the other two neutral MSSM Higgs bosons are in this case $m_H = 151$ GeV and $m_h = 125$ GeV.

Process	Cross-section × BR (pb)
Signal ($m_A = 150$ GeV, $\tan\beta = 20$, m_h^{mod} scenario)	
$gg \to A/h/H \to \tau\tau \to e\mu + 4\nu$	0.24/0.20/0.95
$pp \to b\bar{b}A/h/H \to \tau\tau \to e\mu + 4\nu$	0.53/0.05/0.49
Backgrounds	
$W \to \ell\nu$+jets	12.22×10^3
$Z/\gamma^* \to \ell\ell$+jets	5.5×10^3
$t\bar{t} \to \ell\ell + X$	137.3
Single top quark ($t-$, $s-$ and $Wt-$channels) $\to \ell + X$	28.4, 1.8, 22.4
Dibosons (WW, WZ and ZZ) $\to \ell\ell + X$	20.6, 6.8, 1.55

The described signal topology is common to several other SM background processes which in general have higher cross sections than the sought signal. The dominant background processes are $Z/\gamma^* \to \tau^+\tau^-$ production either via the Drell-Yan process or in association with jets and top quark production ($t\bar{t}$ and single top quark production). Additional significant background contributions arise from dibosons production (WW, WZ, ZZ) and QCD multi-jet events with non-prompt leptons from hadron decays. Vector boson production ($W \to \ell\nu$ or $Z \to \ell\ell$, where $\ell \equiv e, \mu$) in association with jets is also considered, but has small impact on the total background contamination. Examples of leading order Feynman diagrams for the dominant background processes are shown in Figure 5.3. The production cross sections times the branching fractions for signal and background processes are summarised in Table 5.1.

5.1.3. Analysis Strategy

In this thesis, a search for the neutral MSSM Higgs boson decays $A/h/H \to \tau^+\tau^- \to e\mu + 4\nu$ is presented. The $ee + 4\nu$ and $\mu\mu + 4\nu$ final states are not considered since large background contributions are expected from $Z \to ee$ and

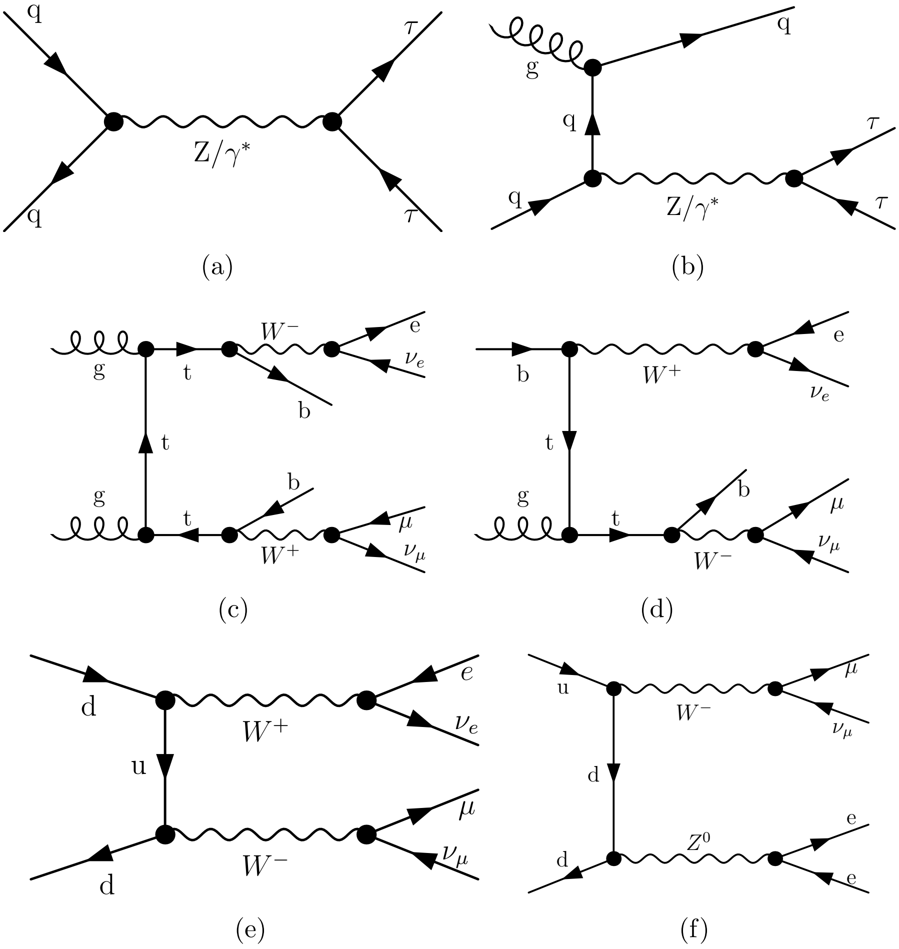

Figure 5.3.: Examples of tree level Feynman diagrams for the most important background processes. The production of $Z/\gamma^* \to \tau^+\tau^-$, either via the Drell-Yan process or in association with jets, is shown in (a) and (b) respectively, top quark pair and single top quark production in (c) and (d), while WW and WZ production in (e) and (f).

$Z/\gamma^* \to \mu\mu$ decays, respectively, such that the sensitivity of the search in these final state is significantly reduced.

Candidate events are selected based on the topological properties of Higgs boson production and decay. The presence of exactly one electron and one muon is required in each event. The electron and the muon are required to be isolated and of opposite electrical charge. The events are categorised into two orthogonal categories. In the so called *b-vetoed* event category, the absence of b-tagged jets is required, thus searching mainly for the signal production via gluon fusion. The main background process in this category is $Z/\gamma^* \to \tau\tau$. In contrast, the presence of exactly one b-tagged jet is required in the so called *b-tagged* event category, in which predominantly the signal production in association with b-quark is searched for. The requirement of a b-jet in the final state suppresses the $Z/\gamma^* \to \tau\tau$ background, consequently, $t\bar{t}$ and single top quark production are the main background processes in this event category. Further selection criteria are introduced in both event categories optimised to enhance the signal with respect to the background.

The search is performed within the MSSM m_h^{mod} benchmark scenario scanning the $m_A - \tan\beta$ plane in the range $90 \leq m_A \leq 300$ GeV and $5 < \tan\beta < 60$. The signal event yields and kinematical distributions are predicted by simulation. The contribution of the dominant $Z/\gamma^* \to \tau\tau$ background process is measured in a dedicated signal-depleted control data sample in order to reduce the systematic uncertainties of the simulation. Similarly, the QCD multi-jet background contribution is also estimated from a dedicated data control sample since this background process is hard to model. The contributions of all other background processes are estimated by simulation. The modelling of the background processes is validated using different signal-depleted validation data samples where good agreement is found.

Systematic uncertainties on cross section calculations and the modelling of the detector response for simulated signal and background processes are taken into account. For background processes determined from data, the uncertainties of the measurement methods are evaluated.

The statistical interpretation of the data is based on the comparison of the observed $\tau\tau$ invariant mass distributions with the predictions of the background-only and signal-plus-background hypotheses. Exclusion limits on the signal production are set by means of a binned profiled likelihood ratio test statistic within the MSSM m_h^{mod} scenario as constraints in the $m_A - \tan\beta$ plane. Furthermore, the data are interpreted in a less model-dependent way in terms of upper limits on the cross section for the production of a generic Higgs boson ϕ with mass m_ϕ via the processes $pp \to b\bar{b}\phi$ and $gg \to \phi$.

5.1.4. Data and Simulated Event Samples

Data Sample

The presented results are based on proton-proton collision data recorded by the ATLAS experiment during 2012 at a centre-of-mass energy of $\sqrt{s} = 8$ TeV corresponding to an integrated luminosity of 20.3 fb^{-1}. The events used in this analysis are recorded using a combination of a single electron trigger and combined electron-muon triggers. Only events recorded with all relevant components of the ATLAS detector fully operational are considered. Additional data quality requirements are applied according to [119] rejecting events with jet activity in known noisy calorimeter regions.

Signal Samples

Signal production via the gluon fusion process $gg \to A/H/h$ was simulated with POWHEG [82] and the associated $b\bar{b}A/H/h$ production with SHERPA [83]. The pseudo-scalar Higgs boson samples were generated in the mass range from 90 GeV to 300 GeV assuming $\tan\beta = 20$. Re-weighting of the production cross sections is applied to simulate other $\tan\beta$ values. All three neutral Higgs bosons A, h, H are assumed to decay with the same kinematical properties. The m_h^{mod} MSSM benchmark scenario is assumed for the prediction of the mass and cross sections of the three neutral Higgs bosons for given m_A and $\tan\beta$ values.

Background Samples

The production of W and Z/γ^* bosons in association with jets was simulated with the ALPGEN [75] generator. The $t\bar{t}$ process was generated using the POWHEG program. Single top quark production via the s-channel and via the Wt process was generated using MC@NLO [77], while single top quark production via t-channel was generated with the AcerMC [78]. Diboson processes (WW, WZ, ZZ) were generated with HERWIG [79]. For all ALPGEN and MC@NLO event samples described above, the parton shower and hadronization were simulated with the HERWIG and the underlying event activity with the JIMMY [80] programme. Different sets of parton density functions (PDFs) are used depending on the generator: CTEQ6L1 [84] is used with the ALPGEN and AcerMC while CT10 [85] is used with SHERPA, POWHEG and MC@NLO.

TAUOLA [87] and PHOTOS [88] are used to model the tau lepton decay and additional photon radiation from final state charged leptons in the leading-log approximation, respectively.

The ATLAS detector response is simulated for all generated samples using the GEANT4 [89, 90] package. The reconstruction of physics objects, described in chapter 4, is performed with the same software as used for the data. The effects of simultaneous recording of additional proton collisions from the same or neighbouring bunch crossings (pile-up) are taken into account in the detector simulation.

5.2. Event Selection and Categorisation

5.2.1. The Common Selection Criteria

According to the kinematical properties of signal events, each event in data and simulation have to satisfy the selection criteria described in the following. Since these are shared by both the b-tagged and the b-vetoed event category, they are referred to as common selection criteria:

(i) The trigger selection requires the presence of a single electron with $p_T >$ 24 GeV or, alternatively, an electron with $p_T >$ 12 GeV togheter with a muon with $p_T >$ 8 GeV.

(ii) At least one reconstructed vertex with more that three associated tracks in order to reject background from cosmic muons.

(iii) Exactly one reconstructed “Tight” electron with $|\eta| < 1.37$ or $1.52 < |\eta| < 2.47$ and $p_T >$ 15 or 25 GeV, depending on the trigger that selected the event.

(iv) Exactly one “Combined” muon with $|\eta| < 2.5$ and $p_T >$ 10 GeV.

(v) The electron have to be isolated with $E_T^{cone}/p_T < 0.08$ and $P_T^{cone}/p_T < 0.06$.

(vi) The muon have to be isolated with $E_T^{cone}/p_T < 0.04$ and $P_T^{cone}/p_T < 0.06$.

(vii) Muon and electron have to be of opposite charge.

(viii) Removal of overlap between reconstructed electron, muon, τ-jets and jets is performed.

(ix) The event is rejected if at least one hadronic τ lepton decay is found with τ-jet transverse momentum $p_T > 15$ GeV. τ-jets candidate are required to be associated to one or three charged tracks, for the identification a "Medium" BDT working point is chosen, additionally, a BDT-based electron veto is applied.

(x) To reduce QCD multi-jet background contamination, the invariant mass of electron and muon has to be greater than 30 GeV.

Details on the definition of physics objects and the applied quality criteria can be found in chapter 4.

Events accepted by the common selection criteria are divided into *b-tagged* and *b-vetoed* categories by requiring the presence or the absence, respectively, of exactly one b-tagged jet in the event. A jet is tagged as a b-jet if it has $p_T > 20$ GeV, $|\eta| < 2.5$, JVF > 0.5 and if it passes the $MV1$ b-tagging criteria corresponding to 70% of b-quark efficiency $\epsilon_b^{t\bar{t}}$ in $t\bar{t}$ events. Further selection criteria are applied to each category and optimized separately as described in the following.

5.2.2. b-Vetoed Event Category

A veto on the presence of b-tagged jets in the final state allows for the selection of signal events produced predominantly via gluon fusion. In this event category, the $Z/\gamma^* \to \tau\tau$ process is an irreducible background due to the same topology of the Higgs and Z boson decay. Other background processes can be discriminated from the signal due to their kinematical properties. The τ leptons from the Higgs boson decay are highly boosted and so are their decay products, resulting in significantly different lepton kinematics in the Higgs decays with respect to diboson or $t\bar{t}$ background processes. Firstly, the electron and muon from Higgs boson decay are predominantly emitted back-to-back as illustrated in Figure 5.4(a) which

Table 5.2.: Summary of the event selection criteria in the b-tagged and b-vetoed event categories applied after the common event selection has been performed.

Category	Selection
b-vetoed	No b-tagged jets $\Delta\phi_{e,\mu} > 1.6$ $\sum \cos \Delta\phi_{E_T,\ell} > -0.4$
b-tagged	Exactly one b-tagged jet $\Delta\phi e, \mu > 2$ $\sum \cos \Delta\phi_{E_T,\ell} > -0.2$ $H_T < 100$ GeV $P_{T\mu} + P_{Te} + E_T^{miss} < 100$ GeV

shows the angular distance $\Delta\phi_{e,\mu} = |\phi_e - \phi_\mu|$ between the two leptons in the transverse plane for the signal and background processes. Secondly, the neutrinos from Higgs boson decay are predominantly collinear with the charged leptons. Thus, the angular correlation between the direction of the missing transverse energy and the two charged leptons in the transverse plane,

$$\hat{E}_T^{miss} \cdot (\hat{P}_T^{\mu} + \hat{P}_T^{e}) = cos(\Delta\phi_{E_T,\mu}) + cos(\Delta\phi_{E_T,e}) = \sum_{\ell} cos(\Delta\phi_{E_T,\ell}) \,,$$

tends to zero as shown in Figure 5.4(b). These two features are used to discriminate between signal and the W boson, top quark and dibosons background processes. No further selection criteria are applied in the b-vetoed category, since no significant improvement in signal sensitivity could be achieved. The described selection criteria are listed in Table 5.2, while in Table 5.3 the predicted numbers of signal and background events after each selection stage are shown.

5.2.3. b-Tagged Event Category

The requirement of exactly one b-tagged jet in the b-tagged event category predominantly selects signal events where the Higgs bosons are produced in association with b-quarks. Background processes with b-jets, as the $t\bar{t}$ and single top quark production, are enhanced compared to the $Z/\gamma^* \to \tau\tau$ background. Also in

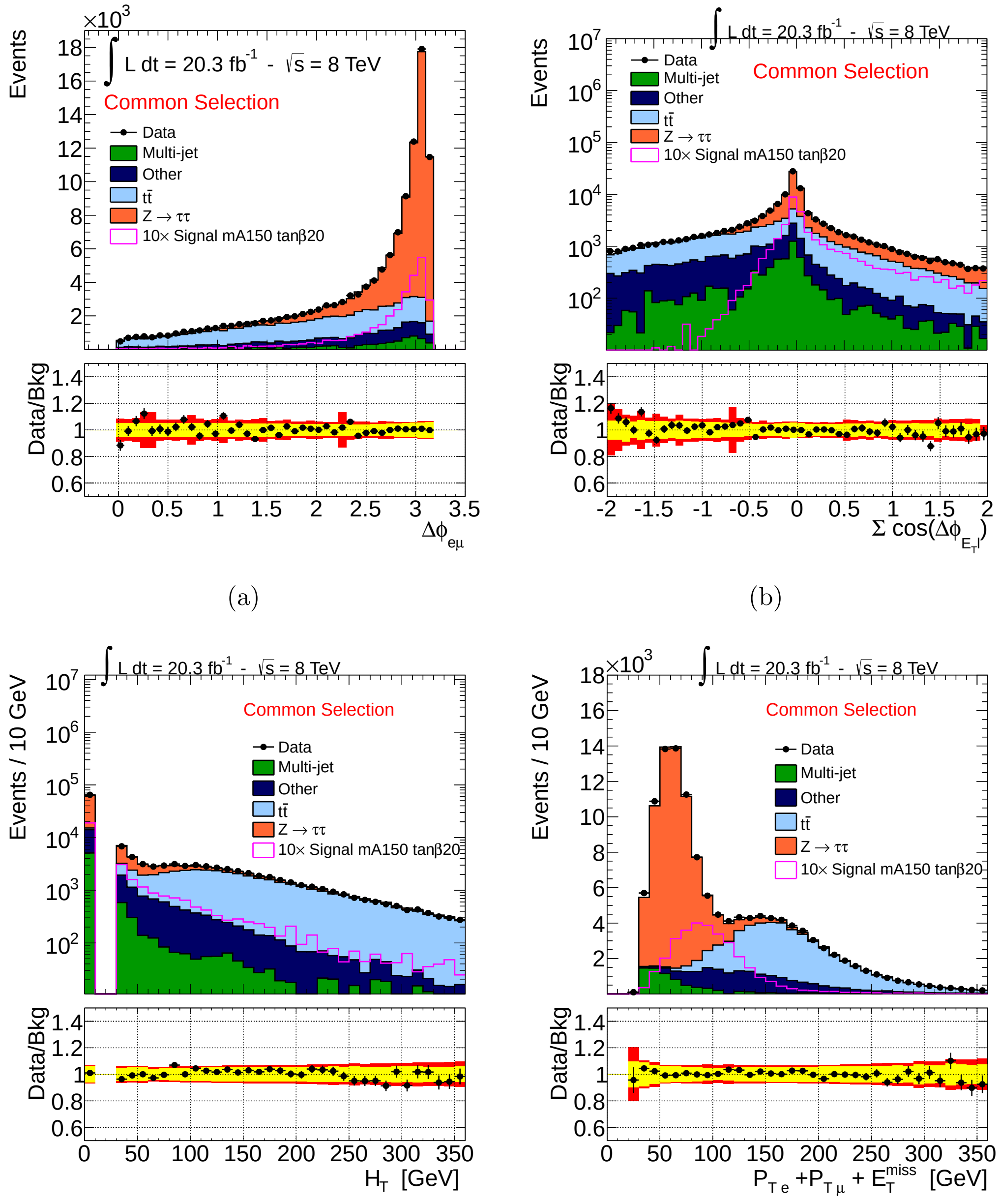

(a) (b)

(c) (d)

Figure 5.4.: Distributions of discriminating variables (see text) after the common selection has been applied. The notation “Other” stands for $W \to \ell\nu$, $Z \to \ell\ell$, diboson and single top quark processes. The prediction for the background contributions is determined as described in Section 5.3. For the signal the m_h^{mod} scenario is assumed with $m_A = 150$ GeV and $\tan\beta = 20$ and it is scaled by a factor ten. The yellow and red band indicates the systematic and statistical uncertainty on the background prediction, respectively.

Table 5.3.: Number of observed and predicted signal and background events, after each selection stage in the b-vetoed event category.

	Common Selections	n(b-jet)=0	$\Delta\phi(e-\mu) > 1.6$	$\sum \cos\Delta\phi > -0.4$
Multi-jet	6693 ± 456	6357 ± 461	5322 ± 438	4180 ± 230
$Z \to \ell\ell$	569 ± 48	564 ± 48	516 ± 47	432 ± 44
$W \to \ell\nu$	1625 ± 155	1604 ± 155	1145 ± 125	660 ± 100
Dibosons	9338 ± 48	9235 ± 48	7358 ± 43	2921 ± 27
$t\bar{t}$	40632 ± 106	7707 ± 46	5044 ± 37	2228 ± 25
Single Top	4449 ± 44	1664 ± 27	1124 ± 22	443 ± 14
$Z/\gamma^* \to \tau\tau$	61503 ± 68	60440 ± 67	58078 ± 65	54680 ± 60
Total	124800 ± 500	87600 ± 400	78600 ± 400	65540 ± 260
Data	125886	89155	79729	65917

Table 5.4.: Numbers of observed and predicted signal and background events after each selection stage in the b-tagged event category.

	n(b-jet)=1	$\Delta\phi$	$\sum \cos\Delta\phi$	$P_{T\mu} + P_{Te} + E_T^{miss}$	H_T
Multi-jet 330 ± 40	208 ± 27	135 ± 22	114 ± 17	101 ± 15	
$Z \to \ell\ell$	5.2 ± 1.8	2.3 ± 1.1	2.3 ± 1.1	1.7 ± 1.0	1.3 ± 1.1
$W \to \ell\nu$	20 ± 6	15 ± 6	13 ± 6	10 ± 6	10 ± 6
Dibosons	99 ± 5	63 ± 4	36.4 ± 3.0	14.8 ± 1.8	14.4 ± 1.9
$t\bar{t}$	19810 ± 70	9680 ± 50	6450 ± 50	808 ± 15	330 ± 10
Single Top	2456 ± 33	1223 ± 23	784 ± 18	122 ± 7	90 ± 7
$Z/\gamma^* \to \tau\tau$	952 ± 9	625 ± 7	540 ± 7	482 ± 6	418 ± 6
Total	23570 ± 90	11750 ± 60	7960 ± 60	1552 ± 25	963 ± 21
Data	23352	11490	7568	1528	904

this category requirements on $\Delta\phi_{e,\mu}$ and $\sum \cos\Delta\phi$ are imposed to reduce the top quark and diboson background contributions as described for the b-vetoed event category. Further selection criteria specific for the b-tagged category are employed as described below.

Signal events in this event category can be discriminated from top quark given their relatively low jet activity. The $t\bar{t}$ events are likely to have two or more highly enegetic reconstructed jets, unlike the signal b-jets which have relatively low energy. Low jet activity is ensured by requesting the sum of the jet transverse momenta H_T to be small. The H_T distribution is shown in Figure 5.4(c). The jets used for the calculation of H_T have to fullfill $p_T > 30$ GeV, $|\eta| < 4.5$ and JVF > 0.5 (if $|\eta| < 2.5$).

Another feature that discriminates top quark pair production from the Higgs boson signal is the higher invariant mass of the decay products of the former as the highest Higgs mass considered in this search is 300 GeV. The sum of the electron and muon transverse momenta and of E_T^{miss} is used as discriminating variable and is shown in Figure 5.4(d) .

The optimized selection criteria for the b-tagged event category are shown in Table 5.2. In Table 5.4 the predicted numbers of signal and background events after each selection stage are given in the b-tagged event category.

5.2.4. Mass Reconstruction with the MMC Technique

Acurate invariant mass reconstruction of a di-τ resonance is a challenging task due to the undetected neutrinos. In this analysis there are a total of four neutrinos in the final state, two from each of the τ lepton decays. The invariant mass depends on eight unknown which are the components of the total neutrino four-momenta in each of the τ lepton decays. These unknowns are constrained by the two measured component of the missing transverse energy $\vec{E}_T^{miss}$ and by the τ lepton mass M_τ via the following four equations:

$$\begin{aligned}
\vec{E}_T^{miss} &= \vec{P}_T^{mis_1} + \vec{P}_T^{mis_2} \, , \\
M_{\tau_i}^2 &= m_{mis_i}^2 + m_{vis_i}^2 + 2\mathbf{P}_{vis_i} \cdot \mathbf{P}_{mis_i} \, ,
\end{aligned} \tag{5.1}$$

where i=1,2 distinguish the two τ leptons. $\vec{P}_T^{mis_i}$, m_{mis_i} and $\mathbf{P}_{mis_i}$ are the transverse momentum vector, the invariant mass and the four momentum of the neutrino pair originating from the decay of the i-th τ lepton. $\mathbf{P}_{vis_i}$ and m_{vis_i} are the known four momenta and mass of the charged lepton from the i-th τ lepton decay. The remaining four degrees of freedom can be further constrained, assuming for example that the neutrinos are collinear with the electron or muon from the same τ lepton decay. This so-called collinear approximation, however, leads to rather limited mass resolution.

In this analysis, the so-called "Missing Mass Calculator" (MMC) algorithm is used to determine the most likely invariant mass of the di-τ system for a given event topology. The implementation of the MMC method in this search is based on [131]. The MMC algorithm solves the equations 5.1 for a set of grid points in a four-dimensional parameter space. The four independent variables are chosen to be $m_{mis_i}^2$ and $cos\theta_i^*$. Where θ_i^* is the angle between the τ lepton and the charged lepton originating from its decay. The di-τ invariant mass in each event is calculated for each grid point of the parameter space. Each solution is weighted by the probability for that parameter configuration determined by Monte Carlo simulation using the PYTHIA generator supplemented by the TAUOLA package. The invariant mass $m_{\tau\tau}^{MMC}$ of the di-τ system is then estimated as the maximum of the weighted invariant mass distribution from all grid points.

The accuracy of the invariant mass obtained with the $m_{\tau\tau}^{MMC}$ method depends strongly on the resolution of the missing transverse energy measurement. To improve the E_T^{miss} resolution, a scan of a six-dimensional parameter space is performed in a similar manner as described above. For this purpose, the absolute value of $\vec{E}_T^{miss}$ is also considered unknown and a scan is performed over all possible values constrained by the measured E_T^{miss} and its corresponding uncertainty.

Figure 5.5 shows the $m_{\tau\tau}^{MMC}$ invariant mass distribution after the common selection and after the event categorisation.

5.3. Background Prediction and Validation

In this section the strategies for the prediction of the background contributions and validation of these predictions are described. Monte Carlo simulation is extensively used to model the kinematical properties of the signal and background processes. However, since the simulation is prone to systematic uncertainties due to a non-perfect description of pileup effects, the underlying event and the detector performance, the QCD multi-jet and $Z/\gamma^* \rightarrow \tau\tau$ background contributions are estimated using dedicated signal-free control data samples as described in sections 5.3.2 and 5.3.3. The contributions of the other background processes, such as $t\bar{t}$, single top quark, diboson, $Z \rightarrow ll$ + jets (where $l = e, \mu$) and W + jets, are estimated from simulation. Because of the relatively large contribution of $t\bar{t}$ background, a study to validate this background prediction has been performed as described in section 5.3.1.

Good agreement between data and background prediction is found after the common selection as can be seen in Figures 5.4 and 5.6.

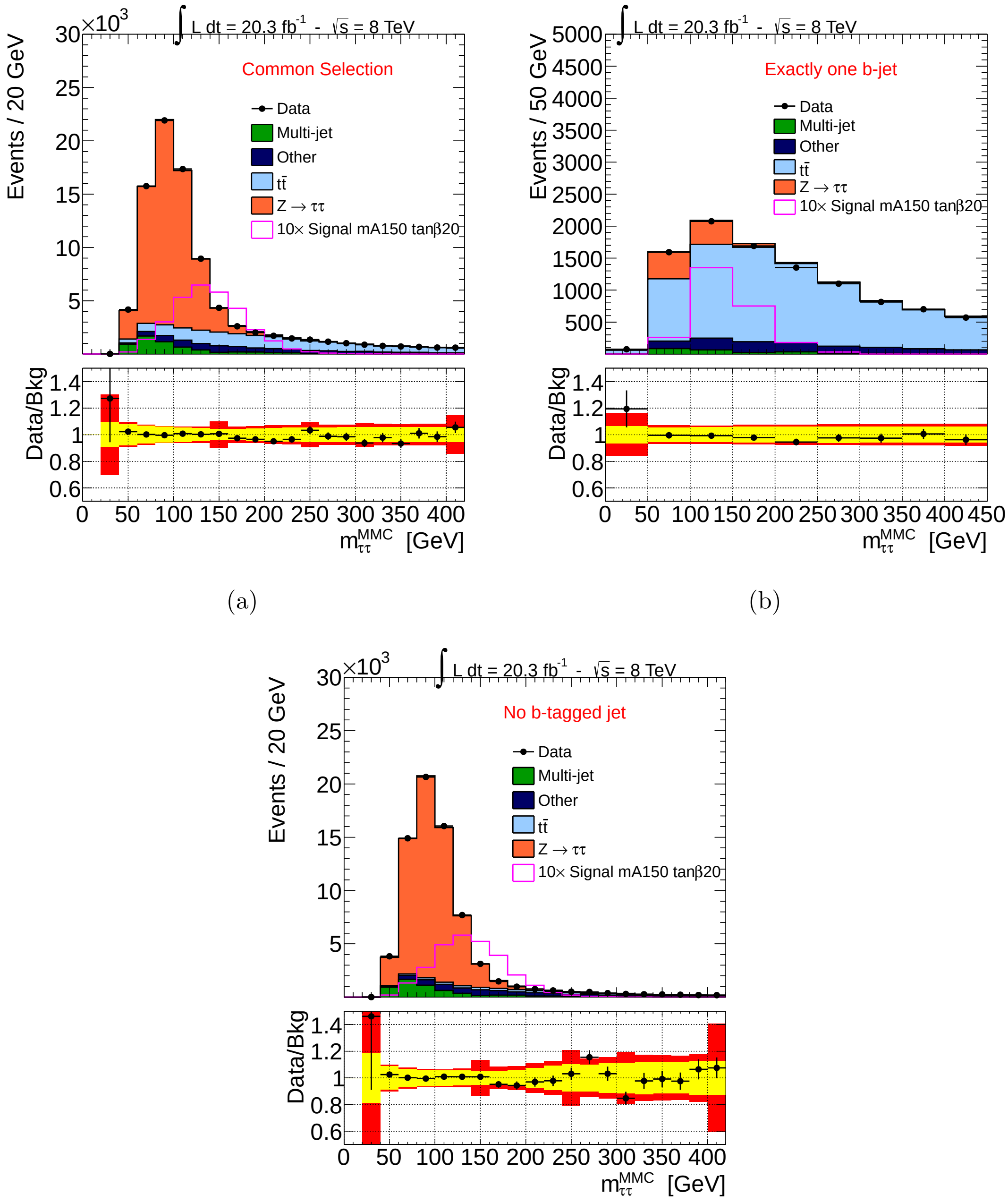

(a)

(b)

(c)

Figure 5.5.: Observed and expected distribution of the invariant di-τ mass estimate $m_{\tau\tau}^{MMC}$ at different stage of the analysis: (a) after the common selection, (b) after requiring exactly one b-tagged jet and (c) for the b-vetoed sample. The predictions of the background model is compared to the data (as in Figure 5.4).

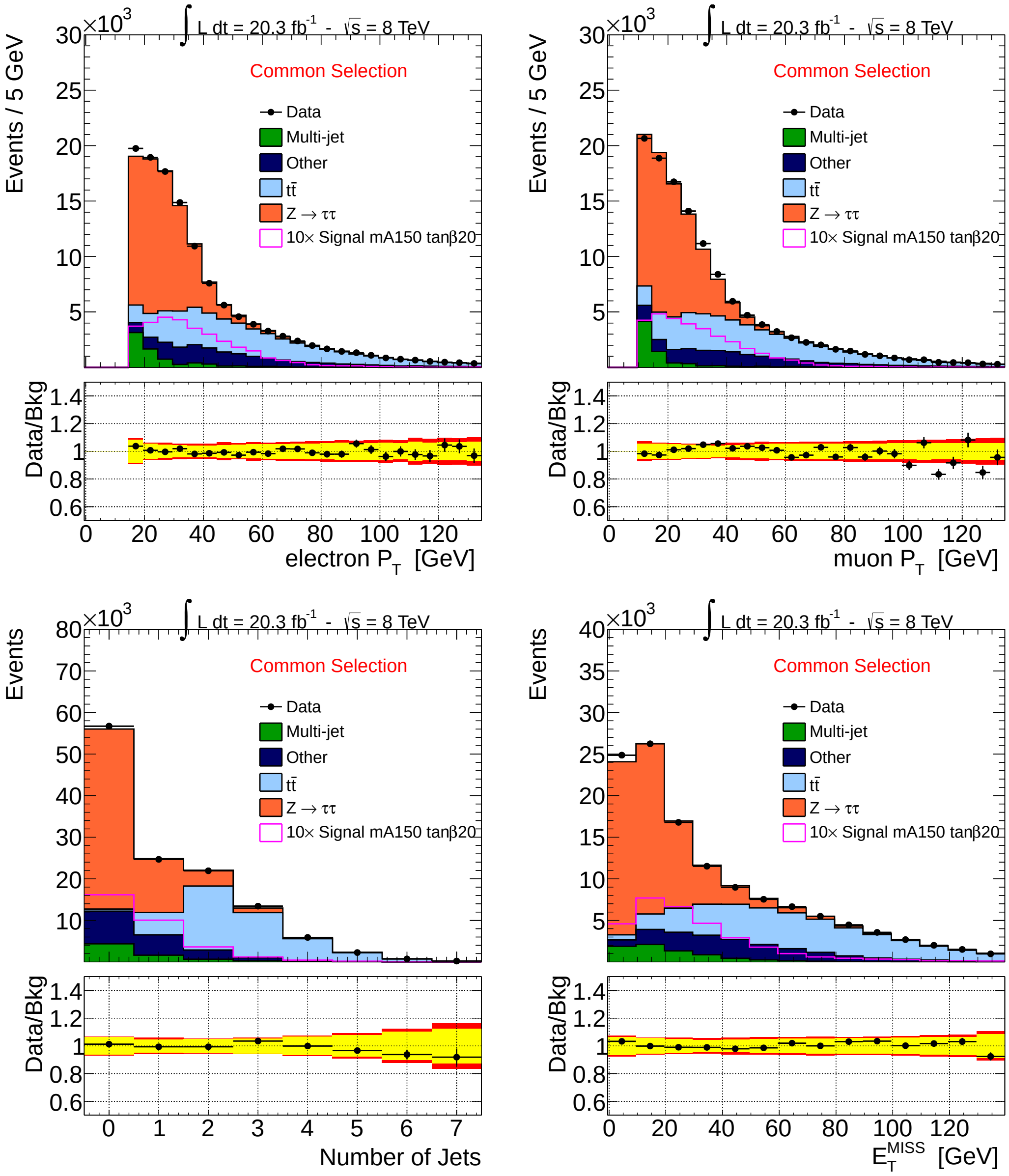

Figure 5.6.: Observed and expected distributions of kinematical variables after the common selection. The predictions of the background model are compared to data (as in Figure 5.4).

5.3.1. Validation of the $t\bar{t}$ Background Simulation

The background contribution from top quark pair production is estimated using the POWHEG-PYTHIA Monte Carlo generator. Since this is one of the major background processes for this analysis, a careful validation of the predicted contribution is needed. For this purpose a signal-depleted data sample is enriched with $t\bar{t}$ events by requiring the presence of exactly two b-tagged jets after the common selection criteria. Figures 5.7 and 5.8 show the distributions of kinematical variables and of the discriminating variables for this data sample. Good agreement between data and Monte Carlo prediction is found with a ratio of observed to predicted numbers of $t\bar{t}$ events of $0.998 \pm 0.011(\text{stat.}) \pm 0.110(\text{sys.})$. The total systematic uncertainty in the ratio is dominated by the uncertainty in the b-tagging efficiency.

5.3.2. Measurement of Multi-jet Background

QCD multi-jet production represents an important background, especially in the b-vetoed event category, due to its high cross-section and the relatively low lepton p_T threshold used in this analysis. The contribution of this background is evaluated by the so-called ABCD data-driven technique. In the ABCD method, the data events after the common selection are split into four sub-samples: the signal sample (A) defined by the event selection criteria described in Section 5.2 and three signal-depleted control data samples (B,C,D) which are mutually exclusive and enriched in multi-jet events. The three control data samples are defined by inverting the requirements on the relative sign of the electron and muon charge and on the isolation criteria. Both the calorimetric and tracking isolation criteria described in Section 5.2.1 are inverted for electron and muon with respect to the nominal values, thus defining the so-called non-isolated leptons. The data are divided into four samples of events with leptons of opposite sign charge (OS) or same sign charge (SS) and respectively isolated or non-isolated, as summarised in Table 5.5.

The ABCD method assumes that there is no correlation between the requirements of relative charge sign and of lepton isolation in QCD multi-jet events. In this case, the number N_A of QCD multi-jet events in the signal sample A can be estimated from the yields N_B, N_C and N_D of multi-jet events in the control samples B, C

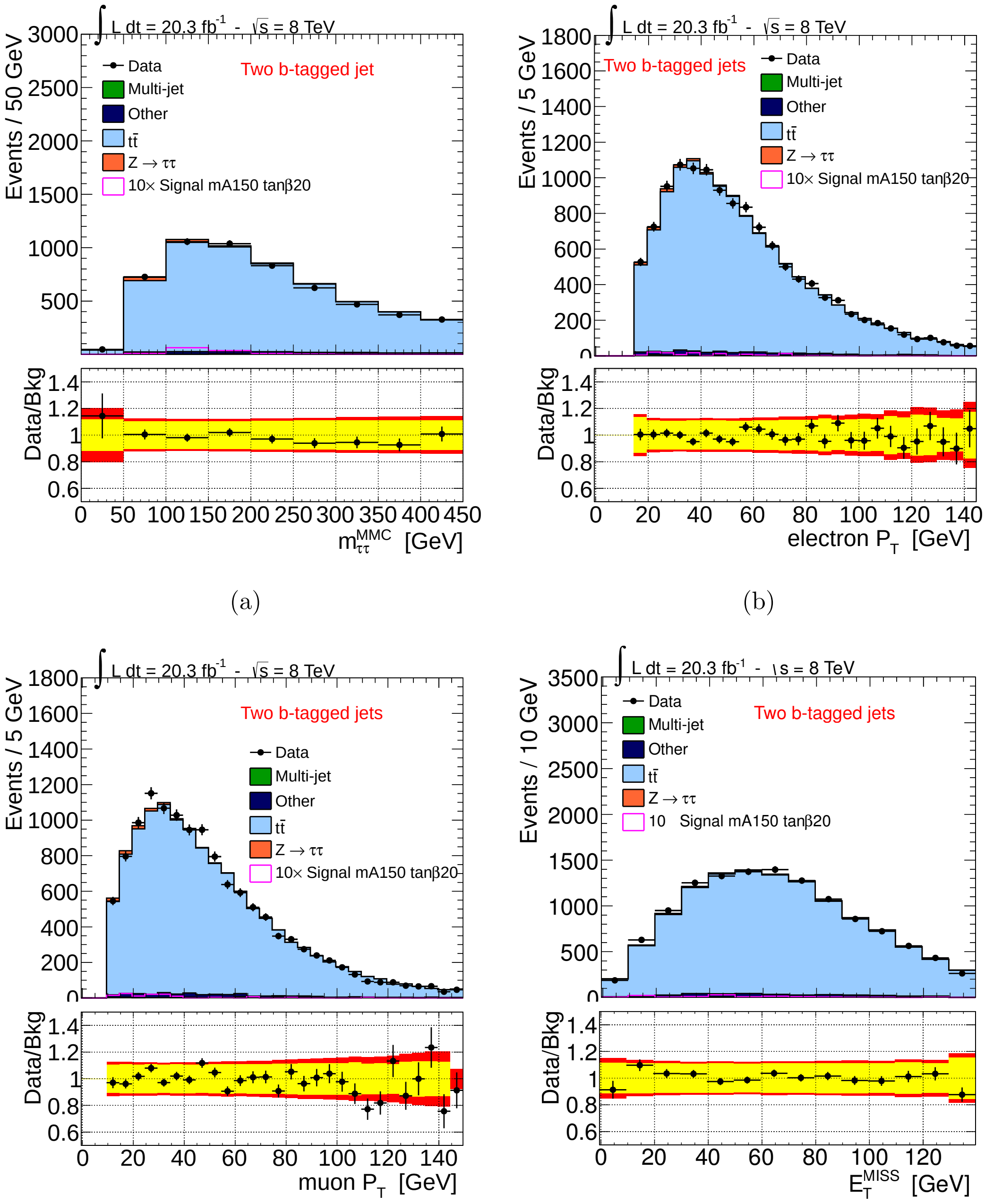

(a) (b)

(c) (d)

Figure 5.7.: Observed and expected distributions in the $t\bar{t}$ validation sample of (a) the di-τ invariant mass estimated with $m_{\tau\tau}^{MMC}$, (b) the electron and (c) the muon transverse momentum, (d) the missing transverse energy E_T^{miss}. The predictions of the background model are compared to data (as in Figure 5.4).

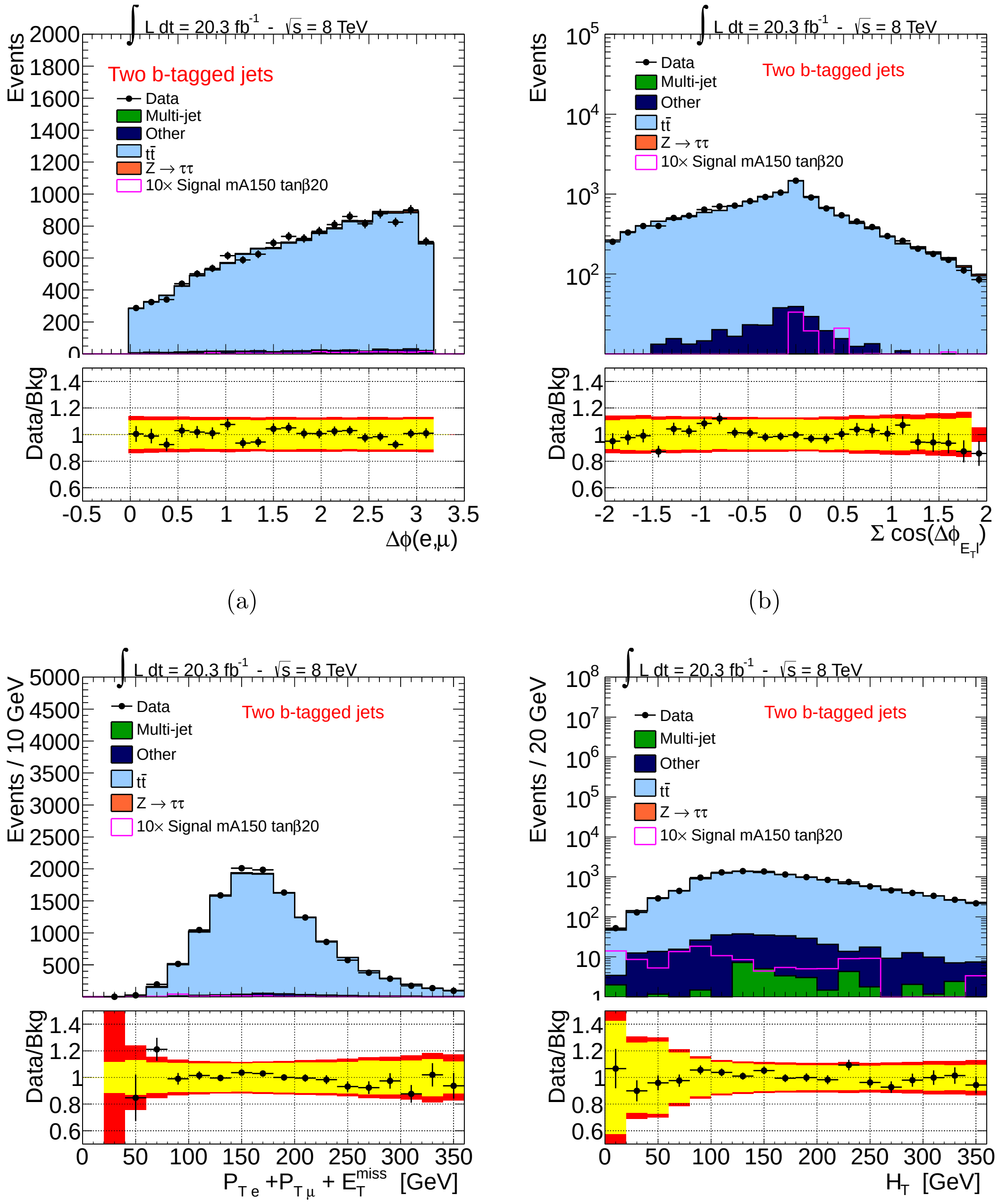

(a)

(b)

(c)

(d)

Figure 5.8.: Observed and expected distributions of the discriminating variables (a) $\Delta\phi(e-\mu)$, (b) $\sum\cos\Delta\phi$, (c) $p_{T\mu}+p_{Te}+E_T^{miss}$ and (d) H_T in the $t\bar{t}$ validation sample. The predictions of the background model are compared to data (as in Figure 5.4).

Table 5.5.: Control data samples for the measurement of the QCD multi-jet background. The samples are defined by requirements on the relative sign of the two lepton charges (OS,SS) and on the lepton isolation (isolated or non-isolated). See text.

Data sample	Relative lepton charge	Lepton isolation
A (signal sample)	OS	isolated
B	SS	isolated
C	OS	non-isolated
D	SS	non-isolated

and D using the equation

$$N_A = N_B \times \frac{N_C}{N_D} = N_B \times R_{QCD}\,. \tag{5.2}$$

To obtain the QCD multi-jet event yields in the control data samples, the contributions of contaminating electroweak (W+jets, Z+jets and dibosons) and top quark ($t\bar{t}$, single top quark production) processes are subtracted based on the prediction from simulation. Tables 5.6 and 5.7 show the observed event yields in the control samples at different stages of the event selection along with the non-QCD background predictions which are subtracted. Contamination by signal events has been evaluated in all three control samples for different m_A and $\tan\beta$ values in the range considered in this analysis. The highest signal contamination of 0.2% is observed[1] in sample B for $m_A = 300$ GeV and $\tan\beta = 50$.

The shapes of the kinematical distributions in QCD multi-jet events are modelled by the data sample B which is expected to have similar kinematical properties as the signal sample. A drawback of this choice is a rather low number of events and a higher contamination with non-QCD process compared to samples C and D. Sample B is chosen to avoid bias in the shapes due to the isolation requirements at the trigger level, since the single-electron trigger already imposes isolation requirements. Figure 5.9 shows the comparison of the electron p_T distributions in samples B and D. In the latter, high-p_T electrons are suppressed as they do not pass the trigger selection. The trigger isolation requirement could in principle also bias the ratio R_{QCD}. This possibility has been investigated in a dedicated study

---

[1] This signal contamination originates mainly from the production in association with b-quarks and, as it scales with the cross section, it is an order of magnitude smaller for $\tan\beta = 20$.

Table 5.6.: Numbers of observed events and the non-QCD contributions at different stages of the event selection for the b-vetoed category. The error on R_{QCD} ratio is statistical only.

Event Selection		B	C	D	R_{QCD}
Common Selection	Data	6189	604628	312901	1.929 ± 0.004
	non-QCD	2510 ± 180	1090 ± 30	730 ± 35	
B-veto	Data	5673	558217	284847	1.960 ± 0.004
	non-QCD	2220 ± 180	710 ± 30	415 ± 30	
$\Delta\phi_{e,\mu}$	Data	4610	532583	271404	1.962 ± 0.005
	non-QCD	1700 ±170	580 ± 30	345 ± 30	
$\sum\cos\Delta\phi$	Data	3417	486747	247712	1.965 ± 0.005
	non-QCD	1120 ± 100	370 ± 20	230 ± 20	
$m_{\tau\tau}^{MMC} > 0.$	Data	3177	479967	244276	1.965 ± 0.005
	non-QCD	1000 ± 100	300 ± 17	190 ± 20	

Table 5.7.: Numbers of observed events and the non-QCD contributions at different stages of the event selection for the b-tagged category. The error on R_{QCD} ratio is statistical only.

Event Selection		B	C	D	R_{QCD}
Common Selection	Data	6189	604628	312901	1.929 ± 0.004
	non-QCD	2510 ± 180	1090 ± 30	730 ± 35	
B-tag	Data	419	44619	27257	1.64 ± 0.01
	non-QCD	215 ± 10	310 ± 12	277 ± 13	
$\Delta\phi_{e,\mu}$	Data	230	38810	23316	1.67 ± 0.01
	non-QCD	104 ± 6	200 ± 10	175 ± 7	
$\sum\cos\Delta\phi$	Data	149	31379	18779	1.67 ± 0.02
	non-QCD	67 ± 5	127 ± 8	114 ± 6	
$\sum H_T$	Data	83	27781	15626	1.78 ± 0.02
	non-QCD	23 ± 4	25 ± 3	22 ± 3	
$p_{T\mu} + p_{Te} + E_T^{miss}$	Data	71	27735	15590	1.78 ± 0.02
	non-QCD	10 ± 3	22 ± 3	18 ± 2	
$m_{\tau\tau}^{MMC} > 0.$	Data	70	27634	15522	1.78 ± 0.02
	non-QCD	9 ± 3	20 ± 3	17 ± 2	

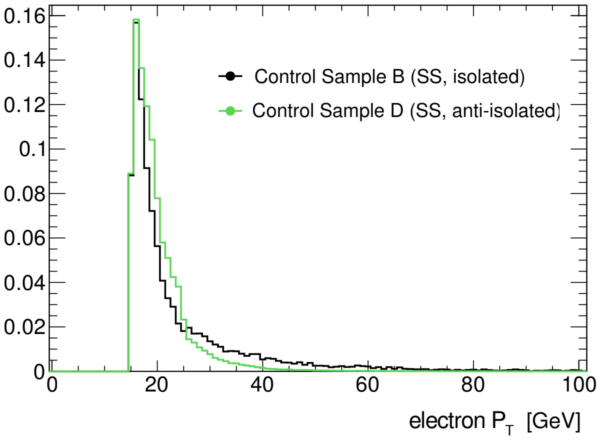

Figure 5.9.: Comparison of the electron p_T distributions in control samples B and D, showing the bias due to the trigger. The histograms are normalised to the same area.

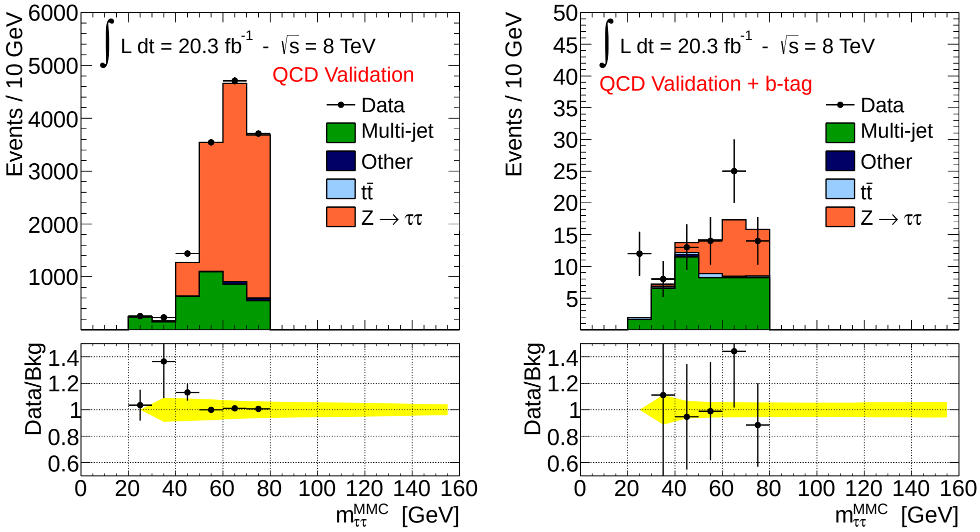

Figure 5.10.: $m_{\tau\tau}^{MMC}$ distributions for the QCD validation samples defined in Section 5.3.2 without (left) and with (right) additional requirement of exactly one b-tagged jet in the final state. The error bars and the yellow band indicate the statistical and systematic uncertainties, respectively.

discussed in Appendix A. To good approximation, the trigger effects cancel in the ratio R_{QCD} and no additional systematic uncertainty arises.

To test the predictions of the ABCD method, an additional validation sample has been defined with the following criteria applied after the common selection:

- $E_T^{miss} < 20$ GeV,
- $H_T < 70$ GeV and $p_{T\mu} + p_{Te} + E_T^{miss} < 50$ GeV,
- $0 < m_{\tau\tau}^{MMC} < 80$ GeV .

These requirement are designed to enhance the multi-jet background contribution with respect to $Z/\gamma^* \to \tau\tau$ keeping the final state kinematics as similar as possible to the signal sample. Figure 5.10 shows the $m_{\tau\tau}^{MMC}$ distribution for this validation sample with and without the b-tagging requirements. Agreement between data and the background predictions is found within statistical and detector-related systematics uncertainty.

Systematic uncertainties are assigned on the scaling factor R_{QCD} and on the shape of the discriminating variable $m_{\tau\tau}^{MMC}$ to take into account any correlation between the isolation and the relative charge of the leptons as detailed in Section 5.4.

5.3.3. $Z \to \tau\tau$ + Jets Background Measurement

The $Z/\gamma^* \to \tau\tau$ production is the main source of background in this analysis and needs to be well understood. Unfortunately, for a light Higgs boson, it is impossible to fully discriminate between $Z/\gamma^* \to \tau\tau$ decays and the signal because of the similarity of the final state, a dedicated signal-free data control sample, thus, cannot be defined. However, thanks to the small Higgs boson coupling to muons, $Z/\gamma^* \to \mu\mu$ events from data provide a good starting point to model $Z/\gamma^* \to \tau\tau$ events. A hybrid approach relying on data and simulation known as "embedding" is used for this purpose. $Z/\gamma^* \to \mu\mu$ event candidates are selected in data. Each of the two muons from the Z decay is then substituted by the decay products from a simulated decay of a τ lepton, which has the same kinematical properties as the muon. The energy deposits in the calorimeters and the reconstructed tracks within a cone around the muon are subtracted in the data and substituted by the simulated τ lepton decay. Further details on the embedding technique can be found in [91, 92].

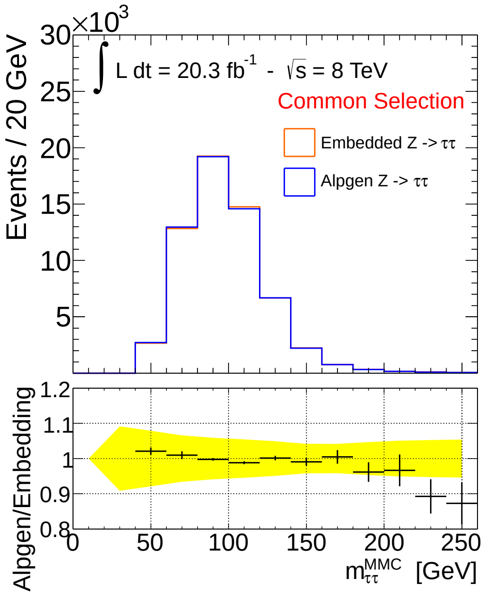

Figure 5.11.: Comparison of the $m_{\tau\tau}^{MMC}$ distributions obtained from the ALPGEN $Z/\gamma^* \rightarrow \tau\tau$ simulation and from the embedding technique after the requirements of th common selection has been applied. The yellow bad indicates the total systematic uncertainty relative to the ALPGEN simulation sample.

As the trigger requirement are not simulated in the embedded samples, only the shapes of kinematical variables distribution are modelled by the embedding, while the $Z \rightarrow \tau\tau$ event yield is normalised to the ALPGEN $Z/\gamma^* \rightarrow \tau\tau$ background prediction after the common selection. Furthermore, a set of corrections described in [93] are applied as event weight to recover the original $Z/\gamma^* \rightarrow \mu\mu$ distribution of kinematical variable from the data biased by a muon trigger. Subsequently, the trigger and reconstruction efficiency of the $e\mu + 4\nu$ final state are emulated by means of event weights.

The embedding technique has been validated in several studies detailed in [91,93] demonstrating reliable description of the data. Figure 5.11 shows the excellent agreement between the $m_{\tau\tau}^{MMC}$ distributions of embedded and simulated $Z/\gamma^* \rightarrow \tau\tau$ events. On the other hand, other important variables, such as the E_T^{miss} and the number of b-jets in the final state, are better described by the embedded rather than the simulated $Z/\gamma^* \rightarrow \tau\tau$ sample as shown in Figure 5.12. This is expected and is due to the imperfect modelling of these variables in the simulation.

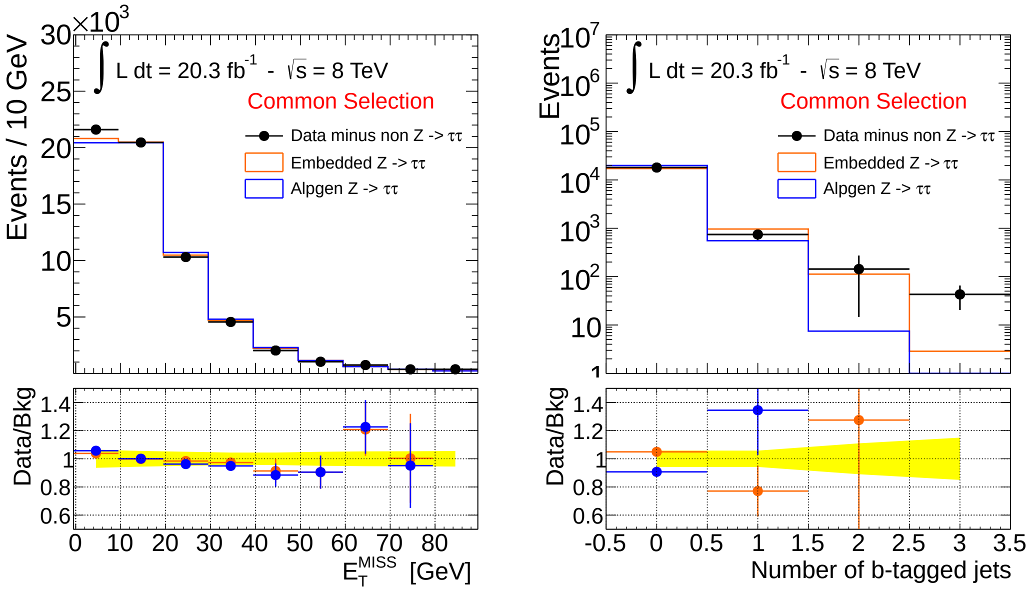

Figure 5.12.: Comparison of the E_T^{miss} (left) and b-tagged jet multiplicity (right) distributions in embedded and in ALPGEN $Z/\gamma^* \to \tau\tau$ events after the common selection. Data are superimposed after subtracting the contributions of non-$Z/\gamma^* \to \tau\tau$ processes.The yellow band indicates the total systematic uncertainty of the ALPGEN simulation.

	Embedded event yield in $t\bar{t}$ control sample	Transfer factor	Estimated events in signal sample	Contamination
b-taged	84 ± 9	$(2.6 \pm 0.1) \times 10^{-2}$	2.2 ± 0.2	0.5 %
b-vetoed	84 ± 9	$(1.74 \pm 0.02) \times 10^{-1}$	15 ± 2	0.03 %

Table 5.8.: Evaluation of the $t\bar{t}$ contamination in the embedded $Z \to \tau\tau$ sample requiring a two b-tagged jets. The transfer factor from the validation sample to the signal sample is obtained from simulation.

	Embedded event yield in QCD control sample C	Transfer factor	Estimated events in signal sample	Contamination
B-tag	12 ± 3	$(7 \pm 1) \times 10^{-3}$	$(8.4 \pm 0.3) \times 10^{-2}$	0.03 %
B-veto	390 ± 20	$(2.5 \pm 0.1) \times 10^{-2}$	10.0 ± 0.5	0.02 %

Table 5.9.: Evaluation of the QCD multi-jet contamination in the embedded $Z \to \tau\tau$ sample requiring OS non-isolated leptons (sample C). The transfer factor $R^{\mu\mu}_{QCD}$ extrapolates the event yield measured in control sample C to the signal sample (see text).

The embedding method uses selected $Z/\gamma^* \to \mu\mu$ data events. The $Z/\gamma^* \to \mu\mu$ selection criteria assure a pure $Z/\gamma^* \to \mu\mu$ sample, however, further event selection criteria used in this analysis, for example the b-tagging requirements, can enhance the contamination of this sample. Dedicated studies have been made to estimate the $t\bar{t}$ and QCD multi-jet contamination in the embedded sample. The $t\bar{t}$ contamination is estimated by evaluating the yield of embedded $Z \to \tau\tau$ events with the additional requirement of two b-tagged jets as described in Section 5.3.1. These events are assumed to originate solely from $t\bar{t}$ production and the corresponding yield in the signal sample is determined by extrapolation using the simulation. Table 5.8 summarises the estimated top quark contamination in the embedded $Z \to \tau\tau$ sample separately for the two event categories. The multi-jet contamination is estimated in a similar way starting from the yield of embedded events in sample C of the ABCD method. It is assumed that all events in this validation sample are QCD multi-jet events. The QCD multi-jet contamination of the embedded events in the signal region A is estimated as

$$N_A^{QCD-emb} = N_C^{QCD-emb} \times \frac{N_B^{\mu\mu}}{N_D^{\mu\mu}} = N_B \times R^{\mu\mu}_{QCD} \,. \tag{5.3}$$

The transfer factor $R^{\mu\mu}_{QCD}$ is evaluated using a di-muon final state with the same kinematical selection criteria as for the $Z/\gamma^* \to \mu\mu$ candidates used for the embedding procedure. Table 5.9 shows the estimated contamination of embedded sample with QCD multi-jet events which is considered negligible.

5.4. Systematic Uncertainties

In this section the systematic uncertainties for the measurement of this thesis are discussed. To account for differences in the actual and simulated detector response, corrections are applied at the level of object reconstruction and of event selection as described in Chapter 4. The detector-related systematic uncertainties due to these corrections are addressed in Section 5.4.1. For all processes whose contributions are predicted by simulation, also theoretical uncertainties related to cross-section calculation and to the acceptance of the selection criteria have been taken into account as described in section 5.4.2 . The Systematic uncertainties due to background measurements using dedicated control data samples are described in Sections 5.4.3 and 5.4.4 .

Each source of systematic uncertainty can contribute separately to the uncertainties in the final event yield and in the shape of the $m_{\tau\tau}^{MMC}$ distribution which is used as final discriminating variable in the statistical interpretation of the data. Systematic uncertainties affecting the shape of the mass distribution are documented in Appendix C.2. Uncertainties in the shape of the $m_{\tau\tau}^{MMC}$ distribution are found to be significant only for the embedded sample in the b-vetoed category, for all other backgrounds these uncertainties are found to be negligible. Systematic uncertainties which do not affect the shape of the mass distribution and have an impact on the event yield of less than 0.5% for each process are neglected.

5.4.1. Detector-Related Systematic Uncertainties

Systematic uncertainties related to object reconstruction and event-by-event corrections are derived from the calibration measurements of the relevant parameters. These parameters correspond to a nuisance parameter in the probability model used for the statistical interpretation of the data as described in Section 5.5. Each parameter is varied independently by one standard deviation according to its measured uncertainty, the impact on the event yield is evaluated for each simulated signal and background sample. In the following the detector-related uncertainties are described in more detail. Tables 5.10 and 5.11 summarise the systematic uncertainties in the predicted event yields.

Luminosity The integrated luminosity recorded during 2012 by the ATLAS detector at centre-of-mass energy of 8 TeV is measured to be 20.3 fb^{-1} [69] with an uncertainty of 2.8%.

Pileup Simulated events are re-weighted to reproduce the average number of interactions per bunch crossing $< \mu >$ as seen in data. Those event weights have an uncertainty which is propagated to each simulated sample.

The Trigger Efficiency is corrected in simulation to match on average the one observed in data. The correction weights and their uncertainties are evaluated as a function of p_T and η of the leptons. Systematic uncertainties in the single-electron and the electron-plus-muon trigger efficiencies are taken into account independently and are in the range of 1-2%.

For the embedded $Z \to \tau\tau$ sample, the trigger is emulated by applying weights depending on the p_T and η of the leptons. These weights have similar uncertainties as the ones described above. Trigger efficiency uncertainties for the embedded sample are considered uncorrelated with the ones of other samples.

Electrons Two sources of uncertainty in the electron reconstruction are considered: the first related to electron identification and reconstruction efficiencies ("Electron ID") which range approximately from 1-2% depending on the transverse momentum of the electron, the second related to electron energy scale and resolution, both in the range of 0.3-3% depending on the pseudorapidity of the electron. The energy scale uncertainties are described by six nuisance parameters [107]. Only a few of them gives a non-negligible contribution to the systematic error. Two of them affect the shape of the $m_{\tau\tau}^{MMC}$ distribution and are considered independently: one is related to the electron momentum measurement from $Z \to ee$ data ("Electron Zee") and the other related to the reconstruction of low momentum electrons ("Electron LOWPT"). All other uncertainties related to energy scale and resolution are combined quadratically ("Electron E").

Muons The uncertainty in the muon identification efficiency depends on the charge and momentum of the muon. Typically these uncertainties are on the order of a fraction of percent, and are referred to as "Muon ID". The uncertainties in the muon energy scale and resolution are considered independently for the inner detector and muon spectrometer measurements and are then added in quadrature (”Muon E”).

τ-Jets Jets from hadronically decaying τ leptons are vetoed in this analysis. Uncertainties in both the τ-jet energy scale and the identification efficiency have been investigated and were found to be negligible.

Jets The systematic uncertainties in the jet energy scale (JES) are described by multiple sets of nuisance parameters [118] related to different effects and jet energy components, for example pileup effects and the flavour composition of the jets. The overall uncertainty in the JES ranges from 3 to 7% depending on p_T and η of the jet. The overall impact of the JES uncertainty on the event yields as shown in Tables 5.10 and 5.11 is determined adding all contribution in quadrature, while in the statistical interpretation of data those uncertainties are considered independently. Systematic uncertainties due to the jet energy resolution (”Jet Resolution”) are obtained by smearing the jet energy according to the measured uncertainty which ranges from 10 to 20% depending on the jet direction.

b-Tagging Corrections are applied to simulation to match the b-tagging efficiency observed in data. Uncertainties on the knowledge of the b-tagging efficiencies for the 70% $\epsilon_b^{t\bar{t}}$ working point of the MV1 b-tagger are considered [122, 123]. These uncertainties range from 5-10% depending on the p_T of the jet. The effect of those uncertainties is evaluated independently for the b-quark, c-quark and light or gluon initiated jets and referred to respectively as ”B Eff”, ”C Eff” and ”L Eff”. The tagging and mis-tagging efficiency uncertainties are considered to be fully anti-correlated.

Missing Transverse Energy The effect of the energy scale uncertainties for all physics objects is propagated to the E_T^{miss} calculation. In addition, uncertainty on the energy scale and resolution due to the remaining unassociated calorimeter energy deposits, the “soft-terms”, is considered and estimated to be of the order of 10% [124]. E_T^{miss} uncertainties are independently propagated through the analysis and are added in quadrature, this final term is referred to as the ”MET” uncertainty.

Systematic uncertainties in event yields (%), b-vetoed category					
Source	Signal bbH	Signal ggH	$Z/\gamma^* \to \tau\tau$	Top	Other
Electron ID	2.4	2.3	2.9 (**s**)	1.4	1.6
Electron E.	0.4	0.5	0.4	0.5	0.9
Electron LOWPT	0.3	0.5	0.4 (**s**)	0.0	1.2
Electron Zee	0.4	0.4	0.4 (**s**)	0.1	0.3
Muon ID	0.3	0.3	0.3	0.3	0.3
Muon E.	0.1	0.1	0.1	0.5	0.5
Trigger Single Ele.	0.6	0.6	0.5	0.9	0.9
Trigger Dilep.	1.0	1.0	1.3	0.2	0.3
Embedding MFS	-	-	0.1 (**s**)	-	-
Embedding Iso.	-	-	0.0 (**s**)	-	-
JES	0.6	0.7	-	1.0	1.2
Jet Resolution	0.5	0.3	-	0.6	0.3
B Eff	1.8	0.0	-	12.0	0.8
C Eff	0.0	0.1	-	0.1	0.0
L Eff	0.0	0.1	-	0.2	0.1
Pileup	0.5	0.8	0.4	0.3	0.3
MET	0.2	0.8	0.1	0.2	0.5
Luminosity	2.8	2.8	2.8	2.8	2.8

Table 5.10.: Experimental systematic uncertainties in the event yields of the different simulated samples in the b-vetoed category. "Other" refers to the sum of all remaining background contribution from: $W \to \ell\nu$, dibosons, $Z \to \ell\ell$ and single top quark processes. The Signal produced in association with b-quarks and via gluon fusion is considered separately assuming $m_A = 150$ GeV and $\tan\beta = 20$ in the m_h^{mod} scenario. Uncertainty influencing the shape of the $m_{\tau\tau}^{MMC}$ distribution labelled with (**s**).

Systematic uncertainties in event yields (%), b-tagged category					
Source	Signal bbH	Signal ggH	$Z/\gamma^* \to \tau\tau$	Top	Other
Electron ID	2.3	2.6	2.8	1.8	2.0
Electron E	0.7	1.2	0.5	0.5	0.9
Electron LOWPT	0.4	0.0	0.4	0.1	0.4
Electron Zee	0.3	0.6	0.4	0.6	0.5
Muon ID	0.3	0.3	0.3	0.3	0.3
Muon E	0.5	0.8	0.1	0.1	0.2
Trigger Single Ele.	0.7	0.5	0.5	0.8	0.8
Trigger Dilepton	1.0	1.2	1.4	0.6	0.6
Embedding MFS	-	-	0.0	-	-
Embedding Iso.	-	-	1.3	-	-
JES	2.7	7.3	-	10.0	7.0
Jet Resolution	1.4	6.3	-	2.9	3.0
B Eff	10.2	3.1	-	2.6	5.0
C Eff	0.2	4.3	-	0.0	1.2
L Eff	0.4	8.0	-	0.1	1.2
Pileup	0.4	0.7	0.4	0.4	0.9
MET	0.7	0.5	0.2	1.0	1.2
Luminosity	2.8	2.8	2.8	2.8	2.8

Table 5.11.: Experimental systematic uncertainties in the event yields of the different simulated samples in the b-tagged category. "Other" refers to the sum of all remaining background contribution from: $W \to \ell\nu$, dibosons, $Z \to \ell\ell$ and single top quark processes. The Signal produced in association with b-quarks and via gluon fusion is considered separately assuming $m_A = 150$ GeV and $\tan\beta = 20$ in the m_h^{mod} scenario.

Table 5.12.: Cross-section uncertainties for signal and background processes assuming $\tan\beta = 20$ for all signal samples.

Process	Generator	Uncertainty (%)
$Z \to \tau\tau/ee/\mu\mu$	ALPGEN	± 5
$t\bar{t}$	POWHEG	± 5.5
$W \to \tau\nu/e\nu/\mu\nu$	ALPGEN	± 5
single top	MC@NLO / AcerMC	± 7 / ± 13
dibosons	HERWIG	± 6
$bbA/h/H$ ($m_A \geq 120$ GeV)	SHERPA	${}^{+9}_{-20}$
$bbA/h/H$ ($m_A = 110$ GeV)	SHERPA	${}^{+9}_{-25}$
$bbA/h/H$ ($m_A = 100$ GeV)	SHERPA	${}^{+9}_{-28}$
$bbA/h/H$ ($m_A = 90$ GeV)	SHERPA	${}^{+9}_{-30}$
$ggA/h/H$ ($m_A \leq 300$ GeV)	POWHEG	± 15

5.4.2. Theoretical Uncertainties

Uncertainties on the cross-sections that have been used to normalise the contribution of simulated samples to the integrated luminosity of analyzed data are reported in Table 5.12. These uncertainties include contributions due to parton distribution functions (PDFs), the choice of the value of the strong coupling constant, the renormalisation and factorisation scales. Furthermore, the uncertainties on the signal cross-section depend on the $\tan\beta$ value, the type of Higgs boson ($A/h/H$) and its mass.

The systematic uncertainties due to Monte Carlo tuning parameters for the description of the underlying event, of lepton kinematical properties and parton density functions have been studied. Since the distribution of the invariant mass of all visible τ lepton decay products is found not to be affected by these systematic uncertainties, only the impact on the acceptance is considered. The acceptance uncertainties for the simulated ALPGEN $Z/\gamma^* \to \tau\tau$ sample, which is used for the normalisation of the embedded sample, are estimated at the common selection stage to be 4% [74]. Since additional selection criteria are applied directly to the embedded sample, no further acceptance uncertainties are considered. Acceptance uncertainties in the yield of simulated $t\bar{t}$ events are estimated to be 2% [133]. The acceptance uncertainties in diboson and single top quark production are estimated to be 2% [74].

Uncertainties in the signal acceptance have been estimated using signal samples simulated with different generator parameters. The impact on the selection of leptons, τ-jets and jets is evaluated at the particle level, prior to simulation of the detector response. This truth-level study is implemented within the Rivet framework [135], where the b-tagging is performed by identifying the b-quarks and applying weights according to the measured ATLAS b-tagging efficiencies [122]. The variation of the acceptance with respect to the nominal Monte Carlo tune has been considered as a source of systematic uncertainty. The total signal acceptance uncertainty varies from 4% to 30% depending on m_A, on the production process and event category.

5.4.3. Systematic Uncertainties of $Z/\gamma^* \to \tau\tau$ Embedded Sample

An important element of the embedding method is the subtraction of the calorimeter cells associated with the muons in the original $Z/\gamma^* \to \mu\mu$ event and their substitution with those from the simulated τ lepton decays. To make a conservative estimate of the systematic uncertainty on this procedure, the energy of the subtracted cells is scaled up or down by 30%. The analysis is repeated with those modified samples and the relative uncertainty is referred as "EMB_MFS". This uncertainty affects mainly the shape of the $m_{\tau\tau}^{MMC}$ mass distribution as shown in Figure 5.13.

In the sample of $Z/\gamma^* \to \mu\mu$ candidates used for the embedding, only a loose requirement on the muon track isolation is used. A different muon isolation requirement may affect the selected sample by modifying the topology of the event, changing the contamination with other processes or the activity in the calorimeter. To estimate the importance of these effects in the embedded sample, the muon isolation criteria used for the original $Z/\gamma^* \to \mu\mu$ sample are tightened, a looser requirement have a small impact due to the isolation requirements at the trigger level. The resulting uncertainty, referred to as "EMB_ISO", affects both the event yield and the shape of the $m_{\tau\tau}^{MMC}$ distribution of the embedded sample as shown in Figure 5.13.

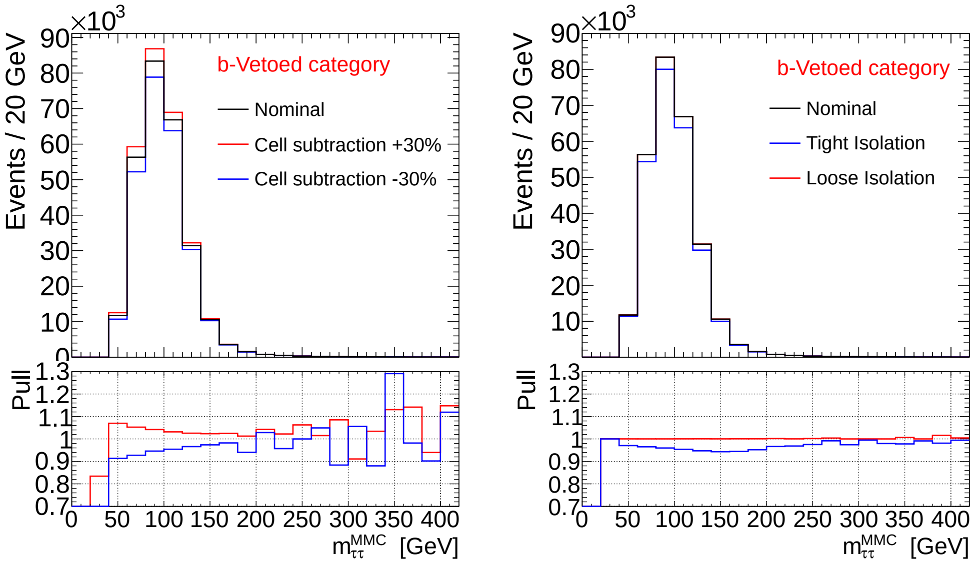

Figure 5.13.: Impact of EMB_MFS (left) and EMB_ISO (right) systematic uncertainties in the $m_{\tau\tau}^{MMC}$ distribution of embedded events. Significant uncertainty have been found only in the b-vetoed category.

Finally, because the normalisation of the embedded sample is determined from the ALPGEN simulation, the uncertainties related to the cross section calculation and the luminosity are assigned. In addition, all the discussed detector-related systematic uncertainties affecting the decay products of the simulated τ lepton decays are propagated to the embedded sample.

5.4.4. QCD Multi-Jet Systematic Uncertainties

The QCD multi-jet background is estimated via the ABCD method as described in Section 5.3.2. This technique relies strongly on the assumption that the lepton isolation variables are uncorrelated with the product of the charge signs of the two leptons. Systematic uncertainties are evaluated to take into account possible deviations from this assumption. The dependence of the ratio R_{QCD} on the lepton isolation criteria is evaluated and then compared to the uncertainties obtained with auxiliary measurements.

Figure 5.14 shows the R_{QCD} factor, i.e. the ratio of the QCD background yields in

Table 5.13.: Comparison between the transition factor R_{QCD}, R^{AB}_{QCD} and R^{iso}_{QCD} after the common selection and after b-tag or b-veto requirements on jets. The value of R^{iso}_{QCD} is calculated for a lepton isolation threshold which is twice the nominal value, while for R^{AB}_{QCD} and R_{QCD} the nominal values are given. The uncertainties are statistical only.

Selection	R_{QCD}	R^{AB}_{QCD}	R^{iso}_{QCD}
Common selection	1.929 ± 0.004	2.12 ± 0.17	2.22 ± 0.16
No b-tagged jets	1.965 ± 0.005	2.10 ± 0.16	2.22 ± 0.16
Exactly one b-tagged jet	1.78 ± 0.02	1.9 ± 0.9	2.0 ± 0.8

data samples C and D, as a function of a sliding lepton isolation threshold relative to the nominal analysis selection. The expected contamination with non-QCD background processes is subtracted from samples C and D. To estimate the uncertainty in the value of R_{QCD}, another transfer factor is defined as $R^{iso}_{QCD} = N_{\hat{A}}/N_{\hat{B}}$, where $\hat{A}$ and $\hat{B}$ are "semi-isolated" OS and SS samples with the requirement on the lepton isolation to be larger than the nominal value, but smaller than the sliding threshold defined by the X-axis of the plot. Also here the non-QCD contributions are subtracted. The semi-isolated samples $\hat{A}$ and $\hat{B}$ have been chosen because of the large contamination of the samples A and B with non-QCD background and possible signal processes. Figure 5.14 shows R^{iso}_{QCD} as a function of the relative lepton isolation threshold. The difference between R_{QCD} and R^{iso}_{QCD} in the vicinity of the nominal isolation threshold is then assigned as a systematic uncertainty in R_{QCD}. For a lepton isolation threshold of twice the nominal required value, a systematic uncertainty of 15% is found. The result are shown in Figure 5.14 after the common selection, similar results are obtained after the full selection of the two event categories as shown in Appendix A.2.

For validation of the results described above an additional measurement is performed. The transfer factor R^{AB}_{QCD} is calculated as the ratio of the estimated QCD multi-jet contributions of the samples A and B (instead of C and D). The non-QCD contributions are subtracted. Due to the large contribution of non-QCD background along with small numbers of observed events and signal contamination, this measurement is only used as cross check. Table 5.13 shows a comparison of R_{QCD}, R^{iso}_{QCD} and R^{AB}_{QCD} after the common selection and after requiring or vetoing

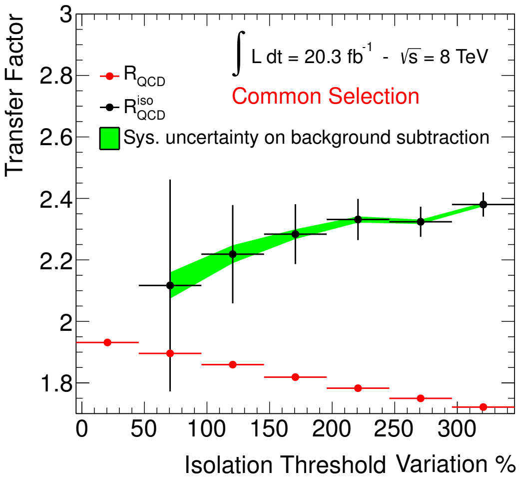

Figure 5.14.: Transfer factors R_{QCD} and R^{iso}_{QCD} (see text) as a function of the sliding lepton isolation thresholds. The thresholds are varied in percentages relative to the nominal lepton isolation threshold (value of zero on the plot). The common selection are applied.

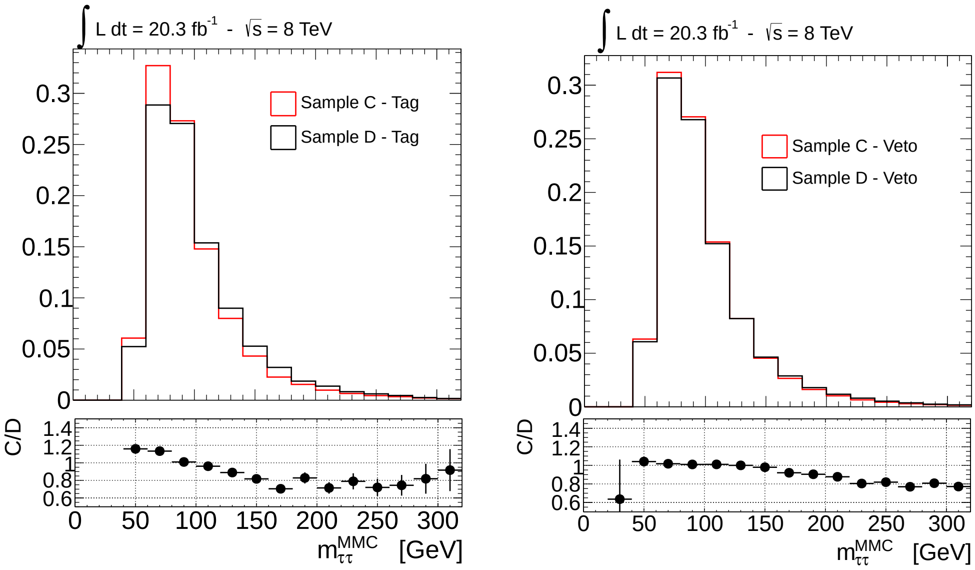

Figure 5.15.: Differences in the shape of the invariant $m^{MMC}_{\tau\tau}$ mass distribution in data samples C and D shown separately for the b-tagged and b-vetoed event categories. The data samples C and D are normalised to the same number of events.

the presence of b-tagged jets. At these selection stages the signal contamination is negligible. Good agreement is found between all three results.

The shape of the $m_{\tau\tau}^{MMC}$ distribution differs between the non-isolated OS and SS lepton samples C and D as shown in Figure 5.15, the ratio R_{QCD} is then dependent on the $m_{\tau\tau}^{MMC}$ distribution. For the mass range in which the QCD multi-jet background is relevant ($m_{\tau\tau}^{MMC} < 150$ GeV), the size of this effect is within the uncertainty in R_{QCD}, hence no correction is applied to the shape of the mass distribution in sample B. However, it is assumed that there could be the same shape difference in the isolated lepton samples. Thus, a shape uncertainty is in the mass distribution in sample B is taken into account. Further shape uncertainties due to non-QCD background subtraction are found to be negligible. The uncertainty due to the use of the isolation requirement at the trigger level is also found to be negligible as discussed in Appendix A .

5.5. Results

5.5.1. Statistical Interpretation of the Data

The statistical interpretation of data is based on the profiled likelihood ratio test statistic as for the SM Higgs boson searches [136]. The statistical procedures described in the following are implemented in the software packages described in [137–139] used for this analysis.

The Likelihood Function

The compatibility of *background only* and *signal-plus-background* hypotheses with the observed data is evaluated. The *test statistic* defined below is based on a binned likelihood function for the data set $\mathcal{D}$:

$$\mathcal{L}(\mathcal{D}\,|\,\mu,\boldsymbol{\theta}) = \prod_i \text{Pois}(n_i\,|\,\mu\cdot s_i(\boldsymbol{\theta}) + b_i(\boldsymbol{\theta}))\cdot\Gamma(\theta_i^{stat}\,|\,\beta_i)\cdot\prod_j \mathcal{G}(\theta_j^{sys}\,|\,0,1) \tag{5.4}$$

describing how likely is a certain hypothesis given the observation of the data set $\mathcal{D}$. The signal strength parameter μ allows for reproducing a continuous set of signal hypotheses with different cross-section. The value $\mu = 0$ corresponds to the background-only hypothesis. The vector $\boldsymbol{\theta}$ represents the set of *nuisance* parameters corresponding to the statistical (θ_i^{stat}) and systematic (θ_j^{sys}) uncertainties in the signal and background. The functions $s_i(\boldsymbol{\theta})$ and $b_i(\boldsymbol{\theta})$ represent the expected yield of signal and background for the bin i of the $m_{\tau\tau}^{MMC}$ distribution histograms. The function $\mathcal{G}(\theta_j^{sys} \mid 0, 1)$ is the Gaussian[2] probability density function (p.d.f.) for the nuisance parameter θ_j^{sys} with mean $= 0$ and $\sigma = 1$. The impact of the corresponding systematic uncertainty on the signal and backgrounds yields and on the shape of the $m_{\tau\tau}^{MMC}$ invariant mass distributions is evaluated separately as described in Section 5.4. The function $\Gamma(\theta_i^{stat}|\beta_i)$ is an extended gamma function[3] providing the p.d.f. for the nuisance parameter θ_i^{stat} associated to the statistical uncertainty β_i in bin i of the $m_{\tau\tau}^{MMC}$ distribution. The values of the nuisance parameter set $\boldsymbol{\theta}$ are associated with variations of the predicted signal and background event yields with respect to the nominal prediction. The Poisson distributions in equation (5.4) give the probability to observe n_i events in the bin i of the $m_{\tau\tau}^{MMC}$ distribution histogram:

$$\mathrm{Pois}(n_i \mid \mu \cdot s_i(\boldsymbol{\theta}) + b_i(\boldsymbol{\theta})) = \frac{(\mu s_i(\boldsymbol{\theta}) + b_i(\boldsymbol{\theta}))^{n_i}}{n_i!}\, e^{-\mu s_i(\boldsymbol{\theta}) - b_i(\boldsymbol{\theta})} .$$

The $m_{\tau\tau}^{MMC}$ distributions in the b-tagged and b-vetoed categories are analysed separately. The implementation of the ABCD method in the likelihood function is based on [132] and is described in more detail in Appendix C.

Statistical Combination of Results

Complementary event categories of a search channel (like the b-tagged and b-vetoed categories) can be combined in order to increase the signal sensitivity. If there are no shared events between the categories the combined likelihood function is simply the product of the likelihoods of the individual categories. The convention described in [136] is used to take into account correlations of uncertainties in the two combined categories. The systematic uncertainties are considered either as fully correlated, which means that the same nuisance parameter describes the corresponding systematic effect in both categories, or as fully uncorrelated, in which case different nuisance parameters are employed for the two categories. Partially

---

[2] Evaluation of systematic uncertainties is obtained from auxiliary measurements. From Bayes theorem, assuming a flat prior and a Gaussian distribution for the measured parameter a Gaussian posterior is obtained.

[3] The posterior of a Poisson distribution assuming a flat prior is a gamma function

correlated uncertainties are either split into components which are (un)correlated or they are defined to be either fully correlated or uncorrelated, depending on which assumption is the most conservative.

Exclusion Limit Computation

To compute the compatibility of the data with a given hypothesis, the *profiled likelihood ratio* [140]

$$\tilde{q_\mu} \;=\; -\,2\ln\frac{\mathcal{L}(\mathcal{D}\mid\mu,\hat{\boldsymbol{\theta}}_\mu)}{\mathcal{L}(\mathcal{D}\mid\hat{\mu},\hat{\boldsymbol{\theta}})} \quad \text{with the constraint} \quad 0\le\hat{\mu}\le\mu \tag{5.5}$$

is used as test statistic with the likelihood function $\mathcal{L}$ defined in equation (5.4). $\hat{\mu}$ and $\hat{\boldsymbol{\theta}}$ are the global maximum likelihood estimators for μ and $\boldsymbol{\theta}$ from fit to the dataset $\mathcal{D}$, whereas $\hat{\boldsymbol{\theta}}_\mu$ is the maximum likelihood estimator of $\boldsymbol{\theta}$ from the fit with a fixed signal strength μ. $\tilde{q_\mu}$ is increasing with increasing disagreement between data and the given μ hypothesis. Upper limits on the signal cross-section are then defined as follows:

1. The probability density functions $P(\tilde{q_\mu}\,|\,\mathrm{H}_i)$ of $\tilde{q_\mu}$ are determined under the background-only (H_0) and the signal-plus-background (H_μ) hypotheses for a given values of μ. Since the determination of these functions by means of Monte Carlo simulation of pseudo-dataset ($\mathcal{D}$) demands large computing resources, the asymptotic approximation formulae described in [140] are employed.

2. Once the p.d.f. for the background-only and signal-plus-background hypothesis are obtained, it is possible to define for a given dataset $\mathcal{D}$ two probability values (p-values) for given value of μ. These are the probabilities to obtain data less compatible with the considered hypothesis than the actual observation:

$$p_{s+b} = P(\tilde{q_\mu} > \tilde{q_\mu}^{\,observed} \mid H_\mu)$$
$$p_b = P(\tilde{q_\mu} > \tilde{q_\mu}^{\,observed} \mid H_0)$$

3. If the ratio $CL_s = p_{s+b}/p_b$ [141, 142] of the two p-values is less than a given value α, the signal-plus-background hypothesis with the corresponding μ is said to be excluded at (1 - α) CL_s confidence level. The 95% confidence level upper limit on μ, denoted as μ^{95}, is the smallest value of μ for which the $CL_s \le 0.05$.

By construction, rejecting all values of $\mu > \mu^{95}$, the signal-plus-background hypothesis will be rejected when it is true at most 5% of the time. The CL_s limits are considered conservative and protected against downward fluctuations of the data. The expected median upper-limit and its error are evaluated with the asymptotic approximation formulae under the background-only hypothesis. The results have been cross-checked using generated pseudo-data instead of the asymptotic approximation formulae for the determination of the probability density functions of $\tilde{q_\mu}$.

Significance Test of the Background Only Hypothesis

In case an excess of events is observed in a given mass range with respect to the background model predictions, the presence of a signal is quantified by the background-only p-value, i.e. the probability that the background fluctuation and gives rise to an excess of events at least as large as the observed one.

To evaluate the significance of an excess the following test statistic q_0 is chosen:

$$q_0 \;=\; -\,2\ln \frac{\mathcal{L}(\mathcal{D} \mid 0, \hat{\boldsymbol{\theta}}_0)}{\mathcal{L}(\mathcal{D} \mid \hat{\mu}, \hat{\boldsymbol{\theta}})} \quad \text{with } \hat{\mu} \geq 0\,. \tag{5.6}$$

The test statistic is defined for a given set of signal hypotheses. To determine the *local* p-value, the probability density function of q_0 is evaluated under the background-only hypothesis for a specific signal mass. Since the test of the background only hypothesis is made for many different signal masses, the chance to obtain in the full mass range a p-value smaller than a predetermined value increases. This is called *look elsewhere effect* [143] and has to be accounted for in local p-value computation. This is done by counting the number of p-value upper fluctuations over a defined threshold and downgrading the maximum local p-value by this effect, for more detail see [136, 143].

To convert the p-value into a significance Z, the convention of one sided Gaussian tail is adopted:

$$\text{p-value} = \int_Z^\infty \frac{1}{\sqrt{2\pi}} e^{-x^2/2}\, dx\,. \tag{5.7}$$

The 5σ significance ($Z = 5$) value which commonly characterises a discovery corresponds to an extremely small p-value of 2.8×10^{-7}.

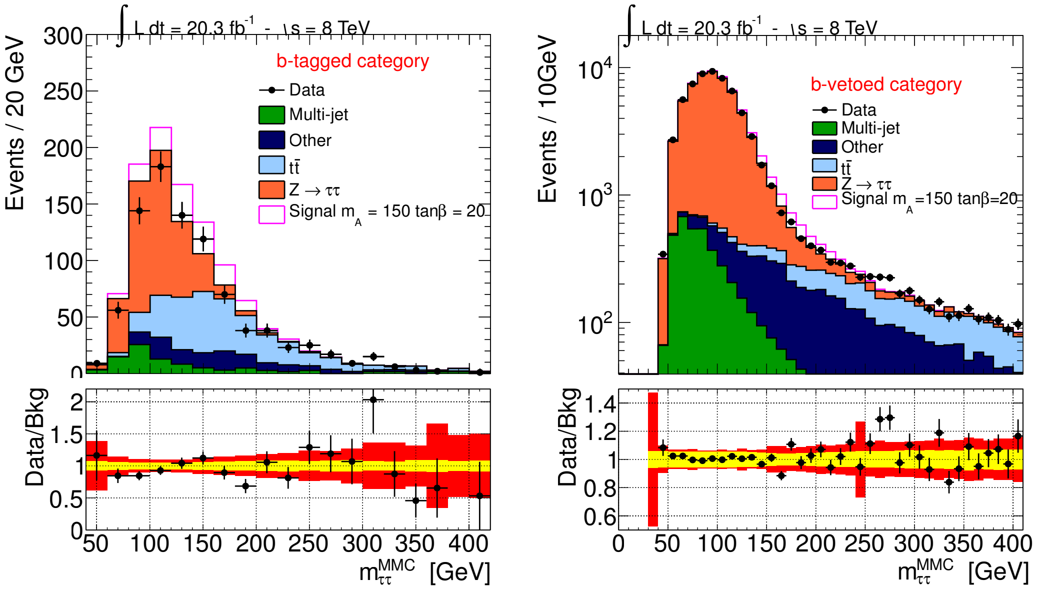

Figure 5.16.: Observed and expected distribution of the $m_{\tau\tau}^{MMC}$ for (left) the b-tagged category and (right) the b-vetoed category after the full event selections. In the ratio, the yellow and red band represents the systematic and statistical uncertainty in the background model prediction, respectively, while the error bars represent the statistical uncertainty of data (see text).

5.5.2. Expected and Observed Events

Expected and observed event yields are compared in bins of the $m_{\tau\tau}^{MMC}$ mass distribution. The bin sizes are chosen such that the number of events per bin is high enough to justify the use of the asymptotic approximation, Figure 5.16 shows the $m_{\tau\tau}^{MMC}$ distributions and Table 5.14 compares the expected and the observed event yields after the full selection in both categories. The predictions of the background model are evaluated as described in Section 5.3, the notation “Other” stands for the electroweak processes $W \to \ell\nu$, $Z \to \ell\ell$, diboson and single top quark production and the signal contribution is evaluated in the m_h^{mod} scenario for values of $m_A = 150$ GeV and $\tan\beta = 20$ considering the production of A, h and H via $gg \to A/h/H$ and $pp \to b(b)A/h/H$. Figure 5.17 and 5.18 show the distributions of different kinematical variables after the full selection in the b-tagged and b-vetoed category, respectively. Additional distribution can be found in Appendix B.

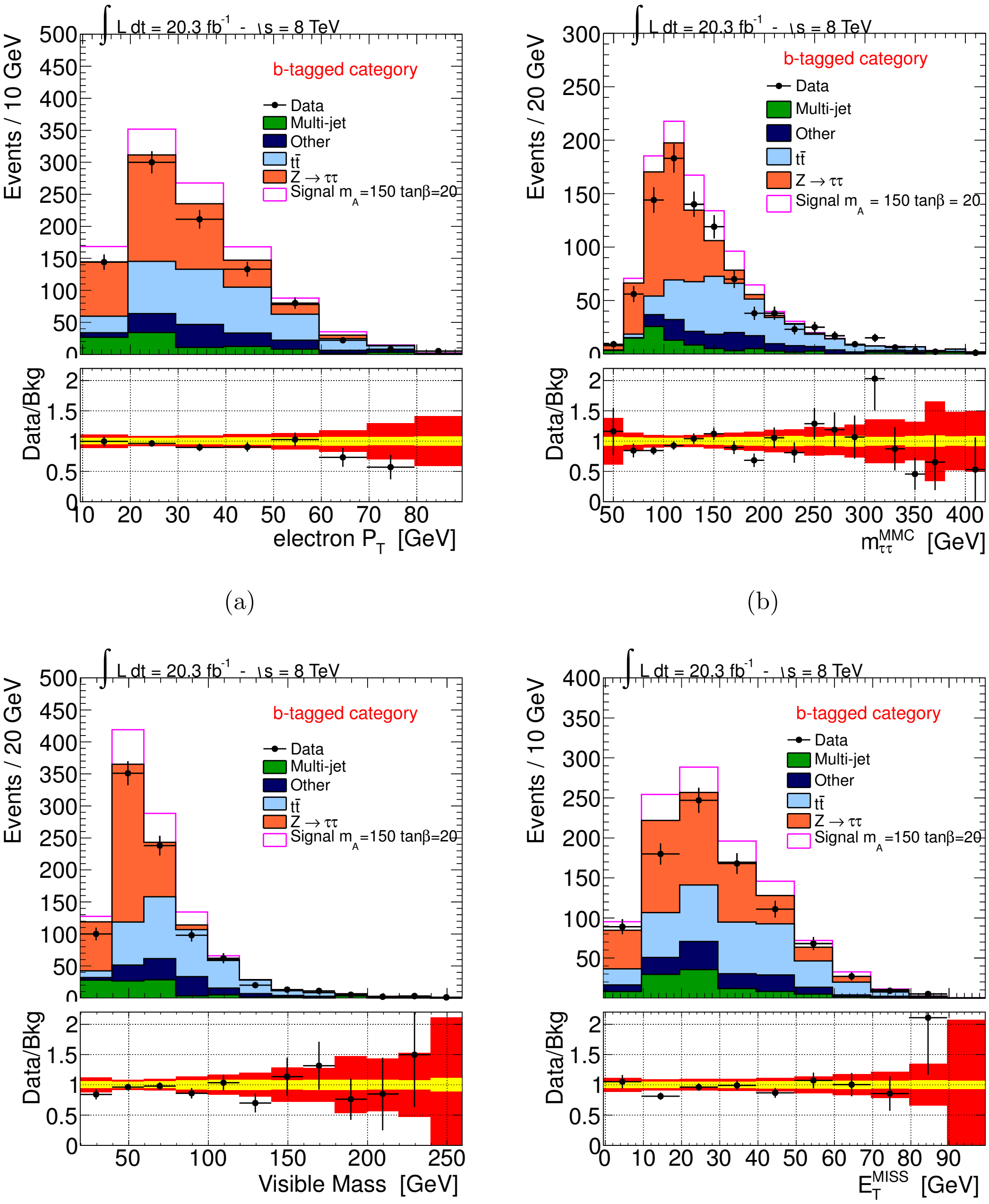

(a) (b) (c) (d)

Figure 5.17.: Observed and expected distribution for (a) electron and (b) muon p_T, (c) invariant mass of electron and muon, (d) missing transverse energy after full selection of the b-tagged category. In the ratio, the yellow and red band represents the systematic and statistical uncertainty in the background model prediction, respectively, while the error bars represent the statistical uncertainty of data (see text).

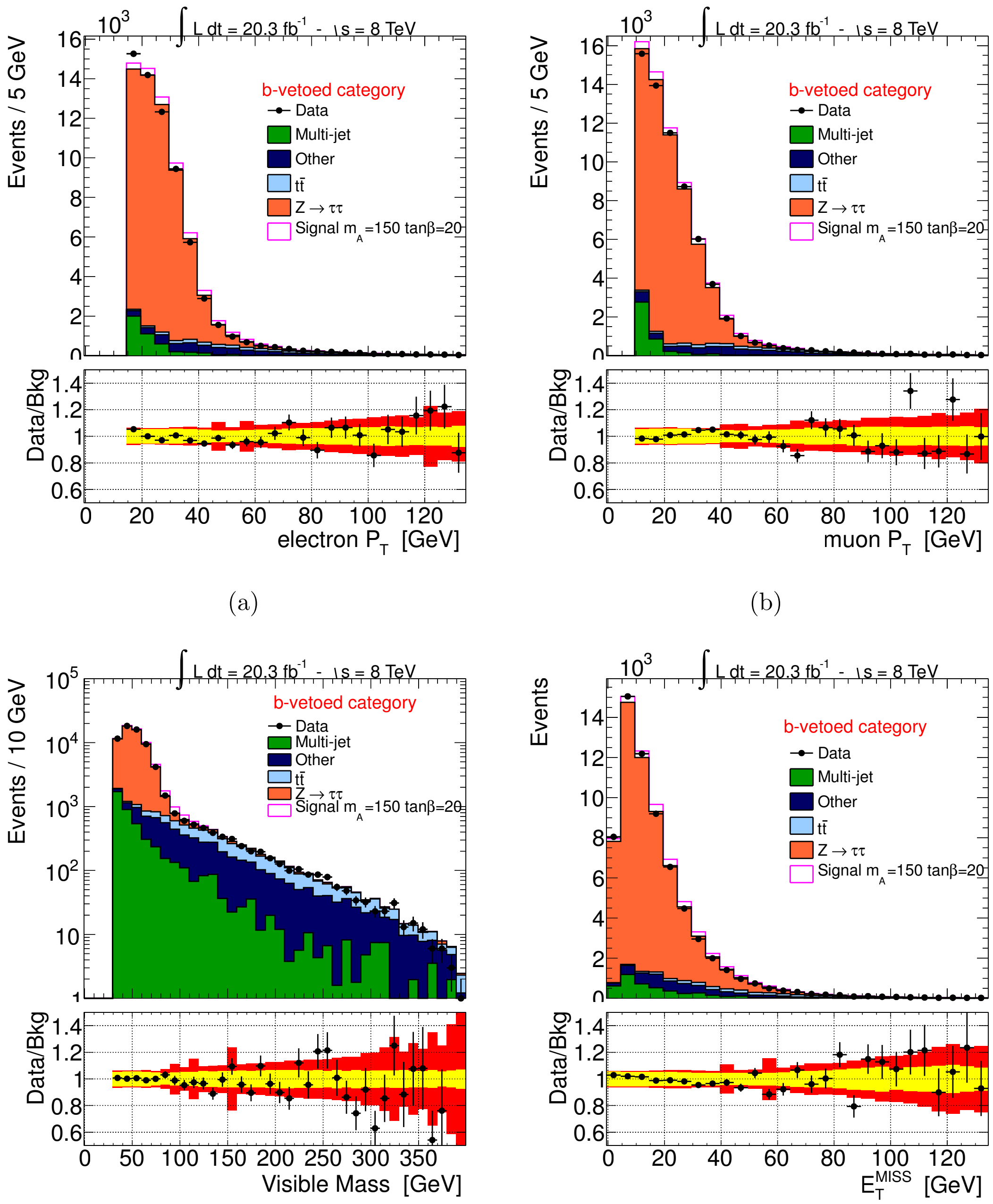

(a)

(b)

(c)

(d)

Figure 5.18.: Observed and expected distribution for (a) electron and (b) muon p_T, (c) invariant mass of electron and muon, (d) missing transverse energy after full selection of the b-vetoed category. In the ratio, the yellow and red band represents the systematic and statistical uncertainty in the background model prediction, respectively, while the error bars represent the statistical uncertainty of data (see text).

Table 5.14.: Expected and observed event yields in the b-tagged and b-vetoed event categories after the full event selection. The expected signal and background and event yields are normalised to the integrated luminosity of 20.3 fb^{-1}. The uncertainties include the statistical (first) and the systematic (second) errors.

Sample	b-tag category			b-veto category		
	N(event)	Stat.	Syst.	N(event)	Stat.	Syst.
$Z/\gamma^* \to \tau\tau$	418	± 6	$^{+27}_{-27}$	54680	± 60	$^{+3500}_{-3500}$
$t\bar{t}$	330	± 10	$^{+37}_{-35}$	2228	± 25	$^{+280}_{-300}$
Multijet	101	± 15	$^{+15}_{-15}$	4180	± 230	$^{+630}_{-630}$
Other	114	± 9	$^{+12}_{-12}$	4450	± 110	$^{+250}_{-250}$
Total	963	± 21	$^{+50}_{-50}$	65540	± 260	$^{+3600}_{-3600}$
Signal	144	± 7	$^{+24}_{-33}$	2028	± 27	$^{+150}_{-100}$
Data	904			65917		

5.5.3. Exclusion Limits on the Signal Production

The statistical procedure described in section 5.5.1 is the general one used for the SM Higgs boson search at the LHC where only the Higgs boson mass determines the signal properties. For the MSSM a complication arise since there are three neutral Higgs bosons contributing to the signal yield. In a particular scenario their masses and production cross sections are defined by the two parameters $\tan\beta$ and m_A. Thus, the procedure described above has to be repeated for each point in the $\tan\beta - m_A$ plane. Exclusion limits at 95% CLs confidence level in the m_h^{mod} scenario are derived in the $\tan\beta - m_A$ plane based on the production cross section times branching ratio for the neutral MSSM Higgs bosons ($A/h/H$) produced via $gg \to A/h/H$ and $pp \to b(b)A/h/H$ and in decays $A/H/h \to \tau\tau \to \mu e + 4\nu$. A grid has been set up in the $\tan\beta - m_A$ plane with 15 tanβ values[4] in the range between 5 and 60 and 12 m_A values[5] in the range from 90 to 300 GeV. A point

---

[4] The set of tanβ values used is 5, 8, 10, 13, 16, 20, 23, 26, 30, 35, 40, 45, 50, 55, 60

[5] The set of m_A values used is: 90, 100, 110, 120, 125, 130, 140, 150, 170, 200, 250 and 300 GeV

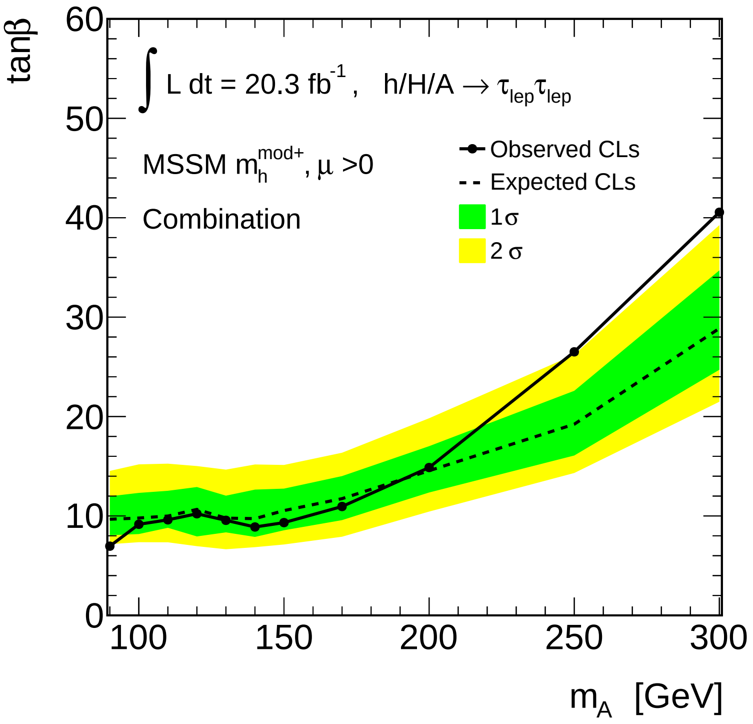

Figure 5.19.: Expected and observed exclusion limits at the 95% CL_s confidence-level for MSSM Higgs bosons production interpreted in the $m_A - \tan\beta$ parameter space of the m_h^{mod} scenario. Combined result of the b-tagged and b-vetoed category is shown.

in the $\tan\beta - m_A$ plane is excluded if $\mu^{95} \leq 1$, a linear interpolation is used to determine the excluded $\tan\beta$ value for a given m_A.

The exclusion limits in the $m_A - \tan\beta$ parameter space of the MSSM m_h^{mod} benchmark scenario are shown in Figure 5.19 for the combination of b-tagged and b-vetoed category, while Figure 5.21 shows the limits for the b-tagged and b-vetoed category separately. The expected and observed exclusion limits at 95% CL_s confidence level are shown as dashed and solid black lines, respectively. The green and yellow bands correspond to the 1σ and 2σ error bands on the expected exclusion limit. No significant excess over the expected SM background prediction is observed, $\tan\beta \geq 10$ in the mass range $90 < m_A < 200$ GeV is excluded with 95% CL_s confidence level. The most significant excess of events with a local p-value of 2.9% for the background only hypotesis is observed in the mass rage $250 < m_A < 300$ GeV, corresponding to a signal significance of $1.9\,\sigma$ after the

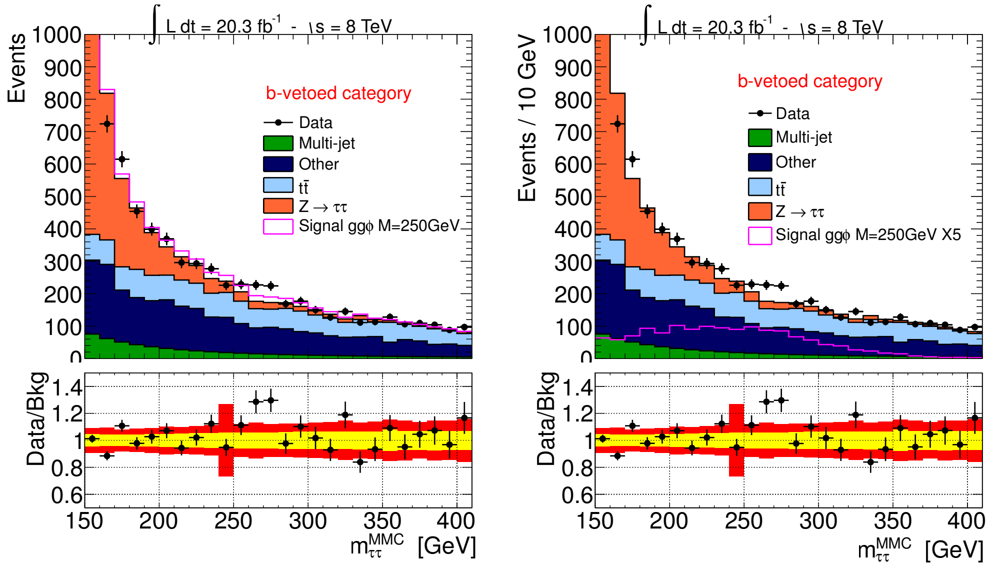

Figure 5.20.: Observed and expected distribution of the $m_{\tau\tau}^{MMC}$ in the mass range $150 < m_{\tau\tau}^{MMC} < 400$ GeV. A scalar boson with mass of 250 GeV produced via gluon fusion is assumed and superimposed to the background prediction (left) or scaled by a factor five to better appreciate the mass resolution (right). The production cross section considered is the one excluded by the observed limits for this mass (see text).

look elsewhere effect is considered. This small excess is driven by a fluctuation of the data in the b-vetoed category as can be seen from Figure 5.16. The excess is not confirmed by the other search channels. An attempt to interpret the excess as a scalar boson with a mass of 250 GeV is shown in Figure 5.20. The signal is assumed to be produced via gluon fusion and its cross section is scaled to the observed upper limit for this mass. Further cross checks on this excess of events can be found in Appendix C.

The outcome of the search is also interpreted in a model-independent way, by setting limits on the cross-section times branching ration into τ pairs of a scalar boson produced via gluon fusion, $pp \to gg \to \phi$, or in association with b-quarks $pp \to b\bar{b}\phi$. The corresponding expected and observed 95% CL_s confidence level limits are shown in Figure 5.22. Exclusion limits for additional benchmark scenario like m_h^{max}, tau-phobic and light-stop scenarios are shown in Appendix B. More information on the limit setting procedure and its validation can be found in Appendix C.

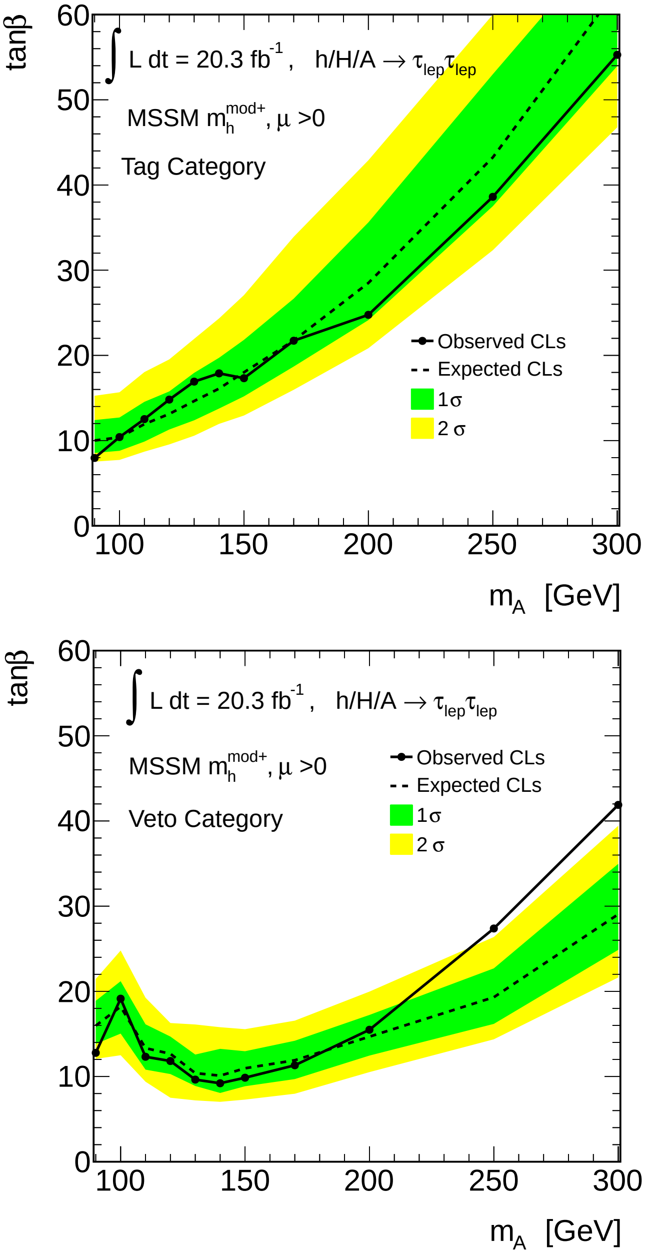

Figure 5.21.: Expected and observed exclusion limits at the 95% CL_s confidence-level for MSSM Higgs bosons production interpreted in the $m_A - \tan\beta$ parameter space of the m_h^{mod} scenario in the b-tagged (top) and b-vetoed (bottom) category.

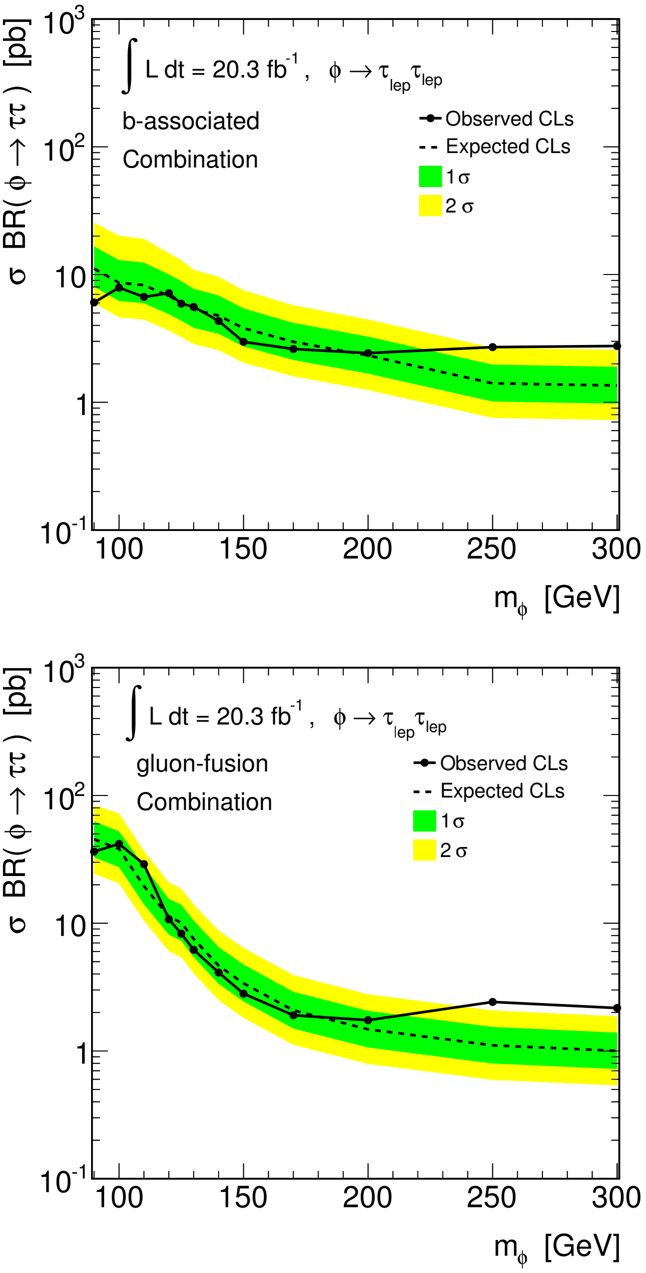

Figure 5.22.: Expected (dashed line) and observed (solid line with markers) 95% CL_s confidence level upper limits on the production cross section via gluon fusion (top) and in association with b quarks (bottom) for a scalar boson decaying into τ lepton pair. The b-tagged and b-vetoed category are combined.

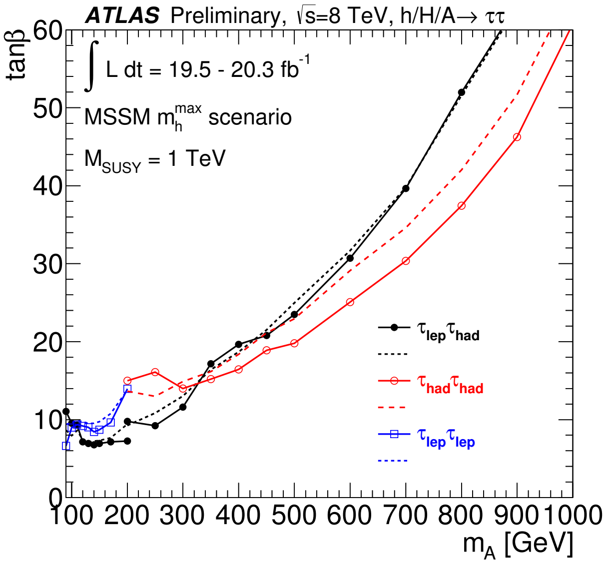

Figure 5.23.: Expected (dashed line) and observed (solid line with markers) 95% CL_s confidence level upper limits on $\tan\beta$ as a function of m_A for the different search channels shown separately [61].

5.5.4. Combination with Other Search Channels

The results of the presented search are combined with the search for neutral MSSM Higgs bosons in the semi-leptonic and fully hadronic $\tau\tau$ decay channels, which are characterised by the presence of one and two hadronically decaying τ leptons in the final state, respectively. The search for the semi-leptonic decays $(\tau_h\tau_\ell)$ has a high sensitivity to the signal for a large mass range and is split into two categories defined by the mass of the Higgs boson candidate: a low-mass category optimised for $90 < m_\phi < 200$ GeV and a high-mass category for $200 < m_\phi < 1000$ GeV. The $\tau_h\tau_\ell$ channel is combined with the $\tau_\ell\tau_\ell$ in the low-mass category while the high-mass category $\tau_h\tau_\ell$ is combined with the $\tau_h\tau_h$ channel. There is no simultaneous combination of the three search channels over the full mass range since it is demonstrated to give no further improvement of the signal sensitivity. A comparison between the expected and observed limits obtained with the different search channels is shown in Figure 5.23 in the m_h^{max} scenario. Figure 5.24 shows the upper limit in the m_h^{mod} scenario for the combination of all three search channel, the vertical dashed line at 200 GeV indicates the transition point between low and

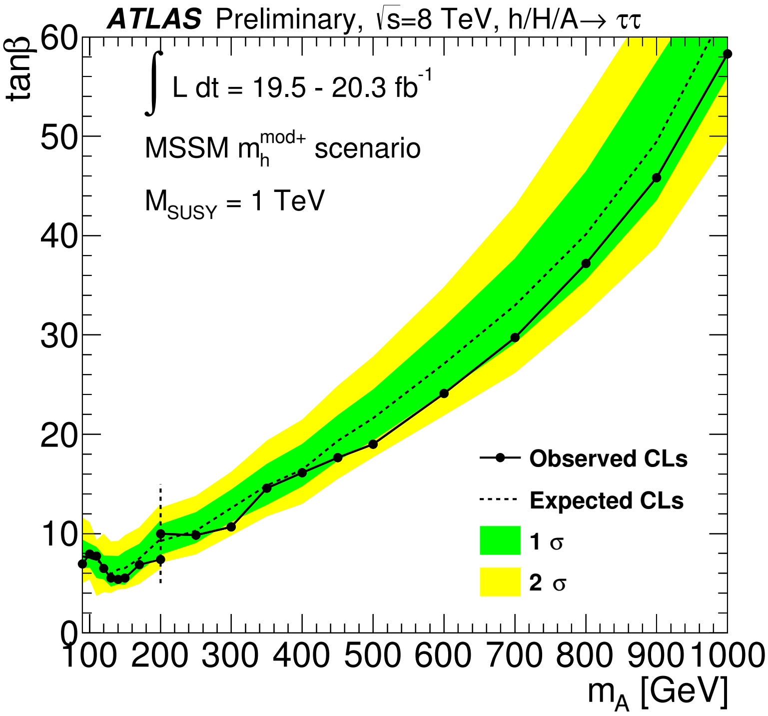

Figure 5.24.: Expected (dashed line) and observed (solid line with markers) 95% CL_s confidence level upper limits on $\tan\beta$ as a function of m_A for the m_h^{mod} benchmark scenario. Combination of all three search channel [61].

high mass categories. The outcome of the search is also interpreted in a model-independent way by setting limits on the cross-section times branching ration into τ pairs of a scalar boson produced via gluon fusion or in association with b-quarks, the combined upper limits are shown in Figure 5.25. A comparison with the corresponding CMS result [73] is shown in Figure 5.26 for the m_h^{max} benchmark scenario, ATLAS currently provide the world best limit for the neutral MSSM Higgs boson search for $m_A > 600$ GeV. Exclusion limits obtained for other benchmark scenarios can be found in Appendix B.

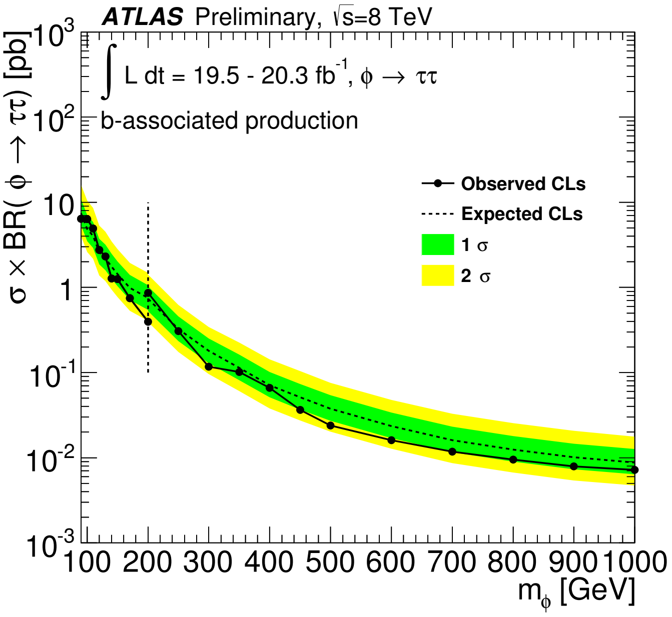

(a) $pp \rightarrow b(b)\phi$

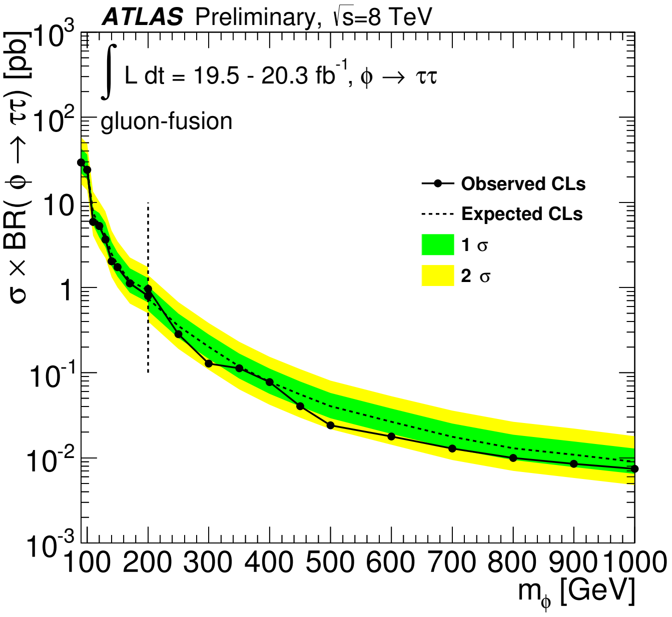

(b) $gg \rightarrow \phi$

Figure 5.25.: Expected (dashed line) and observed (solid line with markers) 95% confidence level upper limits on the cross section for the production of a scalar boson via (b) $pp \rightarrow b(b)\phi$ and (c) $gg \rightarrow \phi$ decaying into a τ lepton pair. The upper limits are shown for the combination of all channels [61].

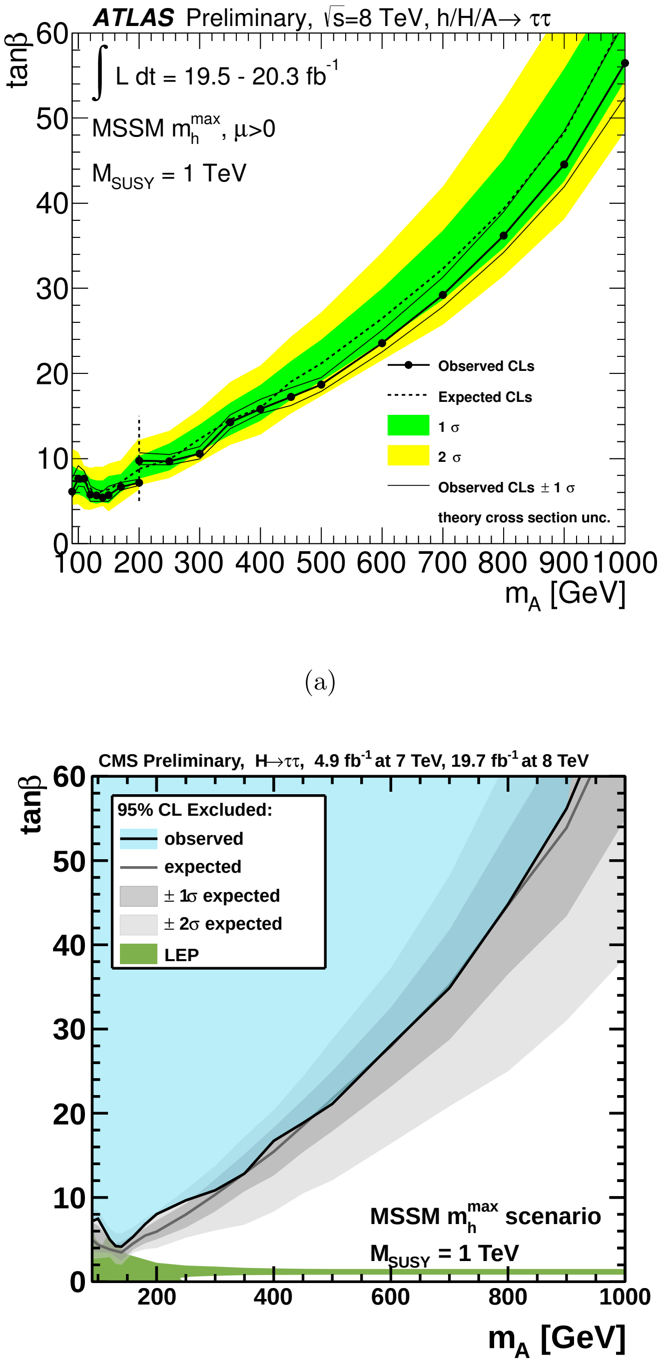

(a)

(b)

Figure 5.26.: Comparison of expected and observed limits on the $m_A - \tan\beta$ plane in the m_h^{max} scenario from the search for the neutral MSSM Higgs boson performed at (a) ATLAS [61] and (b) CMS [73] experiments.

6. Improvements to the MSSM Higgs Boson Search Using Track-Jets

The search for the neutral MSSM Higgs bosons described in the previous chapter suffers from relatively poor b-tagging performance due to the relatively low energies of the b-jets produced in association with the Higgs bosons. Improvements to the b-tagging performance would result in a major improvement of the signal sensitivity. In this chapter an alternative b-jet identification procedure is studied where the b-tagging algorithm is applied to track-based jets instead of the commonly used calorimeter jets. While the calorimeter jets are reconstructed from the energy clusters in the calorimeter, the track-based jets consist of inner detector tracks. The performance of the b-tagging for track-based jets have been investigated here for the first time. The prospects for improvements to the neutral MSSM Higgs boson search by applying b-tagging to track-based jets are discussed.

In Section 6.1 the challenges in the b-tagging for the MSSM Higgs boson search are explained together with a description of the track-based jet reconstruction. In Section 6.2 the performance of the b-tagging algorithms to track-based jets is described in comparison with the b-tagging performance for calorimeter jets. Preliminary evaluation of the impact on the analysis presented in this thesis is discussed. In Section 6.3 systematic uncertainties related to track-based jets are discussed. Finally, the conclusion of the studies on track-based jets are summarised in Section 6.4

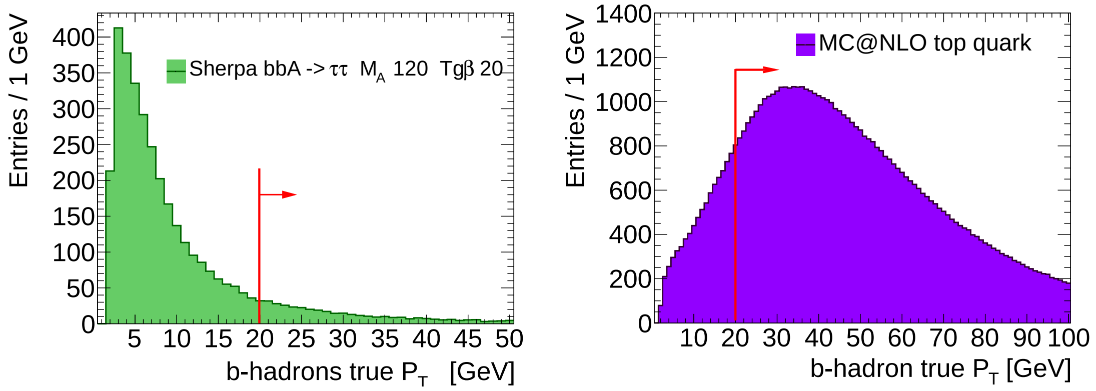

Figure 6.1.: Simulated p_T distribution of b-hadrons from b-quarks produced in association with the neutral MSSM Higgs boson (left) and from b-quarks jet in $t\bar{t}$ events (right). The red line indicates the region in which the energy of the calorimeter jets can be calibrated.

6.1. Track-Based Jets

In the search for the neutral MSSM Higgs bosons, as described in chapter 5, the selected events are categorised in two categories based on the presence or the absence of a b-tagged jet in the event. The b-tagged event category is optimised for the selection of Higgs bosons produced in association with b-quarks. Figure 6.1 shows a comparison between the p_T spectra of simulated b-hadron (hadrons containing a b-quark) in $pp \to b(b)\,A/h/H$ process and in $t\bar{t}$ events. The signal contains b-hadrons with relatively low transverse momenta, imposing a major challenge for the analysis of the b-tagged event category. Due to the high amount of pileup and ambient energy density in the events, the energy of the calorimeter jets with $p_T < 20$ GeV is not calibrated (see chapter 4), the jet reconstruction performance and related systematic uncertainties are not evaluated for these jets. The reconstruction of calorimeter jets in the $pp \to b(b)\,A/h/H$ signal production process is therefore not optimal and represent the major source of the sensitivity losses in the b-tagged event category. An additional challenge of the presented search is the worsening of the b-tagging performance for jets with low transverse momenta. The efficiency obtained with the $MV1$ tagger decreases rapidly with jet p_T, reaching a minimum of 50% at 20 GeV for the tagging point with $\epsilon_b^{t\bar{t}} = 70\%$ [122, 123].

The performance of the jet reconstruction for low transverse momenta may be improved by introducing *track-based* jets (in the following track-jets) in replacement to the commonly used calorimeter jets. Track-jets are reconstructed with the anti-kt algorithm by clustering inner detector tracks. Conversely to calorimeter clusters, tracks have associated impact parameter informations and track-jets can be reconstructed with tracks originating from the same interaction point, making their reconstruction very robust against the impact of pile-up.

Track-jets are built by the *TrackZTool* reconstruction software which runs the anti-kt clustering algorithm on a subset of user-defined tracks. For the purposes of this thesis track-jets are reconstructed from tracks satisfying the following quality selection criteria:

- The track should be associated to the primary vertex (PV), $|z_{track} - z_{PV}| < 2$ mm, where z_{track} and z_{PV} are the absolute z coordinate of the track and of the primary vertex, respectively.
- The track is required to point to the PV in the plane containing the beam axis by $|z_{PV} \cdot sin(\theta)| < 1.5$ mm, where θ is the angle between the track and the beam axis.
- The distance of minimum approach of the track to the primary vertex in the plane orthogonal to the beam axis is required to be $d_{PV} < 1.5$ mm.
- At least one pixel hit and at least 6 SCT hits (including SCT holes) should be detected for each track.
- A b-layer hit should be present if the b-layer module passed by the track was active.
- The pseudorapidity of the track is required to be $|\eta| < 2.5$, corresponding to the coverage of the inner detector.
- The track transverse momentum should be $p_T > 300$ MeV to ensure a low track fake rate.

A track-jet is seeded by a cluster of at least two tracks which satisfy the above selection criteria, the sum of the transverse momenta of all associated tracks is required to be $\sum_i p_{T,i} > 2$ GeV. It has been shown that the above selection criteria, together with a maximum cone size for clustering of $\Delta R = 0.6$, give the best compromise between the power of rejecting fake tracks and the b-hadron reconstruction efficiency. Several simulation samples have been produced to study

Table 6.1.: Monte Carlo simulation samples.

Process	MC Generator	Purpose
Minimum bias	Pythia	Systematics study
$b\bar{b}$	Alpgen	Performance for low p_T b-tagging
$Z/\gamma^* \to \tau\tau$	Pythia	Impact on the MSSM Higgs search
$t\bar{t}$	MC@NLO	Impact on the MSSM Higgs search
MSSM $bb/A/h/H$	Sherpa	Impact on the MSSM Higgs search

the performance of the track-jets reconstruction and of the b-tagging procedure applied to these jets. Table 6.1 gives a list of the produced samples along with the type of studied performed with them.

B-tagging has never been tested before on track-jets, in section 6.2 the first study of b-tagging over track-jets performances is reported.

6.2. Performance of the Track-based Jets Reconstruction and b-tagging

6.2.1. Track-based Jets Reconstruction

Many analysis could profit from an enhanced b-jet reconstruction efficiency at low values of p_T. The studies presented in this section are aimed at comparing the performance of the b-jet reconstruction efficiency and the common b-tagging algorithm for the calorimeter and track-based jets, focusing in particular on jets with low transverse momenta.

Even tough the track-jets are more robust against pile-up effects, which is the main reason for not use calorimeter jet at low transverse momenta, they contain only the charged fraction of the jet, while the neutral jet component is lost. According to isospin invariance the expected charged fraction in a jet amounts to roughly 2/3 of the total energy. The track-jet momentum is therefore shifted accordingly and there is a larger uncertainty on its measured direction. Figure 6.2 shows the distribution of transverse momentum residual $p_{T\,true} - p_{T\,jet}$ relative to the truth value $p_{T\,true}$ from *truth-jet* (see chapter 4) separately for calorimeter and

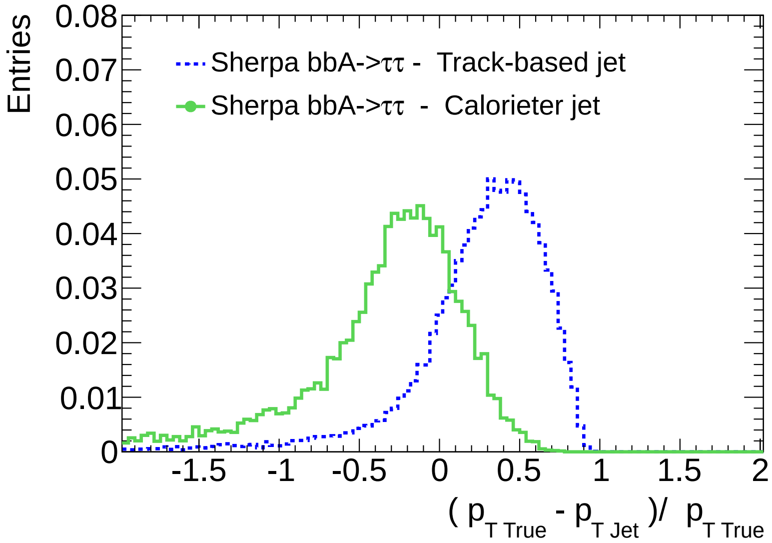

Figure 6.2.: Distribution of transverse momentum residuals relative to the true value $P_{T\,true}$, shown separately for the calorimeter and track-jets.

track-jets. Here truth-jets are matched with reconstructed jets within a cone of size $\Delta R = 0.4$[1]. As expected the track-jets energy is shifted from zero. This effect can be critical for most of the b-tagging algorithms since the likelihood functions used for decision making are derived separately for different region of jets p_T and pseudorapidity. A dedicated track-jets calibration of b-tagging algorithm is desirable for future application of b-tagging on these jets.

To compare the performance of calorimeter and track-jet reconstruction, an anti-kt algorithm with cone size of $\Delta R = 0.4$ is chosen. If the angular distance between the reconstructed jets and a simulated b-hadron in the event is $\Delta R < 0.3$, this jet is said to *match* with a b-hadron. b-hadron *Reconstruction efficiency* is then defined as the ratio between the number of matched b-hadrons and the total number of b-hadrons within inner detector acceptance. Figure 6.3 shows the b-hadron reconstruction efficiency for the calorimeter and track-jets. The latter exhibit a higher reconstruction efficiency at low transverse momenta due to their robustness against pile-up effects.

---

[1] jet splitting effects are resolved by matching with the nearest jet

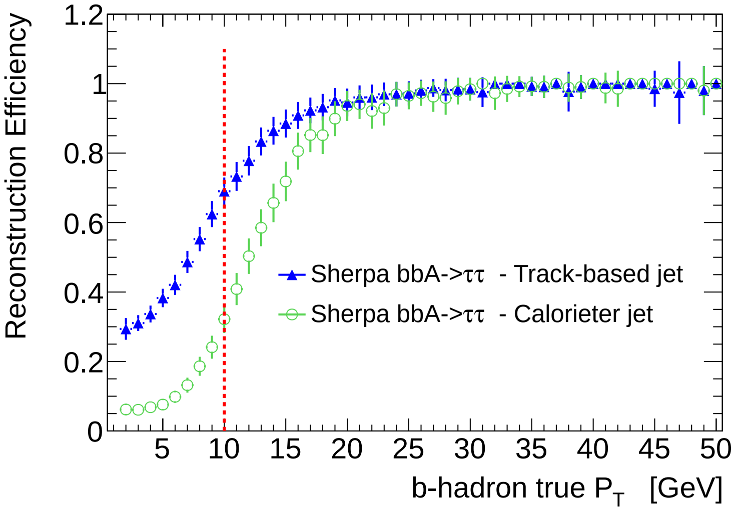

Figure 6.3.: b-hadron reconstruction efficiency for track-jet and calorimeter jets as a function of the true b-hadron p_T. Note that calorimeter and track-based jet are required to have at reconstruction level $p_T > 7$ and 2 GeV, respectively. A fair comparison in this plot is only possible for $p_T > 10$ GeV.

6.2.2. B-tagging with Track-Based Jets

Performance of the b-tagging algorithms is usually described in terms of the b-tagging efficiency and rejection power against misidentified jets. The *b-tagging efficiency* is the fraction of jets matched to a true b-hadron which pass a given tagging selection criteria, i.e. which are *b-tagged*. The *rejection power* is the inverse of the misidentification rate, i.e. the inverse of the fraction of jets which are not matched with a b-hadron or c-hadron, but are b-tagged. Figure 6.4 shows the rejection power as a function of the b-tagging efficiency for various b-tagging algorithms applied on track-jets and calorimeter jets separately. Figure 6.5 shows the rejection power as a function of jet p_T for the b-tagging working point which gives 50% b-tagging efficiency, calorimeter and track-based jet are shown separately. Mis-tagging rate is rapidly increasing for low transverse momentum jets due to increasing particle multiple scattering and secondary interactions in the material, revealing the necessity of a dedicated b-tagging algorithm for low p_T jets.

The described rejection power and b-tagging efficiency cannot serve for a fair comparison of the track-based and calorimeter jets. The latter can be reconstructed even if there are no associated tracks to them, in which case any b-tagging al-

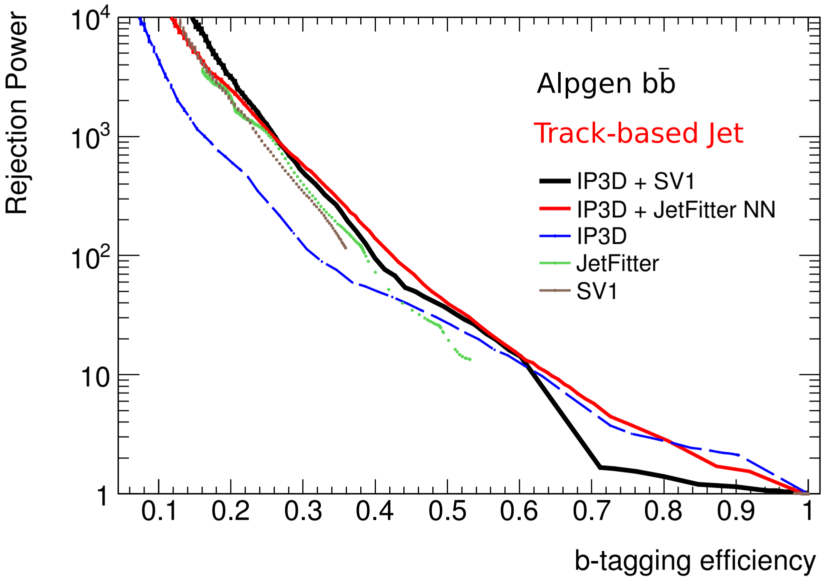

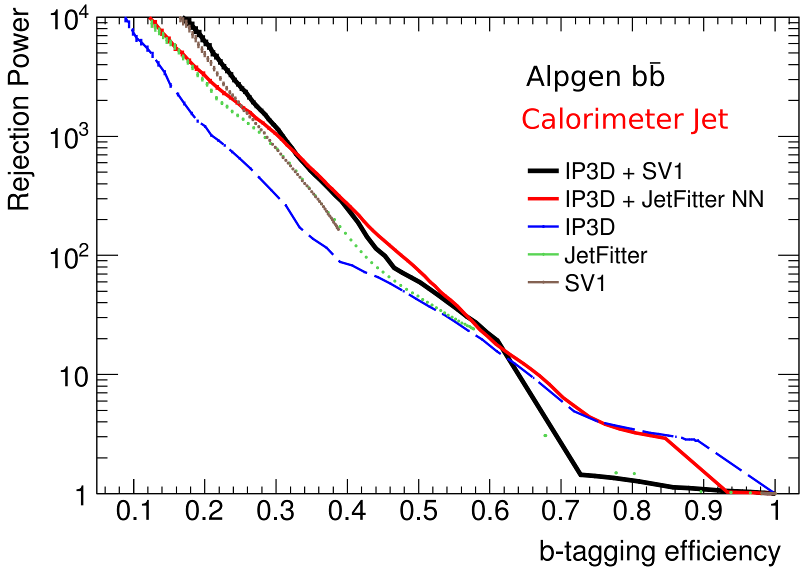

Figure 6.4.: Rejection power as a function of the b-tagging efficiency for different b-tagging algorithm applied on track-jets (top) and on calorimeter jet (bottom) for simulated $b\bar{b}$ events.

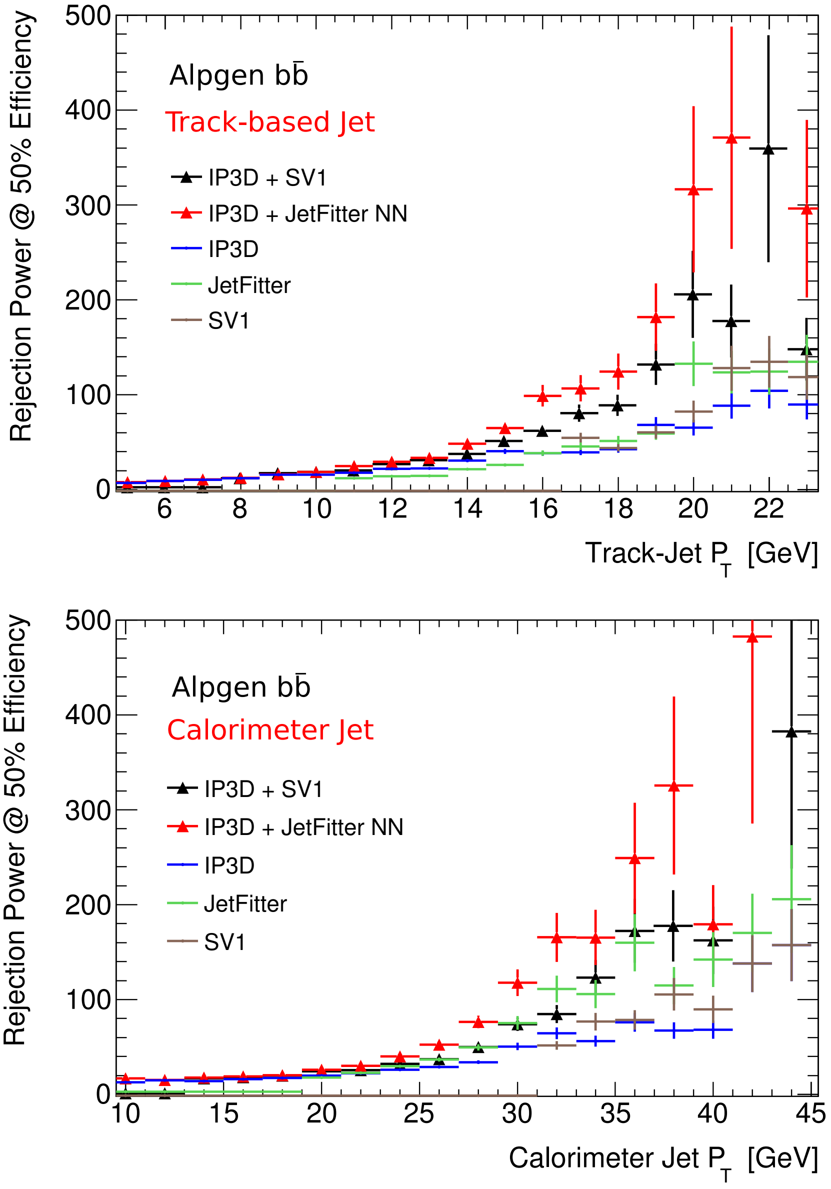

Figure 6.5.: Rejection power as a function of the jet transverse momentum for the b-tagging working point whit a 50% b-tagging efficiency at that p_T value, track-jet (top) and calorimeter jet (bottom) are shown separately. Results are obtained using simulated $b\bar{b}$ events and shown for several b-tagging algorithms.

gorithm will most likely fail. The distribution of the rejection power is therefore altered by such jets. It is instead convenient to introduce the: *effective rejection power*, which is the inverse of the number of mis-tagged jets per event. Figure 6.6 shows the effective rejection power as a function of the b-hadron reconstruction efficiency, for calorimeter and track-based jets. For a given b-hadron reconstruction efficiency, a higher effective rejection of mis-tagged jets can be achieved by track-jets. For a fair comparison with calorimeter jets, the track-jets in Figure 6.6 are selected in the transverse momentum range between 4 and 33 GeV, while the transverse momentum of calorimeter jets ranges from 8 to 50 GeV. The introduced p_T-thresholds corresponds in average to the same p_T range, Figure 6.2 is only valid for low p_T jets and the fraction of undetected momentum from neutral jet component approaches 1/3 for higher p_T track-jets. In conclusion, for jets with low transverse momentum the track-jets provide a higher b-hadron reconstruction efficiency than calorimeter jets and are more suitable for low p_T b-tagging.

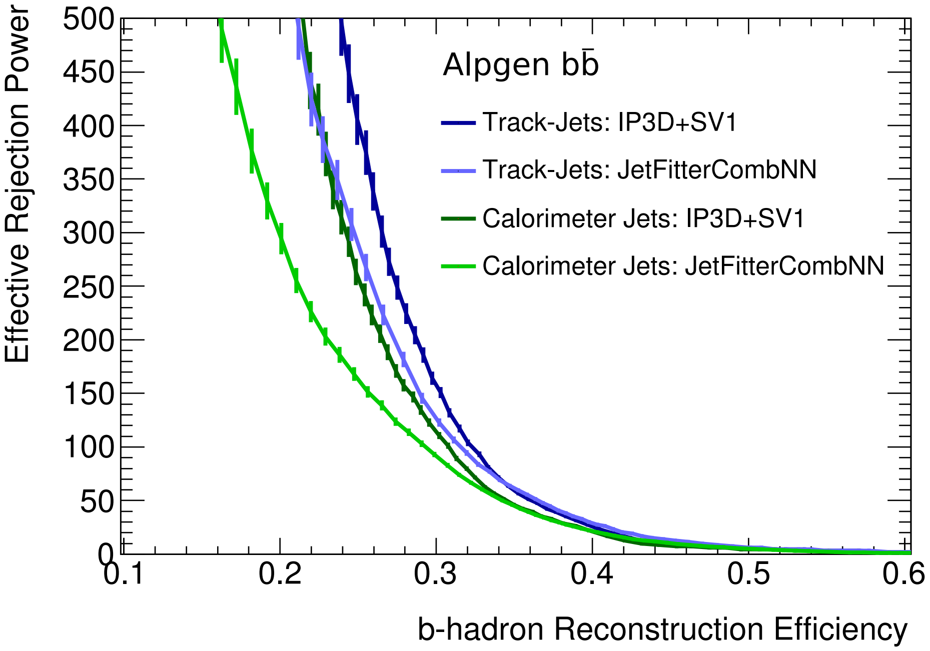

Figure 6.6.: Effective rejection as a function of b-hadron reconstruction efficiency, track-jet and calorimeter jets are compared for two different ATLAS tagging algorithms. Track-jets are selected in the transverse momentum range between 4 and 33 GeV, while calorimeter jets between 8 and 50 GeV.

6.2.3. Use of Track-jets for the MSSM Higgs Boson Search

The impact of the track-jets selection on the search for the neutral MSSM Higgs bosons is tested in a preliminary study and reported in the following. Common selection criteria,[2], as defined in in Section 5.2.1, are applied to simulated signal and background samples with the following modifications concerning the jets on which b-tagging procedure is applied (taggable jets):

- Calorimeter jets should have $|\eta| < 2.5$ and $20 < p_T < 50$ GeV.
- Track-jets should have $|\eta| < 2.5$ and $5 < p_T < 33$ GeV.
- The b-tagging algorithm applied on the above jets is "IP3D+SV1" at a working point with a $\epsilon_b^{t\bar{t}} = 70\%$ tagging efficiency.

The minimum transverse momentum for which calorimeter jet are calibrated is 20 GeV, track-jets instead can safely access transverse momentum up to 5 GeV. The event yields expected for the $pp \to b(b)A/h/H$ signal process, $Z/\gamma^* \to \tau\tau$ and $t\bar{t}$ background processes (the two most important background contributions in the b-tagged event category) are reported in Table 6.2. The yields are normalised to an integrated luminosity of 1 fb^{-1}. In addition to the event yields after the common selection stage other b-tagging related selection requirements are applied to study the impact of the replacement of calorimeter with track-based jets. As expected, after requiring exactly one b-tagged jet, the track-jets reconstruction results in a higher signal efficiency with a relatively similar rejection (10% higher) of top quark background compared to calorimeter-based jet reconstruction. However, lower transverse momentum threshold for the track-jets implies higher mis-tagging rates, as can be seen from an increase of $Z/\gamma^* \to \tau\tau$ background. This may also lead to a strong contamination of the QCD multi-jet background, even tough this is a minor background contribution in b-tagged event category.

In conclusion, the neutral MSSM Higgs boson search presented in the previous chapter may be improved if track-jet reconstruction is applied instead of calorime-

---

[2] This study has not been updated with the latest version of the object reconstruction selections and corrections, a difference of the order of 10% is expected with respect the numbers in table 5.4.

Table 6.2.: Event yield for the signal and dominant background processes after different event selection requirements. The yields are shown separately for the calorimeter and the track-based jet reconstruction. The Higgs boson produced in association with b-quarks is simulated for $\tan\beta = 20$ and $m_A = 150$ GeV. The yields are normalised to an integrated luminosity of 1 fb^{-1}.

Selection	Signal $bbA/H/h$		$Z/\gamma^* \to \tau\tau$		$t\bar{t}$	
Common Selection	127.2 ± 2.2		3017 ± 8		2066 ± 5	
	Calo. jet	Track-jet	Calo. jet	Track-jet	Calo. jet	Track-jet
At least one taggable jet	47.3 ± 0.8	106.9 ± 1.8	1146 ± 3	2513 ± 7	1804 ± 4	2014 ± 5
Exactly one jet matched to a b-hadron	18.4 ± 0.3	46.7 ± 0.8	4.5 ± 0.3	18.2 ± 0.5	1054 ± 3	959.1 ± 2.3
Exactly one b-tagged jet	10.2 ± 0.1	21.0 ± 0.6	37.3 ± 0.5	107 ± 1	777 ± 4	630 ± 4

ter based one. The sensitivity[3] to the signal can be improved in this event category by about a factor two. However, to exploit the full power of this technique a dedicated calibration of the b-tagging algorithms is needed for the track-jets. Additional improvements of the b-tagging algorithms for low p_T b-jets are also desirable. Furthermore, systematic uncertainties of track-jet reconstruction need to be evaluated. A preliminary study, addressing some of the most important of such systematic uncertainties is reported in section 6.3.

---

[3] Note that the sensitivity is estimate according to the $s/\sqrt{b}$ ratio (where s and b are the signal and background yield respectively), considering a counting experiment without systematic uncertainties and with only two background processes, this corresponds to the maximal possible sensitivity achievable with the current b-tagging performance.

6.3. Systematic Uncertainties of Track-Jet Reconstruction

There are several sources of systematic uncertainties of the track-jet reconstruction that may contribute to the mismodeling of physics observables. These effects are briefly summarised in the following with an emphasis on uncertainties of the energy scale and reconstruction efficiency.

Uncertainty on the properties of simulated track-jets can arise from the Monte Carlo generator configurations, depending on the particular choice of PDF and fragmentation functions, or details of the parton shower and underlying event modelling, which have a significant impact on physics objects with low transverse momentum. These uncertainties can be evaluated by means of a dedicated analysis with the Rivet package [135]. They depend on the particular use of track-jets and need to be evaluated case by case.

Energy scale and resolution of single tracks is found to be very well modelled by simulation for tracks above 500 MeV [146]. Thus, uncertainty on the track-jet energy scale and resolution that arise from the mismodeling of the pattern recognition procedure are considered to be negligible.

In a dense track environment different tracks may share same hits, leading to a degradation of the track momentum resolution, fake tracks and losses of track reconstruction efficiency. Mismodeling of the hit sharing among several tracks may in general affect the track-jet energy scale, resolution and reconstruction efficiency. Such effects has been studied in [148], where energy scale uncertainties for calorimeter jets is measured based on associated tracks. It has been shown that effects due to the merging of track hits are negligible for jets with $p_T < 300$ GeV.

Mismodeling of the inner detector material budget leads to the mismodeling of the to track reconstruction efficiency, which strongly affects also the track-jets reconstruction. A methodology to estimate the uncertainty of the energy scale and reconstruction efficiency for track-jets due to the mismodelling of the material budget is studied for the first time and presented in section 6.3.1.

6.3.1. Material Budget Uncertainty on Track-Based Jets Reconstruction

An obvious but rather inconvenient way to estimate the uncertainty due to the mismodeling of the inner detector material budget is to simulate the Monte Carlo samples relevant for a given analysis using several different ID material budgets. It can be shown that the mismodeling of material budget primarily influence the track reconstruction efficiency (see section 6.3.2). An alternative approach is therefore to modify the track reconstruction efficiency in a given sample according to the corresponding uncertainty [147, 149] and build track-jets from such new collection of tracks. A tool has been developed which randomly removes tracks according to the uncertainty on reconstruction efficiency. The track-jets which are build from this subset of tracks are called in the following *inefficient* track-jets.

The standard and inefficient track-jets are compared in a simulated sample of minimum bias processes. A set of "isolated" track-jet with cone size $\Delta R = 0.4$ are selected, where the isolation means that no other track-jet should be reconstructed within an angular distance of $\Delta R = 1$. Inefficient track-jets are then matched with the original track-jet in the same event, the matching fails if no inefficient track-jet is found within a cone of size $\Delta R = 0.8$ around the original track-jet. The impact of tracking inefficiency on track-jet energy scale and reconstruction efficiency is presented respectively in Figure 6.7 and 6.8 . These results are based on the current knowledge of the inner detector material budget [147]. Since track-jets are required to have at least two tracks at reconstruction level, if a track is lost that jet cannot be reconstructed any longer, therefore for track-jet with two tracks the only effect is a loss of reconstruction efficiency. For track-jets with low transverse momentum, uncertainty on the material budget translates into an energy scale shift of 2-4% and in a reduction of the mean number of tracks.

This method can only simulate excess of material (reduced track efficiency) but not a lack of material (increased track efficiency). However, for the latter case a similar, symmetric impact is expected.

6.3.2. Validation of the Track Subtraction Method

The method described in section 6.3.1 depends strongly on the assumption that hadronic secondary interactions within the inner detector material lead manly to

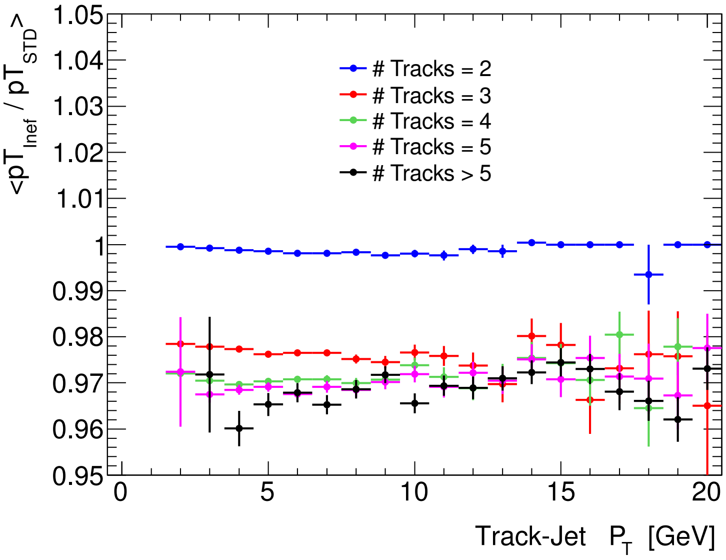

Figure 6.7.: Inefficient track-jets are matched with standard track-jets. The average transverse momenta of the inefficient track-jet $p_{T\,inef}$ relative to the corresponding standard track-jet $p_{T\,std}$ is shown as a function of the p_T and number of associated tracks of the standard track-jet.

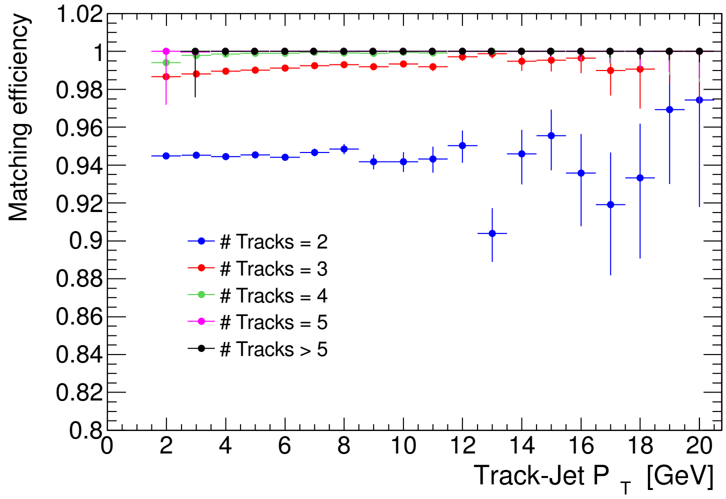

Figure 6.8.: Inefficient track-jets are matched with standard track-jets. The matching efficiency is shown as a function of the p_T and number of tracks associated with the standard track-jet.

the loss of some tracks and only in a marginal way to a decrease of the track quality. As a consequence, the mismodeling of the material budget is expected to influence mainly the track reconstruction efficiency. In this section, the impact of the material budget uncertainty on the track momentum resolution and fake rate is evaluated using a simulated sample of minimum bias events, in which additional material is added to the ID increasing uniformly of 10% the interaction length.

For this study, the track selection is performed as in Section 6.1. Furthermore a track should be matched within a cone $\Delta R < 0.1$ with a stable[4] simulated particle which alone should be causing at least 80% of all the track hits. Tracks that do not fulfil these requirements are considered as fake tracks. Fake tracks originate from a random combination of hits generated by different particles. The track fake rate defined as the ratio between the number of fake tracks and the total number of selected tracks is about 1-3% and is shown in Figure 6.9. The additional material leads to a total increase of the track fake rate by about one permille. The track energy resolution as shown in Figure 6.10 is about 1% for a large range of track p_T values, the total degradation of the resolution in the presence of additional ID material is also of the order about one permille. The deterioration of the track energy resolution and fake rate due to the additional material budget is therefore negligible compared to the impact on the track reconstruction efficiency of about 1-2%. Decrease in the track reconstruction efficiency has a strong impact on the track-jet energy scale. Figure 6.11 shows the ratio of the track reconstruction efficiency for the primary particles assuming the nominal and additional material budget.

Reconstruction of inefficient track-jets in a sample with nominal material budget is also directly compared to the track-jets reconstruction in a sample with added additional ID material. Track-jet are matched to truth-jet (as described in section 6.2) in order to determine the track-jet reconstruction efficiency and energy scale, shown respectively in Figure 6.12 and 6.13 . Inefficient track-jets reproduce correctly the impact of additional material, giving in most of the cases a conservative estimate of the corresponding systematic uncertainties.

---

[4] This refers to a generator level stable and interacting particle, i.e. a charged particle with decay length greater than 1m. Also stable particles from secondary interactions are considered.

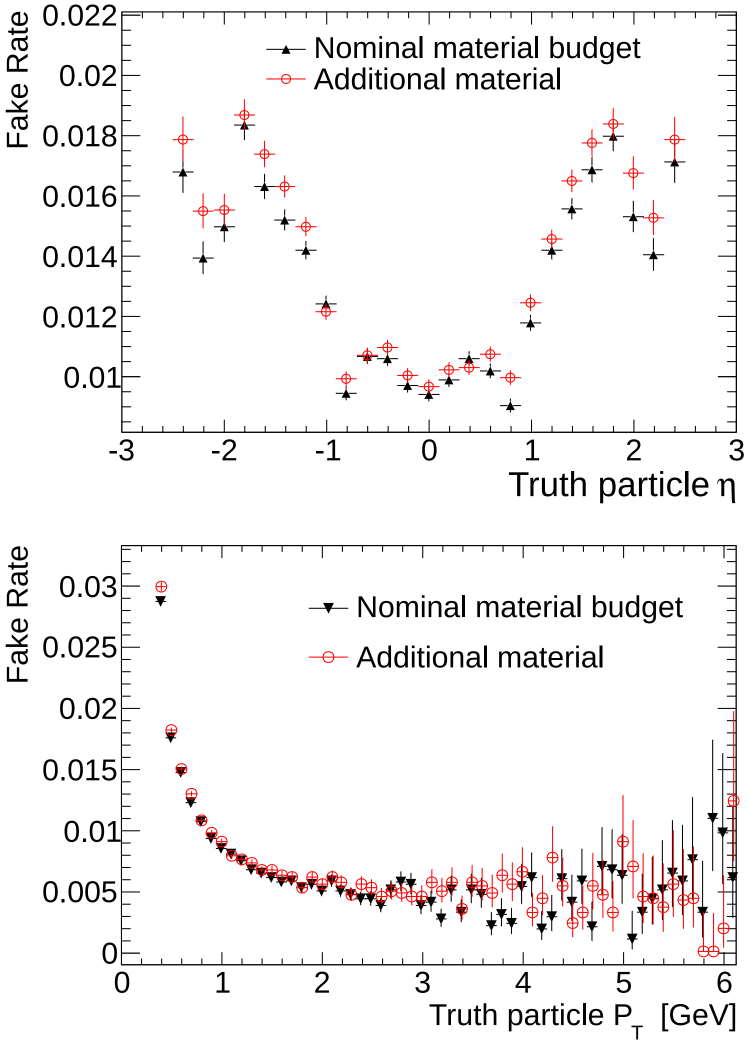

Figure 6.9.: Track fake rate as a function of the associated truth particle η (left) and p_T (right). The results are shown for the two simulated samples of of minimum bias processes, one with a nominal material budget and one with 10% additional inner detector material.

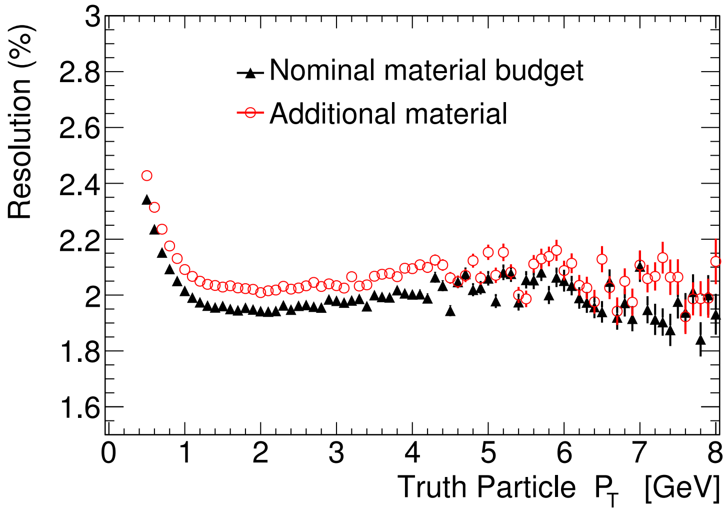

Figure 6.10.: Track momentum resolution relative to the matched truth particle as a function of truth particle p_T. The results are shown for the two simulated samples of of minimum bias processes, one with a nominal material budget and one with 10% additional inner detector material.

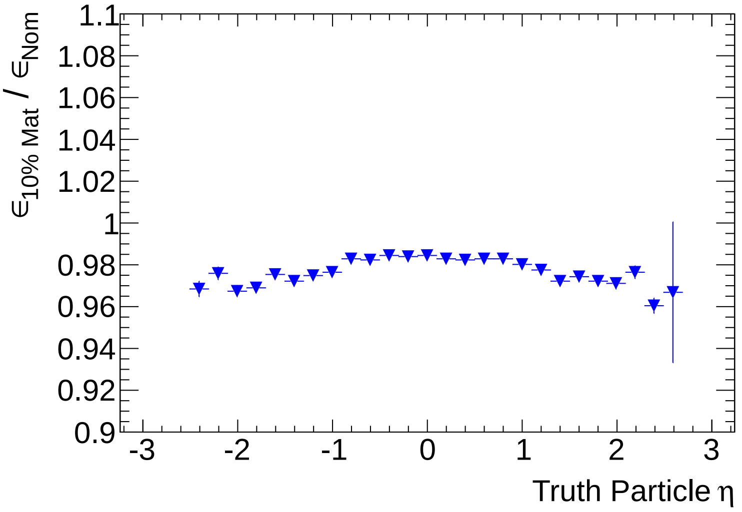

Figure 6.11.: Ratio of track reconstruction efficiencies relative to primary truth particles as a function of truth particle η. The ratio is shown for efficiency measured in minimum bias samples with the nominal material budget (ϵ_{Nom}) and in the sample with 10% of additional material ($\epsilon_{10\% Mat}$).

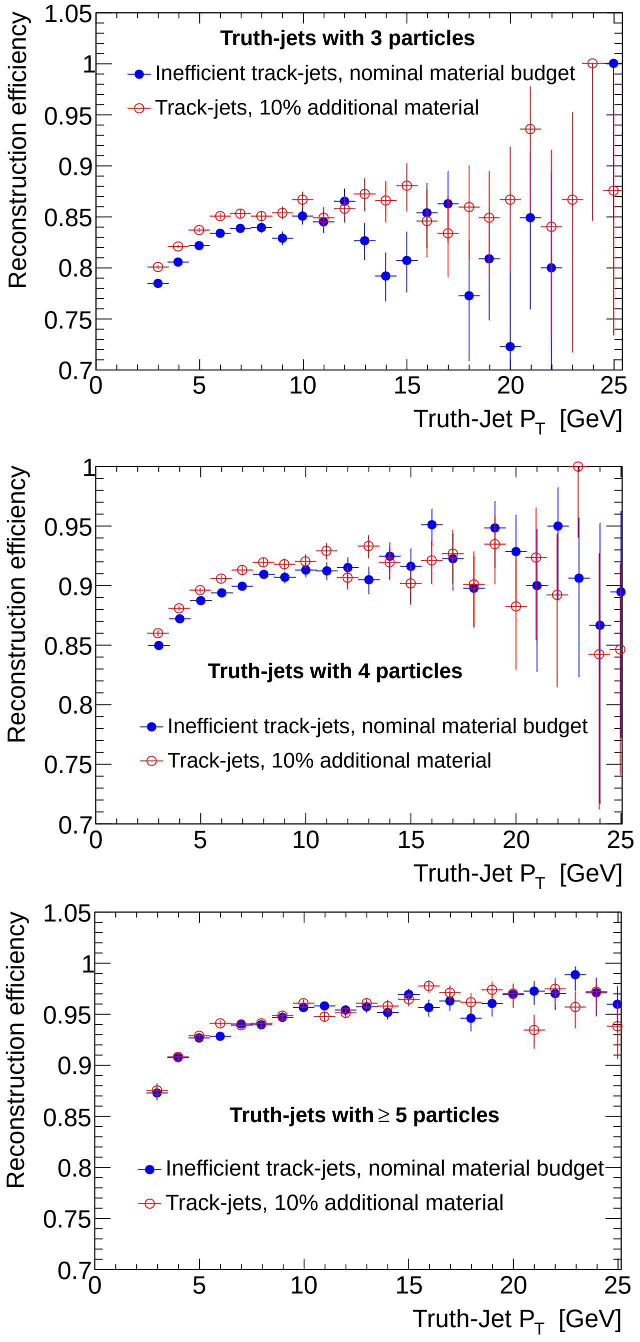

Figure 6.12.: Jet reconstruction efficiency relative to truth-jet for inefficient track-jets reconstructed in a minimum bias sample with nominal material budget and for the nominal track-jet reconstruction in a sample with 10% additional material. Result are shown separately for truth-jet consisting of 3,4 and ≥ 5 truth particle.

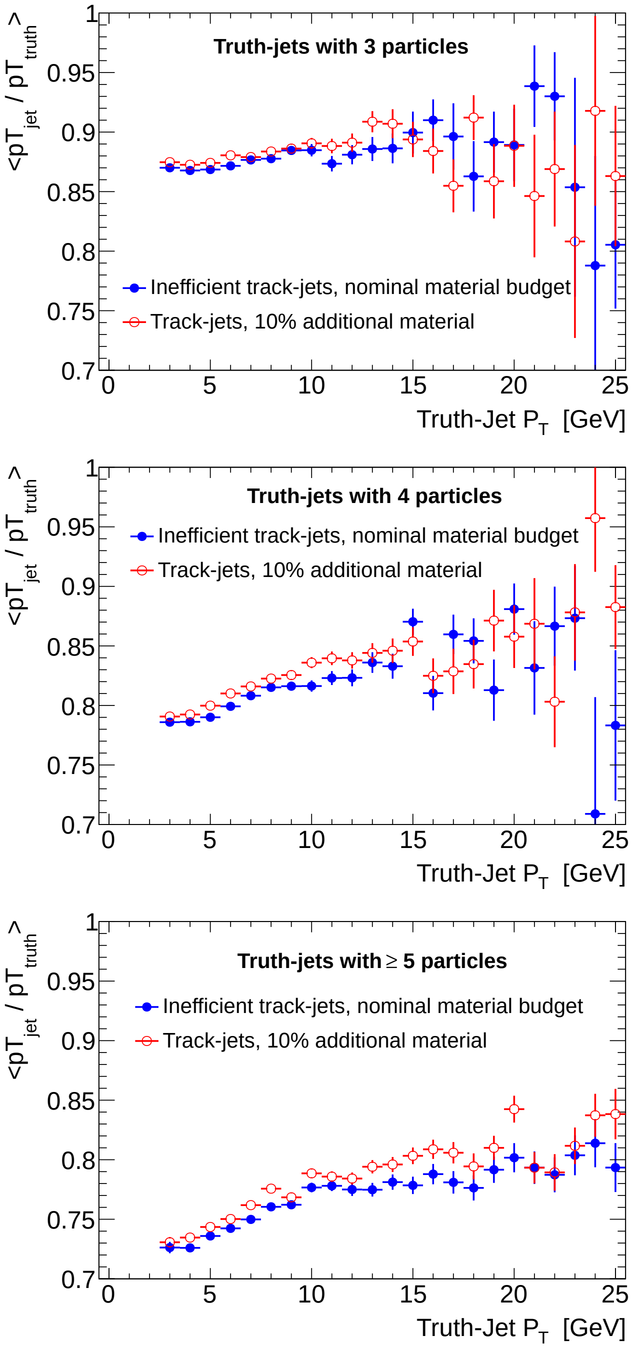

Figure 6.13.: Fraction of the jet transverse momentum relative to truth-jet transverse momentum shown for inefficient track-jets reconstructed in a minimum bias sample with nominal material budget and for the nominal track-jet reconstruction in a sample with 10% additional material. Result are shown separately for truth-jet consisting of 3,4 and ≥ 5 truth particle.

6.4. Conclusions

The performance of the b-tagging algorithms applied on track-based jets has been investigated for the first time in this thesis. One of the major systematic uncertainties arises from the incomplete description of the inner detector (ID) material budget in simulation. A novel technique for the determination of the systematic uncertainties in the track-based jets energy scale and reconstruction efficiency due to the ID material budget mismodelling has been developed. For track-jets with transverse momenta below 20 GeV, the uncertainty in the energy scale due to material budget mismodelling is estimated to range from 2% to 4% depending on the track-jet momentum and number of tracks in the jet.

It has been shown that for b-jets with transverse momenta below 20 GeV the track-based jet reconstruction provides a higher jet reconstruction efficiency than the calorimeter based one and is, therefore, more suitable for b-tagging of low p_T jets. The sensitivity of the search for the neutral MSSM Higgs bosons in associated production with b-quarks can be improved by up to a factor of two if track-jets are employed for b-tagging instead of calorimeter-based jets.

Although many questions about track-jet performance and related uncertainties have been already addressed in this thesis, there are still several open points to be studied in more detail in order to use b-tagging on track-jets into an analysis. Given the limited amount of time of a thesis and the considerable amount of resource needed for these studies, there are at lest two important issues that have not been addressed here and need to be studied in the future: a dedicated calibration of the b-tagging algorithms on track-based jets and an evaluation of the impact on their energy scale of systematic uncertainty related to Monte Carlo description of the underlying event, parton showering and fragmentation functions.

7. Summary and Conclusions

The Higgs boson recently discovered at the LHC with a mass of about 125 GeV shows properties which are well compatible with the predictions of the Standard Model (SM). Nevertheless, this new particle can also be accommodated within theories beyond the Standard Model. Among them, supersymmetric extensions of the SM are theoretically favoured since they offer an elegant way to solve many open questions in the SM. The minimal supersymmetric extension of the SM (MSSM) predicts the existence of five Higgs bosons, two of them neutral and CP-even (h and H), one neutral CP-odd (A) and two charged ($H^{\pm}$). Given the large number of free parameters of the MSSM, benchmark scenarios have been introduced in which most of the parameters are fixed leaving only two of them free which usually are chosen to be m_A and $\tan\beta$, the latter being the vacuum expectation value of the two MSSM Higgs doublets. The m_h^{mod} scenario where the observed boson is interpreted as the lightest MSSM CP-even Higgs boson h, while the other two MSSM Higgs bosons are degenerate in mass and decouple from gauge bosons, has acquired particular interest recently in view of the Higgs boson discovery. A large part of the $m_A - \tan\beta$ plane is still currently unexplored in this scenario, which is a strong motivation to pursue the search for additional neutral MSSM Higgs bosons.

In this thesis a search for the neutral MSSM Higgs bosons has been performed using proton-proton collision data recorded by the ATLAS experiment at the LHC in 2012 at a centre-of-mass energy of 8 TeV which corresponds to an integrated luminosity of $20.3\,\text{fb}^{-1}$. The search focuses on Higgs boson decays into pairs of τ leptons which subsequently decay via $\tau^+\tau^- \to e\mu + 4\nu$. The signal production processes considered are gluon fusion and the production in association with b-quarks. To enhance the signal sensitivity, the events are split into two mutually exclusive categories based on the presence or absence of b-tagged jets.

The main background contributions in this search are $Z/\gamma^* \to \tau\tau$, $t\bar{t}$ and diboson production and QCD multi-jet processes. The contribution of the dominant

$Z/\gamma^* \to \tau\tau$ background is measured using a dedicated signal-depleted control data sample in order to reduce the systematic uncertainties of the simulation. The QCD multi-jet background contribution is also estimated from a dedicated data control sample since these processes are difficult to model. All other background contributions are predicted by simulation. The background model is validated using several control data samples which are well described by the model. Systematic uncertainties in the simulation of signal and background processes from cross section calculations and the modelling of the detector response and in the background determined from data are taken into account.

The data are interpreted in the MSSM m_h^{mod} benchmark scenario as a function of m_A and $\tan\beta$ in the ranges $90 \leq m_A \leq 300$ GeV and $5 < \tan\beta < 60$, respectively. The measured $\tau\tau$ invariant mass distributions is compared to the predictions of the background-only and the signal-plus-background hypotheses. No significant excess above the estimated Standard Model background has been found. Exclusion limits are derived in the $m_A - \tan\beta$ plane in the m_h^{mod} benchmark scenario. Values of $\tan\beta \gtrsim 10$ are excluded in the mass range $90 < m_A < 200$ GeV. The most significant excess of events with a local p-value of 2.9% for the background only hypotesis is observed in the mass rage $250 < m_A < 300$ GeV, corresponding to a signal significance of $1.9\,\sigma$.

The results are also interpreted in other MSSM benchmark scenarios and in a less model-dependent way in terms of upper limits on the production cross section times branching fraction of a generic scalar boson ϕ with mass m_ϕ produced via the processes $pp \to b\bar{b}\phi$ and $gg \to \phi$. The results of this search are combined with the ones from searches in other $\tau\tau$ decay final states. The combined limits considerably constrain the allowed parameter space and represent the current best upper limit at high values of $m_A > 600$ GeV.

The search for the neutral MSSM Higgs bosons suffers strongly from the poor b-tagging performance for low-energy b-jets produced in association with the signal. This is due mainly to two effects: the reconstruction and calibration of jets from energy deposits in the calorimeters are strongly deteriorated by pile-up effects of multiple proton interactions per bunch crossing and in particular for low jet transverse momentum, furthermore the intrinsic b-tagging performance drops rapidly with the transverse momentum of the jet mainly due to mis-association of tracks to the jet, secondary interactions and multiple scattering. Improvements of the b-jet identification performance and jet reconstruction for low energies would result in a major improvement of the sensitivity of the search for Higgs boson produced in association with b-quarks. An alternative b-jet identification procedure in which the b-tagging algorithm is applied on track-based jets instead of the canonical calorimeter jets has been studied. The track-based jets consist of inner detector tracks. The high spatial track resolution allows for the association of the jet to its point of origin making the track-based jets considerably more robust against pile-up effects.

The performance of the b-tagging algorithms applied on track-based jets has been investigated for the first time in this thesis. One of the major systematic uncertainties arises from the incomplete description of the inner detector (ID) material budget in simulation. A novel technique for the determination of the systematic uncertainties in the track-based jets energy scale and reconstruction efficiency due to the ID material budget mismodelling has been developed. For track-jets with transverse momenta below 20 GeV, the uncertainty in the energy scale due to material budget mismodelling is estimated to range from 2% to 4% depending on the track-jet momentum and number of tracks in the jet.

It has been shown that for b-jets with transverse momenta below 20 GeV the track-based jet reconstruction provides a higher jet reconstruction efficiency than the calorimeter based one and is, therefore, more suitable for b-tagging of low p_T jets. The sensitivity of the search for the neutral MSSM Higgs bosons in associated production with b-quarks can be improved by up to a factor of two if track-jets are employed for b-tagging instead of calorimeter-based jets.

Although many questions about track-jet performance and related uncertainties have been already addressed in this thesis, there are still several open points to be studied in more detail in order to use b-tagging on track-jets into an analysis. Given the limited amount of time of a thesis and the considerable amount of resource needed for these studies, there are at lest two important issues that have not been addressed here and need to be studied in the future: a dedicated calibration of the b-tagging algorithms on track-based jets and an evaluation of the impact on their energy scale of systematic uncertainty related to Monte Carlo description of the underlying event, parton showering and fragmentation functions.

Acknowledgments

First of all I would like to thank Prof. Hubert Kroha and Dr. Sandra Kortner for the precious comment and help during editing this document and to gave me the extraordinary opportunity of being here. I would like to thank the Max Planck Institute and the organisers of IMPRS, with a special thank to Frank Steffen.

I would like to thank the members of the neutral MSSM Higgs boson search analysis team, in particular M. Backingham and N. Romptis, for being of such a great support during the last year.

I received an incredible amount of support from many persons. They made my stay in Munich, a journey, an adventure and have created an atmosphere that smells of home. It is to this big family that I want to address my most deep thanks. In order of appearance in this fairy tail that has been my life here. To my almost Russian roommate for being German enough for both of us and for his hard time with me. To Mr. bamboo Toyama with the wish he wont be too "heabi" with the little Ko. To Shangy for being... himself, hoping one day he will find his soul. To the Ogre for teaching me the difference between pig and pork and to Fiona for being a good spezi. To la Bruja Piruja, well, actually I don't know why she is in the list. To Sear-gay for the puzzling and oneiric discussions. But, most of all, I would like to thank the love of my life, the blond A. I hope any of you will manage one day to catch the duck is chasing.

Finally I would like to thank you, the reader, for being brave enough to arrive till this point of this document.

I'm very sorry if I accidentally forgot someone... but it is 5 am...

Bibliography

[1] The ATLAS Collaboration, *Observation of a new particle in the search for the Standard Model Higgs boson with the ATLAS detector at the LHC*, Physics Letters B 716 (2012) 1–29.

[2] The CMS Collatoration, S. Chatrchyan et al., *Observation of a new boson at a mass of 125 GeV with the CMS experiment at the LHC*, Physics Letters B 716 (2012) 30–61.

[3] The ATLAS Collaboration, G. Aad et al., *Evidence for the spin-0 nature of the Higgs boson using ATLAS data* , Phys. Lett. B 726 (2013), pp. 120-144.

[4] The ATLAS Collaboration, G. Aad et al., *Measurements of Higgs boson production and couplings in diboson final states with the ATLAS detector at the LHC*, Phys. Lett. B 726 (2013), pp. 88-119.

[5] The CMS Collaboration, S. Chatrchyan et al., *"Evidence for the direct decay of the 125 GeV Higgs boson to fermions,"* arXiv:1401.6527 [hep-ex].

[6] The CMS Collaboration, S. Chatrchyan et al., *Higgs boson width from on- vs. off-shell production and decay to Z-boson pairs* , arXiv:1405.3455.

[7] G. Altarelli, *Collider Physics within the Standard Model: a Primer,* arXiv:1303.2842, 2013.

[8] S. P. Martin, *A Supersymmetry primer,* In *Kane, G.L. (ed.): Perspectives on supersymmetry II* 1-153 hep-ph/9709356, 2011.

[9] A. Djouadi, *The Anatomy of Electroweak Symmetry Breaking Tome II: The Higgs Bosons in the Minimal Supersymmetric Model*, Phys. Rep. 459 (2008) 1.

[10] LHC Higgs Cross Section Working Group, S. Heinemeyer et al., *Handbook of LHC Higgs Cross Sections: 3. Higgs Properties*, arXiv:1307.1347 2013.

[11] LHC Higgs Cross Section Working Group, S. Dittmaier et al., *Handbook of LHC Higgs Cross Sections: 1. Inclusive Observables,* arXiv:1101.0593 2013.

[12] M. E. Peskin, D. V. Schroeder, *An Introduction To Quantum Field Theory*, Westview Press, 1995.

[13] S. L. Glashow, *Partial Symmetries of Weak Interactions*, Nuc. Phys. 22 (1961) 579.

[14] A. Salam, *Weak and Electromagnetic Interactions*, Conf. Proc. C 680519 (1968) 367. Originally printed in Svartholm: Elementary Particle Theory, proceedings of the Nobel Symposium held 1968 at Lerum, Sweden.

[15] S. Weinberg, *A Model of Leptons*, Phys. Rev. Lett. 19 (1967) 1264.

[16] H. Fritsch, M. Gell-Mann, and H. Leutwyler, *Advantages of the Color Octet Gluon Picture*, Phys. Lett. B 47 (1973) 365.

[17] F. Englert and R. Brout, *Broken Symmetry and the Mass of Gauge Vector Mesons*, Phys. Rev. Lett. 13 (1964) 321.

[18] P. W. Higgs, *Broken symmetries, massless particles and gauge fields*, Phys. Lett. 12 (1964) 132.

[19] P. W. Higgs, *Broken Symmetries and the Masses of Gauge Bosons*, Phys. Rev. Lett. 13 (1964) 508.

[20] P. W. Higgs, *Spontaneous Symmetry Breakdown without Massless Bosons*, Phys. Rev. 145 (1966) 1156.

[21] T. W. B. Kibble, *Symmetry Breaking in NonAbelian Gauge Theories*, Phys. Rev. 155 (1967) 1554.

[22] H. Yukawa, *On the Interaction of Elementary Particles*, PTP, 17, 48 (1935).

[23] W. Hollik, *Electroweak theory,* hep-ph/9602380, 1996.

[24] The Review of Particle Physics, J. Beringer et al. (Particle Data Group), Phys. Rev. D86, 010001 (2012) and 2013 partial update for the 2014 edition.

[25] The ALEPH, CDF, D0, DELPHI, L3, OPAL and SLD Collaborations, the LEP Electroweak Working Group, Tevatron Working Group and SLD Electroweak and Heavy Flavour Working Groups, *Precision Electroweak Measurements and Constraints on the Standard Model*, arXiv:1012.2367. Updated for 2012 winter conferences, March 2012.

[26] The Gfitter Group, M. Baak, et al., *Updated Status of the Global Electroweak Fit And constraints on New Physics*, Eur. Phys. J. C 72 (2012) 2003. Updated for 2012 winter conferences, March 2012, http://gfitter.desy.de.

[27] G.W. Bennett et al., Phys. Rev. Lett. 89, 101804 (2002); Erratum ibid. Phys. Rev. Lett. 89, 129903 (2002); G.W. Bennett et al., Phys. Rev. Lett. 92, 161802 (2004); G.W. Bennett et al., Phys. Rev. D73, 072003 (2006).

[28] B. Bhattacherjee, S. S. Biswal and D. Ghosh, *Top quark forward-backward asymmetry at Tevatron and its implications at the LHC*, Phys. Rev. D 83 (2011) 091501 arXiv:1102.0545 .

[29] M. Veltman, Acta. Phys. Pol. B8 (1977) 475.

[30] S. Weinberg, *Gauge Hierarchies*, Phys. Lett. B 82 (1979) 387.

[31] M. Veltman, *The InfraredUltraviolet Connection*, Acta Phys. Polon. B 12 (1981) 437.

[32] C. Smith and G. Ross, *The Real Gauge Hierarchy Problem*, Phys. Lett. B 105 (1981) 38.

[33] F. Zwicky, *Spectral Displacement of Extra Galactic Nebulae*, Helv. Phys. Acta 6 (1933) 110.

[34] E. W. Kolb and M. S. Turner, *The Early Universe*, Front. Phys. 69 (1990) 1.

[35] The WMAP Collaboration, D. N. Spergel et al., *First Year Wilkinson Microwave Anisotropy Probe (wmap) Observations: Determination of Cosmological Parameters*, Astrophys. J. Suppl. 148 (2003) 175.

[36] H. M. Georgi and S. L. Glashow, *Unity of All ElementaryParticle Forces*, Phys. Rev. Lett. 32 (1974) 438.

[37] J. C. Pati and A. Salam, *Lepton Number as the Fourth Color*, Phys. Rev. D 10 (1974) 275.

[38] P. Fayet, Phys. Lett. B 64, 159 (1976).

[39] P. Fayet, Phys. Lett. B 69, 489 (1977), Phys. Lett. B 84, 416 (1979).

[40] G.R. Farrar and P. Fayet, Phys. Lett. B 76, 575 (1978).

[41] S. Martin, *in Perspectives on Supersymmetry*, Ed. G.L. Kane, World Scientific, Singa- pore, 1998, hep-ph/9709356.

[42] P. Fayet and S. Ferrara, Phys. Rep. 32 (1977) 249; H.P. Nilles, Phys. Rep. 110 (1984) 1; R. Barbieri, Riv. Nuovo Cim. 11N4 (1988) 1; R. Arnowitt and P. Nath, Report CTP-TAMU-52-93; J. Bagger, Lectures at TASI-95, hep-ph/9604232.

[43] H. E. Haber and G. Kane, Phys. Rep. 117 (1985) 75.

[44] M. Drees and S. Martin, CLTP Report (1995) and hep-ph/9504324.

[45] D.J.H. Chung, L.L. Everett, G.L. Kane, S.F. King, J. Lykken and L.T. Wang, Phys. Rept. 407 (2005) 1.

[46] M. Drees, R.M. Godbole and P. Roy, *Theory and Phenomenology of Sparticles*, World Scientific, Spring 2004.

[47] L. Girardello and M.T. Grisaru, Nucl. Phys. B194 (1982) 65.

[48] Y. Okada, M. Yamaguchi and T. Yanagida, Prog. Theor. Phys. 85 (1991) 1;
ibid. Phys. Lett. B262 (1991) 54;
J.R. Ellis, G. Ridolfi and F. Zwirner, Phys. Lett. B257 (1991) 83;
ibid. Phys. Lett. B262 (1991) 477;
H.E. Haber and R. Hempfling, Phys. Rev. Lett. 66 (1991) 1815.

[49] A. Djouadi and S. RosiersLees (conv.) et al., *Summary Report of the MSSM Working Group for the "GDRSupersymetrie"*, hep-ph/9901246 (1999).

[50] K. Inoue, A. Komatsu and S. Takeshita, Prog. Theor. Phys 68 (1982) 927; (E) ibid. 70 (1983) 330.

[51] E. Witten, Nucl. Phys. B188 (1981) 513; ibid Nucl. Phys. B202 (1982) 253;
N. Sakai, Z. Phys. C11 (1981) 153;
S. Dimopoulos and H. Georgi, Nucl. Phys. B193 (1981) 150;
R.K. Kaul and P. Majumdar, Nucl. Phys. B199 (1982) 36.

[52] J.F. Donoghue and L.F. Li, Phys. Rev. 19 (1979) 945.

[53] J.F. Gunion and H.E. Haber, Nucl. Phys. B278 (1986) 449.

[54] J.F. Gunion and H.E. Haber, Nucl. Phys. B272 (1986) 1; (E) hep-ph/9301205.

[55] M. Frank et al., *The Higgs Boson Masses and Mixings of the Complex MSSM in the FeynmanDiagrammatic Approach*, JHEP 0702 (2007) 47.

[56] M. Carena, S. Heinemeyer, C. E. M. Wagner, and G. Weiglein, *Suggestions for benchmark scenarios for MSSM Higgs boson searches at hadron colliders*, Eur. Phys. J. C26 (2003) 601–607, `hep-ph/0202167`.

[57] S. Heinemeyer, O. Stal, and G. Weiglein, *Interpreting the LHC Higgs Search Results in the MSSM*, Phys. Lett. B 710 (2012) 201206, arXiv:1112.3026.

[58] The ATLAS Collaboration , *Constraints on New Phenomena via Higgs Boson Coupling Measurements with the ATLAS Detector.* ATLAS-CONF-2014-010.

[59] L. Maiani, A. Polosa, and V. Riquer, *Bounds to the Higgs Sector Masses in Minimal Supersymmetry from LHC Data*, arXiv:1305.2172 (2013).

[60] A. Djouadi, L. Maiani, G. Moreau, A. Polosa, J. Quevillon, et al., *The post-Higgs MSSM scenario: Habemus MSSM?*, arXiv:1307.5205 (2013).

[61] The ATLAS Collaboration, G. Aad et al., *Search for neutral Higgs bosons of the Minimal Supersymmetric Standard Model in pp collisions at sqrt(s)=8 TeV with the ATLAS detector*, ATLAS-CONF-2014-049 (2014).

[62] L. Evans and P. Bryant, *LHC Machine*, JINST 3 (2008) S08001.

[63] The ATLAS Collaboration, G. Aad et al., *The ATLAS Experiment at the CERN Large Hadron Collider*, JINST 3 (2008) S08003.

[64] J. Haffner, *The CERN accelerator complex*, OPEN-PHO-ACCEL-2013-056.

[65] CMS Collaboration, S. Chatrchyan et al., *CMS technical proposal*, CERN-LHCC-94-38 (1994).

[66] LHCb Collaboration, *LHCb technical proposal*, CERN-LHCC-98-004 (1998).

[67] ALICE Collaboration, *ALICE: Technical proposal for a large ion collider experiment at the CERN LHC*, CERN-LHCC-95-71, CERN, 1995,

[68] G. S. Guralnik, C.R. Hagen and T. W. B. Kibble, Phys.Rev.Lett. 13 (1964) 585.

[69] The ATLAS Collaboration, *Luminosity Determination in pp Collisions at* $\sqrt{s} = 7$ *TeV using the ATLAS Detector in 2011*, ATLAS-CONF-2011-116 (2011).

[70] The ATLAS Collaboration, *A Cherenkov Detector for Monitoring ATLAS Luminosity*, ATL-LUM-PROC-2010-004 (2010).

[71] ALEPH, DELPHI, L3 and OPAL Collaboration, *Search for neutral MSSM Higgs bosons at LEP*, Eur. Phys. J. C47 (2006) 547.

[72] CDF and D0 Collaboration, *Combined CDF and D0 upper limits on MSSM Higgs boson production in tau-tau final states with up to 2.2* fb^{-1} *of data*, `arXiv:1003.3363 [hep-ex]`.

[73] The CMS Collaboration, S. Chatrchyan et al., *Search for MSSM Neutral Higgs Bosons Decaying to Tau Pairs in pp Collisions*, CMS PAS HIG-13-021 (2013).

[74] The ATLAS Collaboration, G. Aad et al., *Search for the neutral Higgs bosons of the Minimal Supersymmetric Standard Model in pp collisions at* $\sqrt{s} = 7$ *TeV with the ATLAS detector*, arXiv:1211.6956 .

[75] M. L. Mangano et al., *ALPGEN, a generator for hard multiparton processes in hadronic collisions*, JHEP 07 (2003) 001.

[76] J. Alwall et al., *Comparative study of various algorithms for the merging of parton showers and matrix elements in hadronic collisions*, Eur. Phys. J. **C53** (2008) 473, `arXiv:0706.2569`.

[77] S. Frixione and B. R. Webber, *Matching NLO QCD computations and parton shower simulations*, JHEP **06** (2002) 029, `hep-ph/0204244`.

[78] B. P. Kersevan and E. Richter-Was, *The Monte Carlo Event Generator AcerMC 2.0 with Interfaces to PYTHIA 6.2 and HERWIG 6.5*, `arXiv:0405247v1 [hep-ph]`.

[79] G. Corcella et al., *HERWIG 6: an event generator for hadron emission reactions with interfering gluons (including supersymmetric processes)*, JHEP **01** (2001) 010.

[80] J. M. Butterworth, J. R. Forshaw, and M. H. Seymour, *Multiparton Interactions in Photoproduction at HERA*, Z. Phys. **C72** (1996) 637.

[81] T. Binoth, M. Ciccolini, N. Kauer, and M. Kramer, *Gluon-induced W-boson pair production at the LHC*, JHEP **12** (2006) 046.

[82] A. S. et al., *Higgs boson production in gluon fusion*, JHEP **02** (2009) 029.

[83] T. Gleisberg et al., *Event generation with SHERPA 1.1*, JHEP **02** (2009) 007.

[84] J. Pumplin, D. R. Stump, J. Huston, H. L. Lai, P. M. Nadolsky and W. K. Tung, "New generation of parton distributions with uncertainties from global QCD analysis," JHEP **0207** (2002) 012 [hep-ph/0201195].

[85] H. -L. Lai, M. Guzzi, J. Huston, Z. Li, P. M. Nadolsky, J. Pumplin and C. -P. Yuan, "New parton distributions for collider physics," Phys. Rev. D **82** (2010) 074024 [arXiv:1007.2241 [hep-ph]].

[86] The ATLAS Collaboration, G. Aad et al., *ATLAS Monte Carlo Tunes for MC09*, ATL-PHYS-PUB-2010-002.

[87] S. Jadach, J. H. Kuhn and Z. Was, *TAUOLA - a library of Monte Carlo programs to simulate decays of polarized τ leptons*, Comput. Phys. Commun. **64** (1990) 275.

[88] E. Barberio, B. V. Eijk and Z. Was, *Photos - a universal Monte Carlo for QED radiative corrections in decays*, Comput. Phys. Commun. **66** (1991) 115.

[89] The GEANT4 Collaboration, S. Agostinelli et al., *GEANT4 - a simulation toolkit*, Nucl. Instrum. Meth. **A506** (2003) 250.

[90] The ATLAS Collaboration, G. Aad et al., *The ATLAS Simulation Infrastructure*, ATLAS-SOFT-2010-01-004, submitted to Eur. Phys. J. C., `arXiv:1005.4568`.

[91] The ATLAS Collaboration, G. Aad et al., *Estimation of $Z/\gamma^* \rightarrow \tau\tau$ Background in VBF $H \rightarrow \tau\tau$ Searches from $Z \rightarrow \mu\mu$ Data using an Embedding Technique*, ATL-PHYS-INT-2009-109.

[92] The ATLAS Collaboration, G. Aad et al.,*Search for the Standard Model Higgs boson in the $H \rightarrow \tau\tau$ decay mode with 4.7 f b1 of ATLAS detector*, Tech. Rep. ATLAS-CONF-2012-014, CERN, Geneva, Mar, 2012.

[93] The ATLAS Collaboration, G. Aad et al.,*Search for the Standard Model Higgs boson $H \rightarrow \tau\tau$ decays with the ATLAS detector*, ATL-COM-PHYS-2013-722.

[94] T. S. et al., Z *physics at LEP 1*, CERN 89-08 **3** (1989) 143.

[95] The ATLAS Collaboration, G. Aad et al.,Inner Detector: Technical Design Report, CERN/LHCC/97-016/017 (1997).

[96] The ATLAS Collaboration, G. Aad et al., The ATLAS Experiment at the CERN Large Hardon Collider, 2008 JINST 3 S08003.

[97] A. Bazan, T. Bouedo, P. Ghez, M. Marino and C. Tull, "The Athena data dictionary and description language," eConf C **0303241** (2003) MOJT010 [cs/0305049 [cs-se]].

[98] The ATLAS Collaboration, G. Aad et al.,*Expected Performance of the ATLAS Experiment - Detector, Trigger and Physics*, CERN-OPEN-2008-020, `arXiv:0901.0512`.

[99] T. Cornelissen et al., Concepts, Design and Implementation of the ATLAS New Tracking, ATLAS Note ATL-SOFT-PUB-2007-007 (2007).

[100] Kalman, R. E. (1960). *"A New Approach to Linear Filtering and Prediction Problems"*. Journal of Basic Engineering 82 (1): 3545. doi:10.1115/1.3662552

[101] The ATLAS Collaboration, G. Aad et al.,Performance of primary vertex reconstruction in proton-proton collisions at $s = sqrt(7)$ TeV in the ATLAS experiment. ATLAS-CONF-2010-069.

[102] R. Fruhwirth, W. Waltenberger, P. Vanlaer, *Adaptive vertex fitting*, J. Phys. G34 (2007).

[103] The ATLAS Collaboration, G. Aad et al.,*Characterization of Interaction-Point Beam Parameters Using the pp Event-Vertex Distribution Reconstructed in the ATLAS Detector at the LHC*, ATL-CONF-2010-027.

[104] The ATLAS collaboration, G. Aad et al., *Expected electron performance in the ATLAS experiment*, ATL-PHYS-PUB-2011-006

[105] A. Hocker, P. Speckmayer, J. Stelzer, F. Tegenfeldt, and H. Voss, *TMVA, toolkit for multivariate data analysis with ROOT*, CERN-2008-001 .

[106] The ATLAS Collaboration, G. Aad et al., *Electron reconstruction and identification efficiency measurements with the ATLAS detector using the 2011 LHC proton-proton collision data*, CERN-PH-EP-2014-040, arXiv:1404.2240

[107] The ATLAS Collaboration, G. Aad et al., *Electron performance measurements with the ATLAS detector using the 2010 LHC proton-proton collision data*, Eur.Phys.J. C72 (2012) 1909.

[108] S. Hassini, et al., *A muon identification and combined reconstruction procedure for the ATLAS detector at the LHC using the (MUONBOY, STACO, MuTag) reconstruction packages*, NIM A572 (2007) 7779.

[109] The ATLAS Collaboration, G. Aad et al., *Preliminary results on the muon reconstruction efficiency, momentum resolution, and momentum scale in ATLAS 2012 pp collision data*, ATLAS-CONF-2013-088, CERN, 2013,

[110] M. Cacciari, G. P. Salam, and G. Soyez, *FastJet user manual*, Eur.Phys.J. C72 (2012) 1896.

[111] W. Lampl et al., *Calorimeter Clustering Algorithms : Description and Performance*, ATL-LARG-PUB-2008-002.

[112] M. Cacciari, G. P. Salam, and G. Soyez, *The anti-kt jet clustering algorithm*, JHEP 04 (2008) 63.

[113] E. Abat, J. Abdallah, T. Addy, P. Adragna, et al., *Combined performance studies for electrons at the 2004 ATLAS combined test-beam*, JINST 5 (2010) P11006.

[114] ATLAS Collaboration, G. Aad et al., *Jet energy measurement with the ATLAS detector in proton-proton collisions at* $\sqrt{s} = 7$ *TeV*, Submitted to EPJ (2011) , arXiv:1112.6426

[115] The ATLAS Collaboration, G. Aad et al., *Pile-up corrections for jets from proton-proton collisions at ATLAS in 2011*, ATLAS-CONF-2012-064, July, 2012.

[116] M. Cacciari and G. P. Salam, *Pileup subtraction using jet areas*, Phys.Lett. B659 (2008) 119.

[117] The ATLAS Collaboration, G. Aad et al., *Jet energy resolution in proton-proton collisions at* $\sqrt{s} = 7$ *TeV recorded in 2010 with the ATLAS detector*, Eur.Phys.J. C73 (2013) 2306

[118] The ATLAS collaboration, G. Aad et al., *Jet energy scale and its systematic uncertainty in proton-proton collisions at* $\sqrt{s} = 7$ *TeV with ATLAS 2011 data*, ATLAS-CONF-2013-004

[119] The ATLAS Collaboration, G. Aad et al., *Data-Quality Requirements and Event Cleaning for Jets and Missing Transverse Energy Reconstruction with the ATLAS Detector in Proton-Proton Collisions at a Center-of-Mass Energy of* $\sqrt{s} = 7$ *TeV*, ATLAS-CONF-2010-038.

[120] G. Piacquadio, C. Weiser, *A new inclusive secondary vertex algorithm for b-jet tagging in ATLAS*, JPCS 119 (2008) 032032

[121] The ATLAS Collaboration, G. Aad et al., *Commissioning of the ATLAS high-performance b-tagging algorithms in the 7 TeV collision data, ATLAS-CONF-2011-102*, CERN, 2011, ATLAS-CONF-2011-102.

[122] The ATLAS Collaboration, G. Aad et al., *Measuring the b-tag efficiency in a ttbar sample with 4.7* fb^{-1} *of data from the ATLAS detector* ATLAS-CONF-2012-097.

[123] The ATLAS Collaboration, G. Aad et al., *Calibration of b-tagging using dileptonic top pair events in a combinatorial likelihood approach with the ATLAS experiment* ATLAS-CONF-2014-004.

[124] The ATLAS Collaboration, G. Aad et al., *Reconstruction and Calibration of Missing Transverse Energy and Performance in* Z *and* W *events in ATLAS Proton-Proton Collisions at* $\sqrt{s}$*=7 TeV*, ATLAS-CONF-2011-080.

[125] ATLAS Collaboration, G. Aad et al., Performance of missing transverse momentum reconstruction in proton-proton collisions at 7 TeV with ATLAS, Eur.Phys.J. C72 (2012) 1844.

[126] The ATLAS Collaboration, G. Aad et al., *Performance of the Reconstruction and Identification of Hadronic tau Decays in ATLAS with 2011 Data*, ATLAS-CONF-2012-142.

[127] The ATLAS Collaboration, G. Aad et al., *Performance of the ATLAS trigger system in 2010*, Eur.Phys.J. C72 (2012) 1849.

[128] The ATLAS Collaboration, G. Aad et al., *Performance of the ATLAS muon trigger in 2011*, ATLAS-CONF-2012-099, CERN, 2012.

[129] The ATLAS Collaboration, G. Aad et al., *Performance of the ATLAS electron and photon trigger in p-p collisions at* $\sqrt{s} = 7$ *TeV in 2011*, ATLAS-CONF-2012-048, CERN, 2012.

[130] M. Dobbs and J.B. Hansen, *The HepMC C++ Monte Carlo Event Record for High Energy Physics*, Computer Physics Communications, ATL-SOFT-2000-001.

[131] A. Elagin, P. Murat, A. Pranko, and A. Safonov, *A New Mass Reconstruction Technique for Resonances Decaying to di-tau*, `arXiv:1012.4686 [hep-ex]`. * Temporary entry *.

[132] Atlas statistics forum, *ABCD method in searches*, link

[133] The Atlas Collaboration, *Measurement of the ttbar production cross-section in pp collisions at* $\sqrt{s} = 8$ *TeV using e-mu events with b-tagged jets* . ATLAS-CONF-2013-097.

[134] T. Sjostrand, S. Mrenna and P. Skands, *PYTHIA 6.4 physics and manual*, JHEP **05** (2006) 026.

[135] A. B. et al., *Rivet user manual*, `arXiv:1003.0694 [hep-ph]`.

[136] The ATLAS and CMS Collaborations, *Procedure for the LHC Higgs boson search combination in summer 2011*, ATL-PHYS-PUB-2011-011, ATL-COM-PHYS-2011-818, CMS-NOTE-2011-005.

[137] W. Verkerke and D. P. Kirkby, *The Roofit Toolkit for Data Modeling*, eConf C0303241 (2003) MOLT007, arXiv:physics/0306116

[138] K. S. Cranmer et al., *The Roostats Project*, PoS ACAT2010 (2010) 57.

[139] K. Cranmer, G. Lewis, L. Moneta, A. Shibata, and W. Verkerke, *Histfactory: A Tool for Creating Statistical Models for use with Roofit and Roostats*, CERNOPEN2012016 (2012)

[140] E. G. G. Cowan, K. Cranmer and O. Vitells, *Asymptotic formulae for likelihood-based tests of new physics*, `arXiv:1007.1727 [hep-ex]`.

[141] A. L. Read. *Presentation of search results: the CLs technique.* J. Phys. G: Nucl. Part. Phys., 28, 2002.

[142] A. L. Read. *Modified frequentist analysis of search results (the CLs method).* In Proceedings of the First Workshop on Confidence Limits, CERN, Geneva, Switzerland, 2000.

[143] E, Gross and O. Vitells. *Trial factors for the look elsewhere effect in high energy physics.* The European Physical Journal C - Particles and Fields, 70:525530, 2010.

[144] LHC Higgs Cross Section Working Group, S. Dittmaier, C. Mariotti, G. Passarino, R. Tanaka (Eds.), et al., *Handbook of LHC Higgs Cross Sections: 1. Inclusive Observables*, `arXiv:1101.0593 [hep-ph]`.

[145] LHC Higgs Cross Section Working Group, S. Dittmaier, C. Mariotti, G. Passarino, and R. Tanaka (Eds.), *Handbook of LHC Higgs Cross Sections: 2. Differential Distributions*, CERN-2012-002 (CERN, Geneva, 2012) , `arXiv:1201.3084 [hep-ph]`.

[146] ATLAS collaboration *Performance of the ATLAS Silicon Pattern Recognition Algorithm in Data and Simulation at* $\sqrt{s} = 7$ *TeV*, ATLAS-CONF-2010-072

[147] The ATLAS Collaboration, *A measurement of the material in the ATLAS inner detector using secondary hadronic interactions*, arXiv:1110.6191, JINST 7 (2012) P01013

[148] The ATLAS Collaboration, *Validation of the ATLAS jet energy scale uncertainties using tracks in proton-proton collision* $\sqrt{s} = 7$ *TeV*, ATLAS-CONF-2011-067

[149] The ATLAS Collaboration, *Track Reconstruction Efficiency in* $\sqrt{s} = 7$ *TeV Data for Tracks with* $p_T > 100$ *MeV* , ATL-PHYS-INT-2010-112

[150] D. de Florian, G. Ferrera, M. Grazzini and D. Tommasini, *Transverse-momentum resummation: Higgs boson production at the Tevatron and the LHC*, JHEP **1111** (2011) , `arXiv:1109.2109 [hep-ph]`.

[151] Statistical twiki, NuissanceCheck. https://twiki.cern.ch/twiki/bin/view/AtlasProtected/NuisanceCheck

A. Additional QCD Studies

A.1. Trigger Bias

The single electron trigger (`EF_e24vhi_medium1`) used in this analysis includes the following isolation cut: $p_T(\text{cone})20/p_T < 0.1$. This means that the kinematical distributions in the anti-isolated ABCD regions will biased due to a reduced efficiency for high p_T electrons. This unwanted feature may potentially effect the R_{QCD} factor, as the OS/SS ratio may differ due to different p_T spectrum. To check the effect on R_{QCD} the ABCD method has been repeated using the `EF_e24vh_medium1` trigger, which doesn't include isolation and hence is prescaled in 2012 8 TeV data. The prescale of a factor around 100 has been taken in consideration using trigger information stored in D3PD. Figure A.1 shows $p_T(\text{cone})$ distribution for the standard and test triggers. The comparable event yields in the region $p_T(\text{cone})20/p_T < 0.1$ show that the prescale normalisation for the test trigger has been correctly accounted for.

Figure A.2 shows the behaviour of R_{QCD} factor as a function of isolation variable for the two triggers under test. As the deviations are within statistical uncertainty, we conclude that the isolation requirement used at trigger level does not influence the OS/SS ratio. Hence no further systematic uncertainty is assigned.

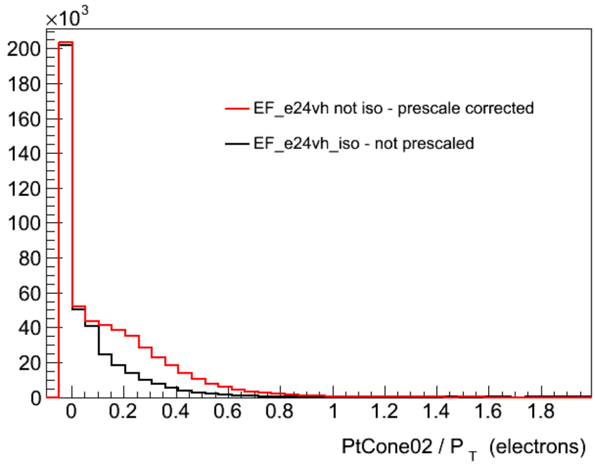

Figure A.1.: p_T(cone) / p_T distribution for the analysis standard trigger and its corrispective without isolation requirement, this second trigger is rescaled according to prescales information.

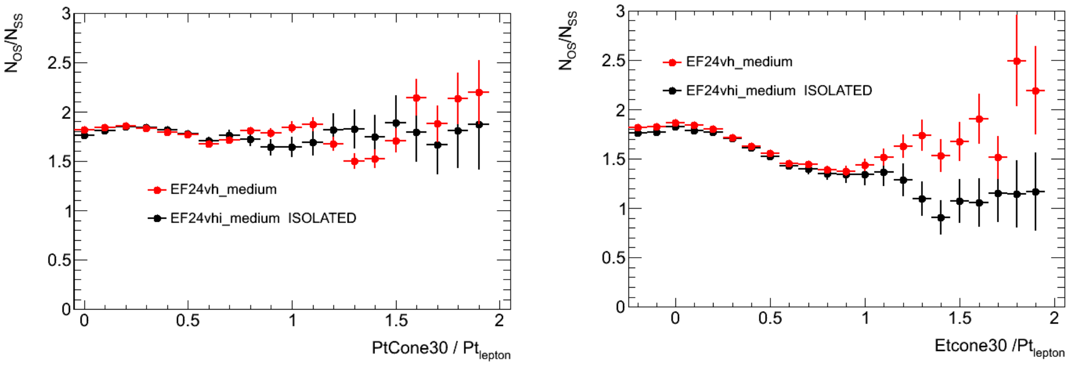

Figure A.2.: R_{QCD} as a function of (a) p_T(cone) / p_T and (b) E_T(cone) /PT for the electron triggers with and without isolation requirement.

A.2. QCD Additional Plots

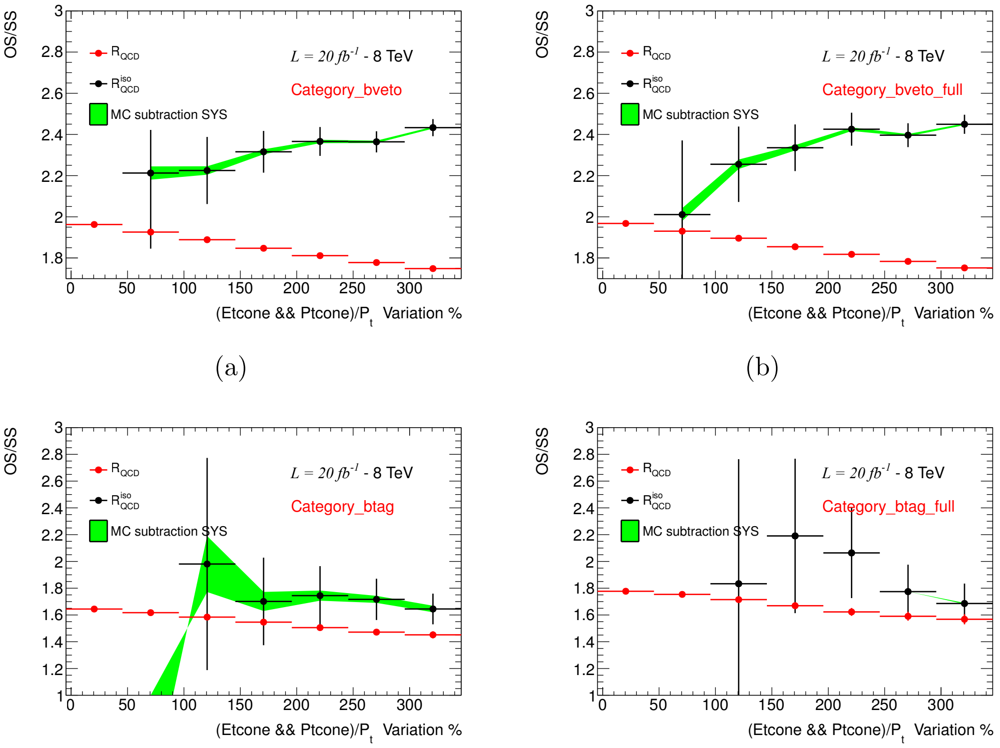

(a) (b)

(c) (d)

Figure A.3.: OS/SS ratio as a function of lepton isolation variable selections after the requirement of (a) zero b-jets, (b) the full b-veto category selection, (c) of a b-jet, (d) the full b-tag category selections. The isolation selections are varied as a percentage relative to the standard lepton isolation cut values (0 in the plot). The red points show the anti-isolated scale factor R_{QCD}, i.e. the ratio between regions C and D. The black points show the isolated SF, which is defined as the ratio between region $\hat{A}$ and $\hat{B}$, where the leptons have isolation values larger than the nominal value but smaller than the sliding cut.

B. Additional Plots and Results

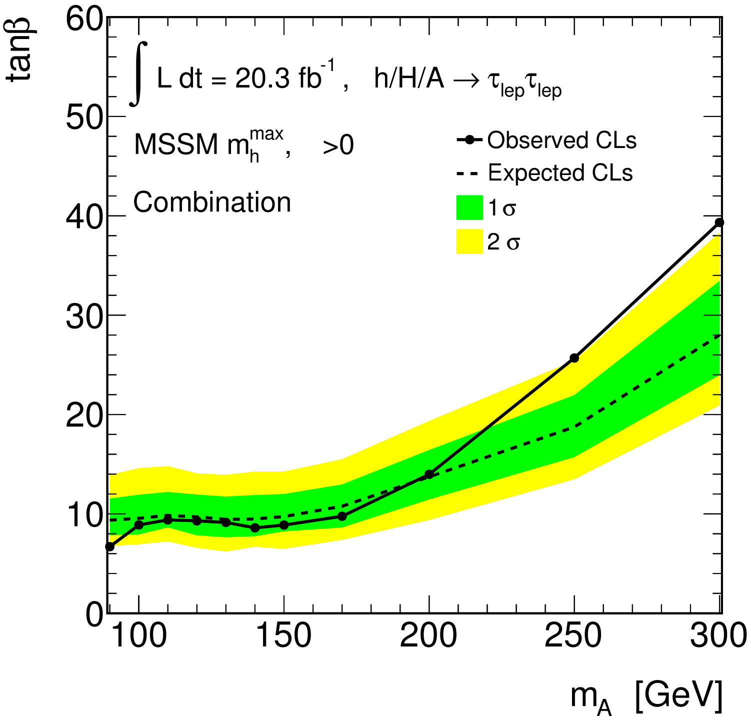

Figure B.1.: Expected and observed exclusion limits at the 95% CL_s confidence-level for MSSM Higgs bosons production interpreted in the $m_A - \tan\beta$ parameter space of the m_h^{max} scenario. Combined result of the b-tagged and b-vetoed category is shown.

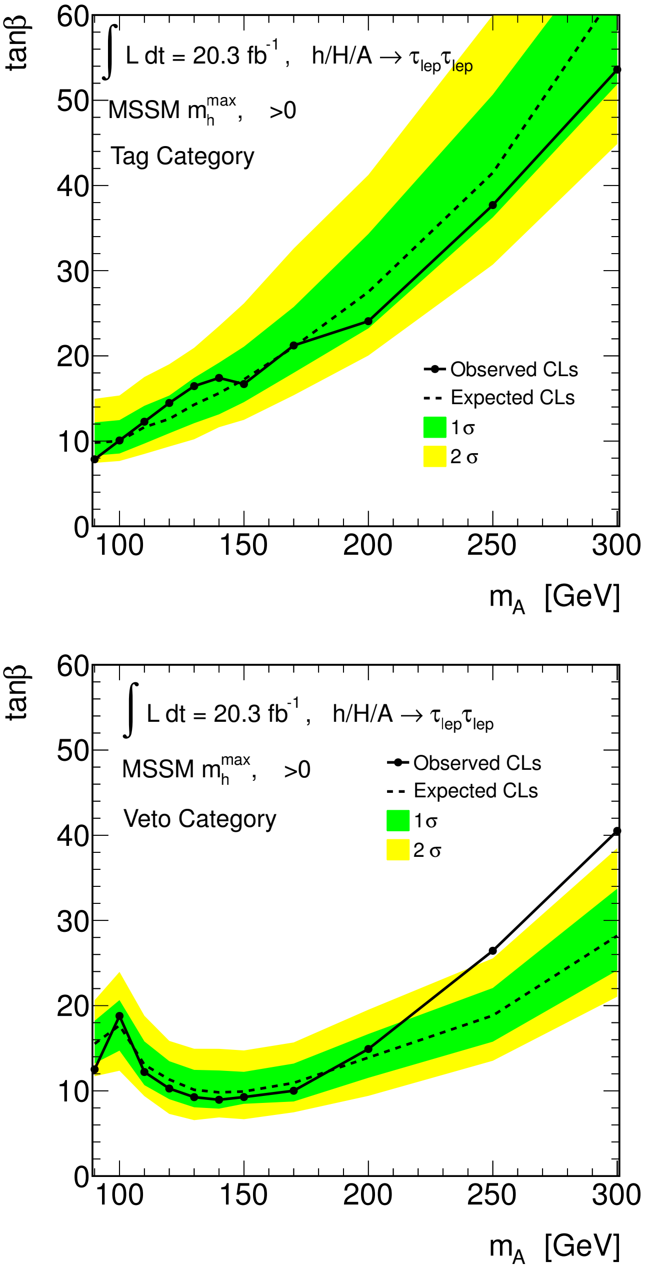

Figure B.2.: Expected and observed exclusion limits at the 95% CL_s confidence-level for MSSM Higgs bosons production interpreted in the $m_A - \tan\beta$ parameter space of the m_h^{max} scenario in the b-tagged (top) and b-vetoed (bottom) category.

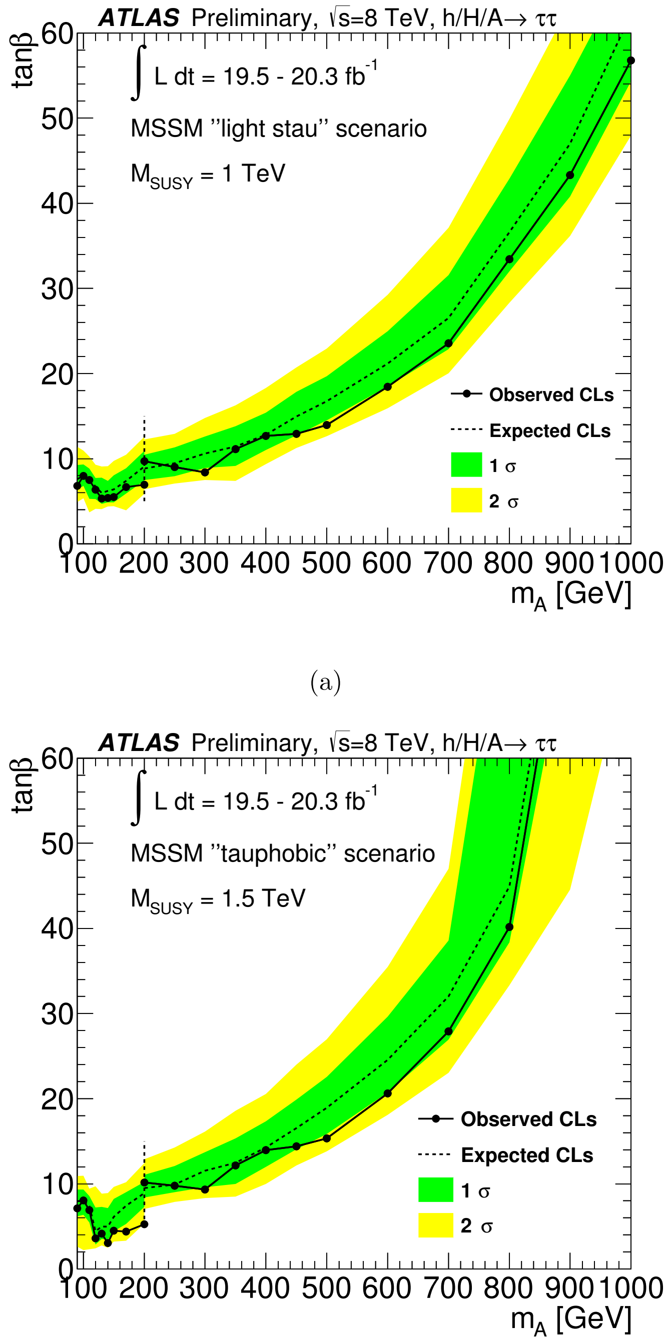

(a)

(b)

Figure B.3.: Expected (dashed line) and observed (solid line with markers) 95% CL upper limits on $\tan\beta$ as a function of m_A. The upper limits are shown in for the statistical combination of all channels in (top) the light stau and (bottom) the tauphobic MSSM benchmark scenarios (see Section 2.3.2). The vertical dashed line at 200 GeV indicates the transition point between low and high mass categories [61].

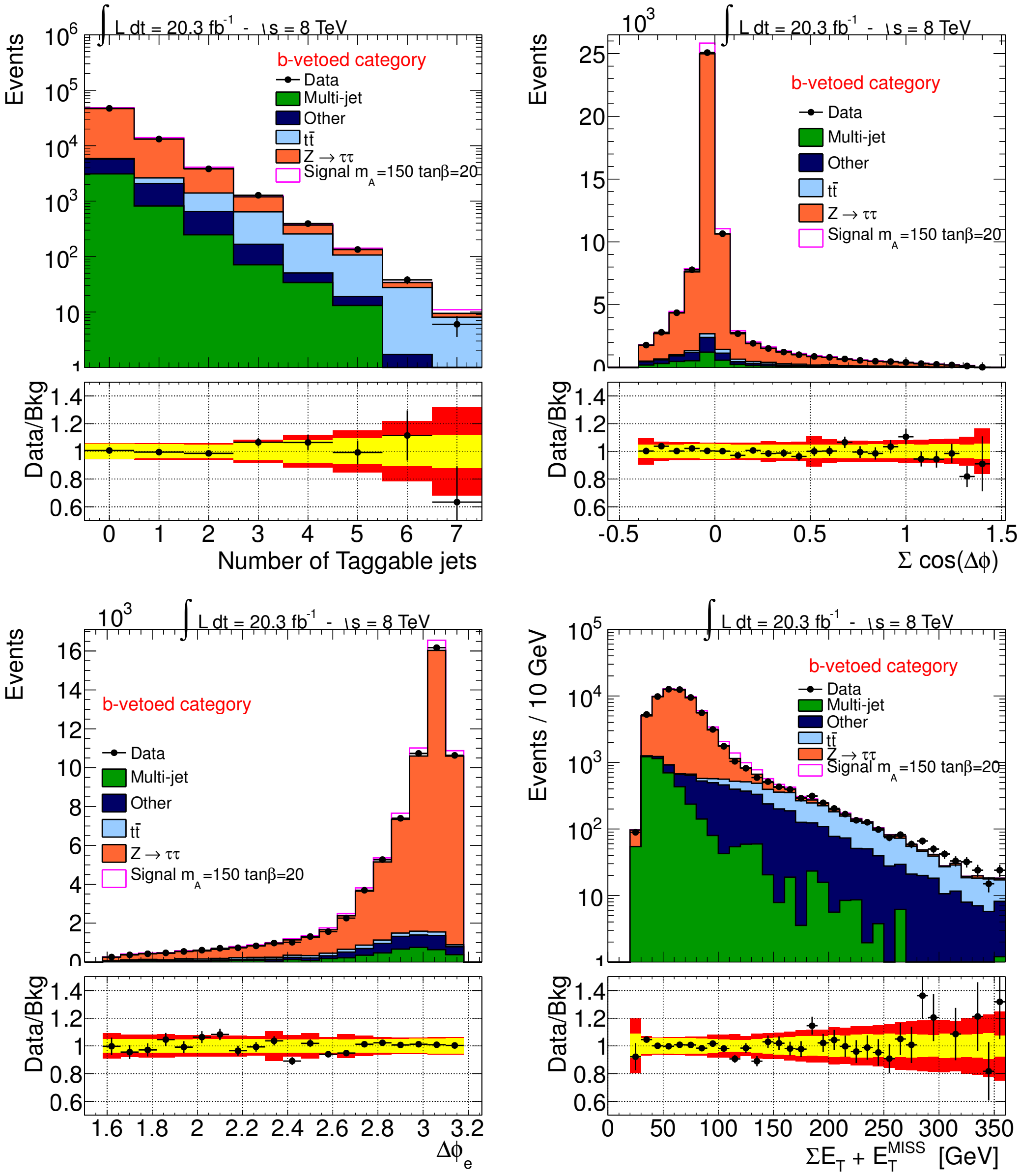

Figure B.4.: Observed and expected distribution for different kinematical variables after full selection of the b-tagged category. In the ratio, the yellow and red band represents the systematic and statistical uncertainty in the background model prediction, respectively, while the error bars respresent the statistical uncertainty of data.

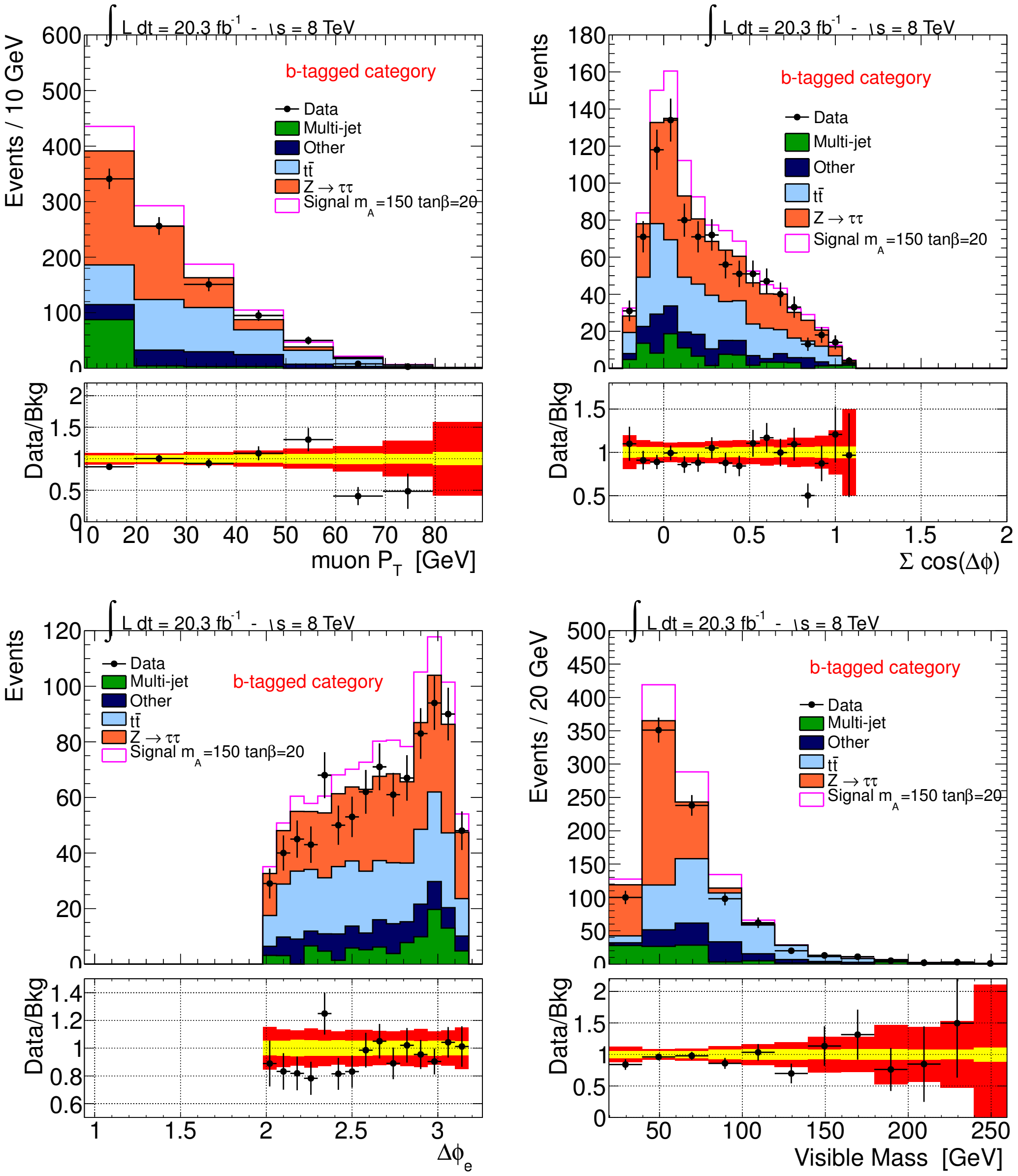

Figure B.5.: Observed and expected distribution fori different kinematical variables after full selection of the b-tagged category. In the ratio, the yellow and red band represents the systematic and statistical uncertainty in the background model prediction, respectively, while the error bars respresent the statistical uncertainty of data.

C. Further Details on Limit

C.1. The ABCD Method

The actual implementation in the limit framework of the ABCD method follows that suggested in [132]. The control data samples B,C and D are considered as additional channels to be statistically combined to two the signal event category. Three free parameters are fitted in B,C and D channels which are: the number of multi-jet events in the data sample B, N_B^{QCD}, the factor R_{QCD} and the factor that extrapolates from isolated to anti-isolated data control samples R_{BD}. Neglecting signal contributions, the following equations can be written for the event yield of the B,C and D control data samples:

$$N_B = N_B^{BKG} + N_B^{QCD}$$

$$N_C = N_C^{BKG} + N_B^{QCD} \times R_{QCD} \times R_{BD}$$

$$N_D = N_D^{BKG} + N_B^{QCD} \times R_{BD}$$

where N^{BKG} represent the prediction of non-QCD background in the relative data samples. The estimate of multi-jet event yield in the signal sample will be then $N_B^{QCD} \times R_{QCD}$. This method is particularly powerful because in the best fit of R_{QCD} the statistical and systematics uncertainty for non-QCD backgrounds and data are considered.

C.2. Shape Systematics

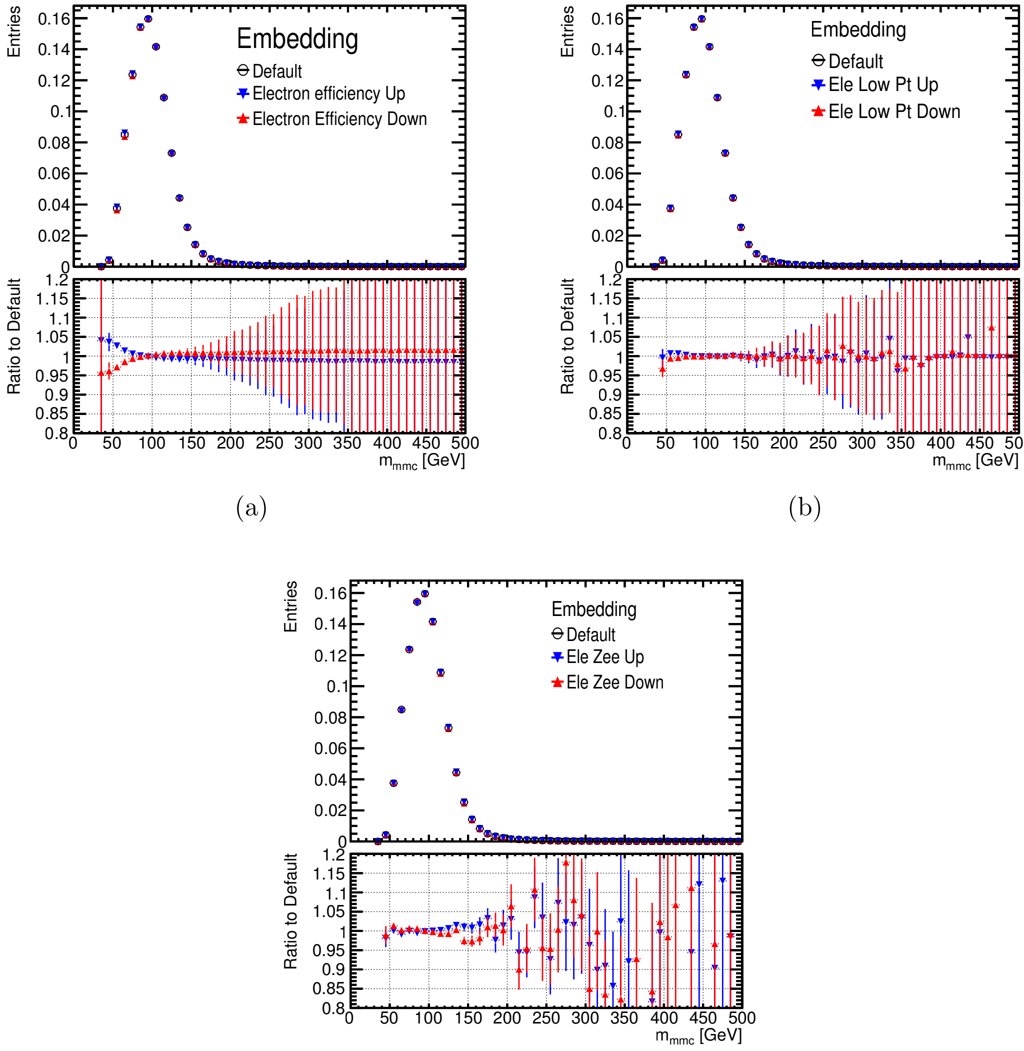

(a)

(b)

(c)

Figure C.1.: Effect on the $m_{\tau\tau}^{MMC}$ distribution of the embedding sample due to the (a) the electron reconstruction and identification systematics, (b) the electron low p_T energy scale systematic and (c) the electron Zee energy scale systematic. The plots are made after the full b-veto category selection. Plots provided by Matthew Backingham.

C.3. Additional Limit Checks

During the limit derivation, the systematic uncertainties (translated in term of nuisance parameter) are fitted to the data, several checks are have been performed to ensure the quality of our statistical model. If some of the nuisance parameters are significantly different from their nominal value (ie before fit), it can be symptomatic of an important mis-modelling and must be carefully scrutinised. Also the correlation between the nuisance parameter and the signal strength (which reflects the degeneracy of the fit) is an important element to keep under control, in fact it reflects how well the data can constraint the nuisance parameters. Finally, to have a feeling of the behaviour of the likelihood at its minimum one can check the negative log likelihood profile in each nuisance parameter direction. We performed all this checks using the package NuisanceCheck-00-00-05 described in [151].

The signal and background model with the signal normalisation free (unconditional fit) is fitted to the data, in the following example plots the signal is assumed for the mass point mA = 120 GeV, tan$\beta = 20$, The difference between the post fit and pre-fit value of the nuisance parameter along with their errors is shown in Figure C.2 for the combination between the two categories. Figure C.3 shows the correlation matrix between the nuisance parameters for the combination between the two channels. Figure C.4-C.6 shows the behaviour of the likelihood at its minimum for each of the nuisance parameters (while a nuisance parameter is investigated the other are kept constant) for the combination between the channels.

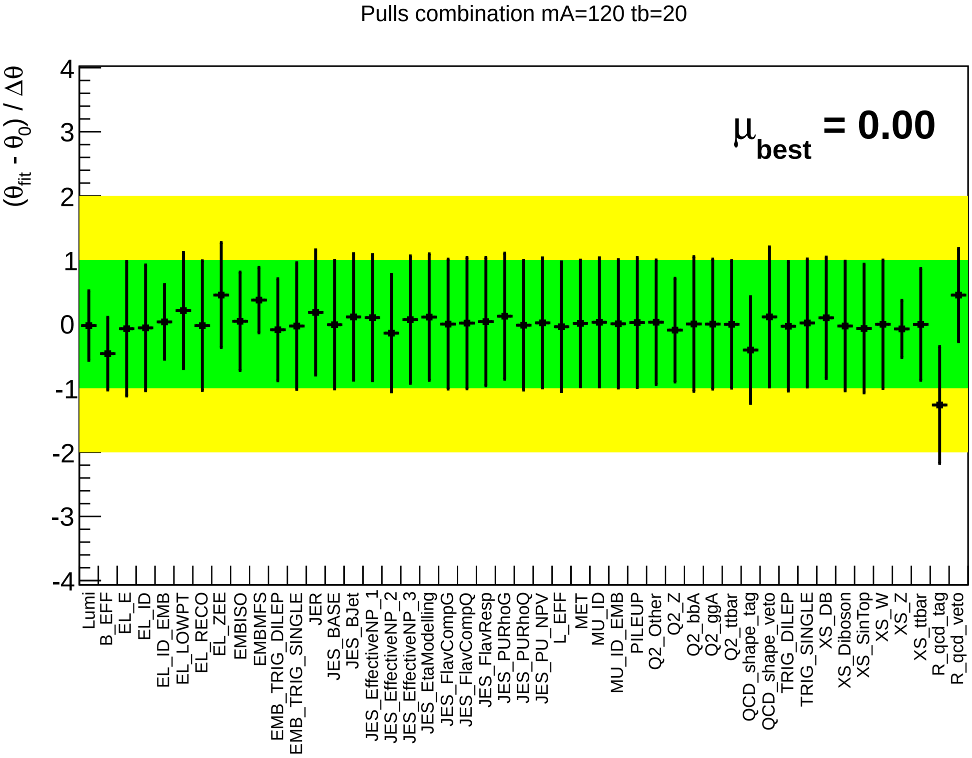

Figure C.2.: Pulls for nuisance parameter considered in the fit, mA = 120 GeV, tanβ = 20, combination between the two channel. These pulls are obtained with NuissanceCheck package, using asymptotic approximation.

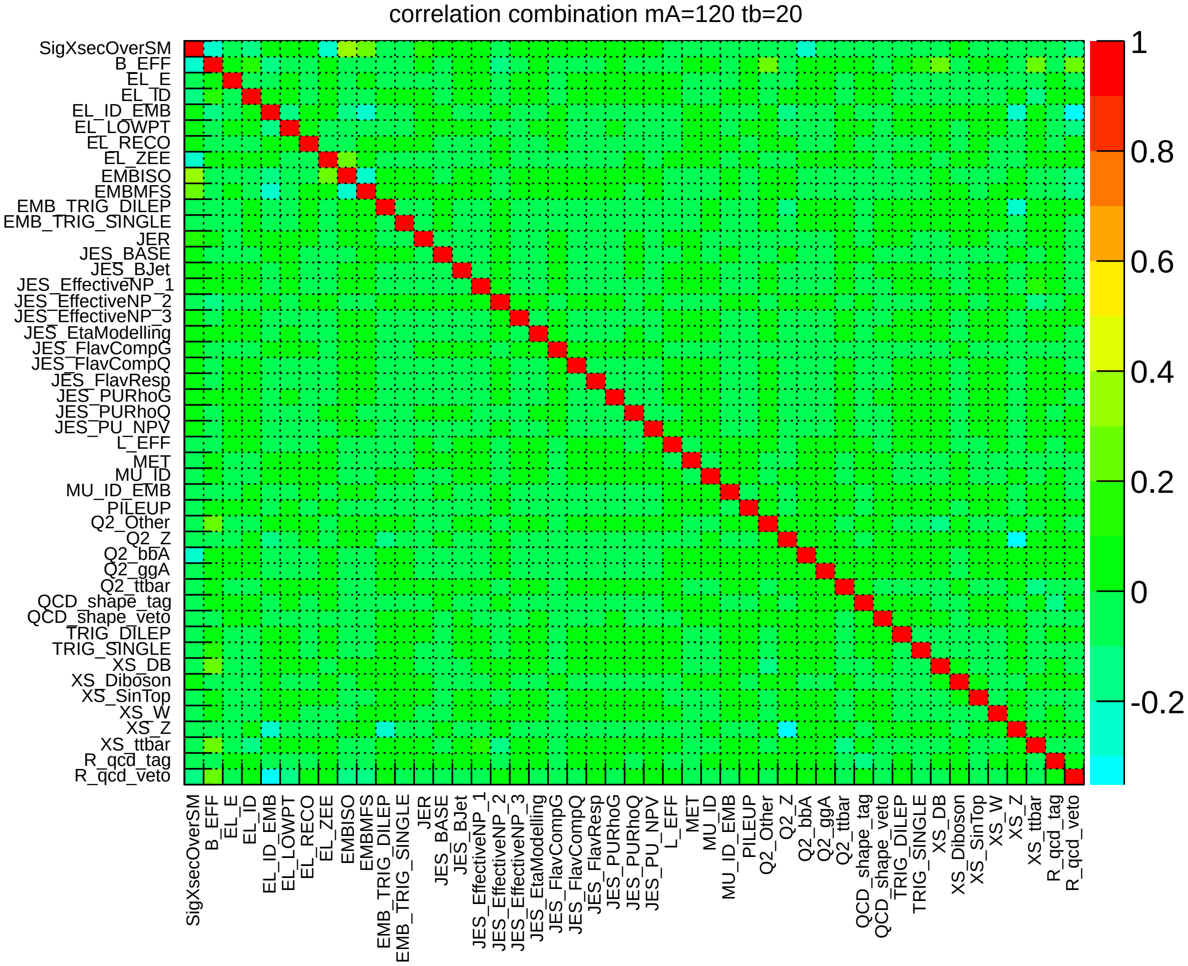

Figure C.3.: Correlation matrix for nuisance parameters considered in the fit. The point mA = 120 GeV and tanβ = 20 is considered for the combination of the b-tag and b-veto channels. This correlation matrix is obtained with NuissanceCheck package, using asymptotic approximation.

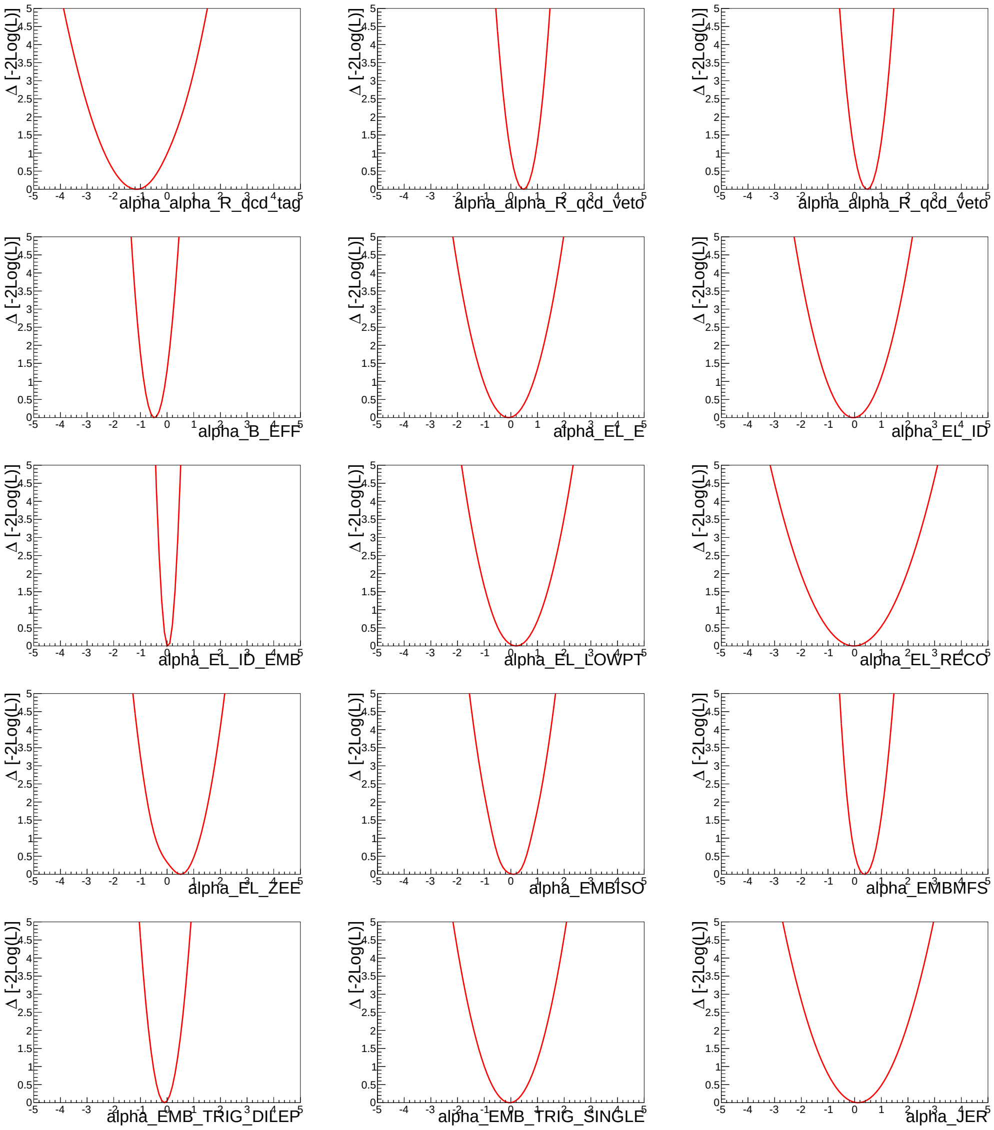

Figure C.4.: Likelihood scans for nuisance parameter considered in the fit, mA = 120 GeV, tanβ = 20, combination between the two channel.

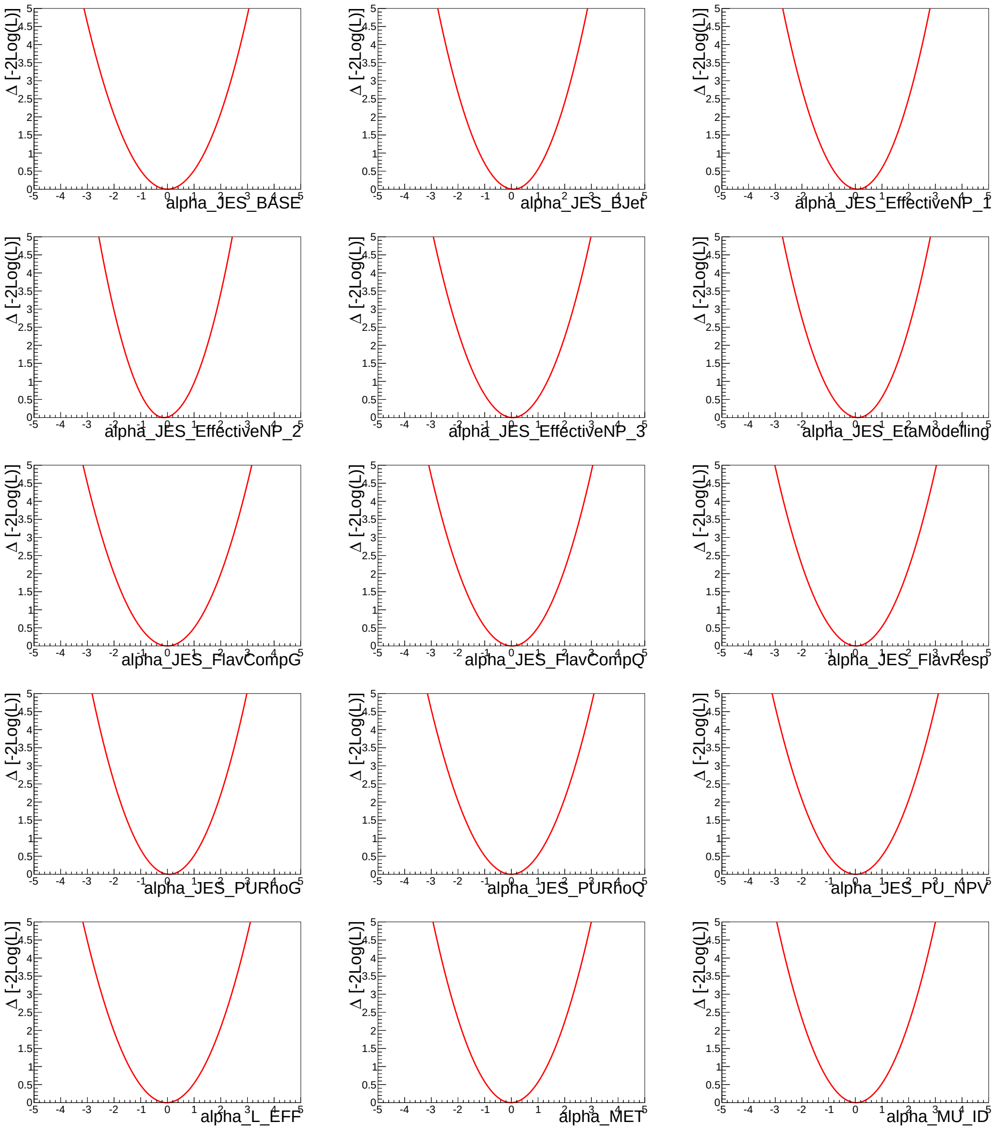

Figure C.5.: Likelihood scans for nuisance parameter considered in the fit, mA = 120 GeV, tanβ = 20, combination between the two channel.

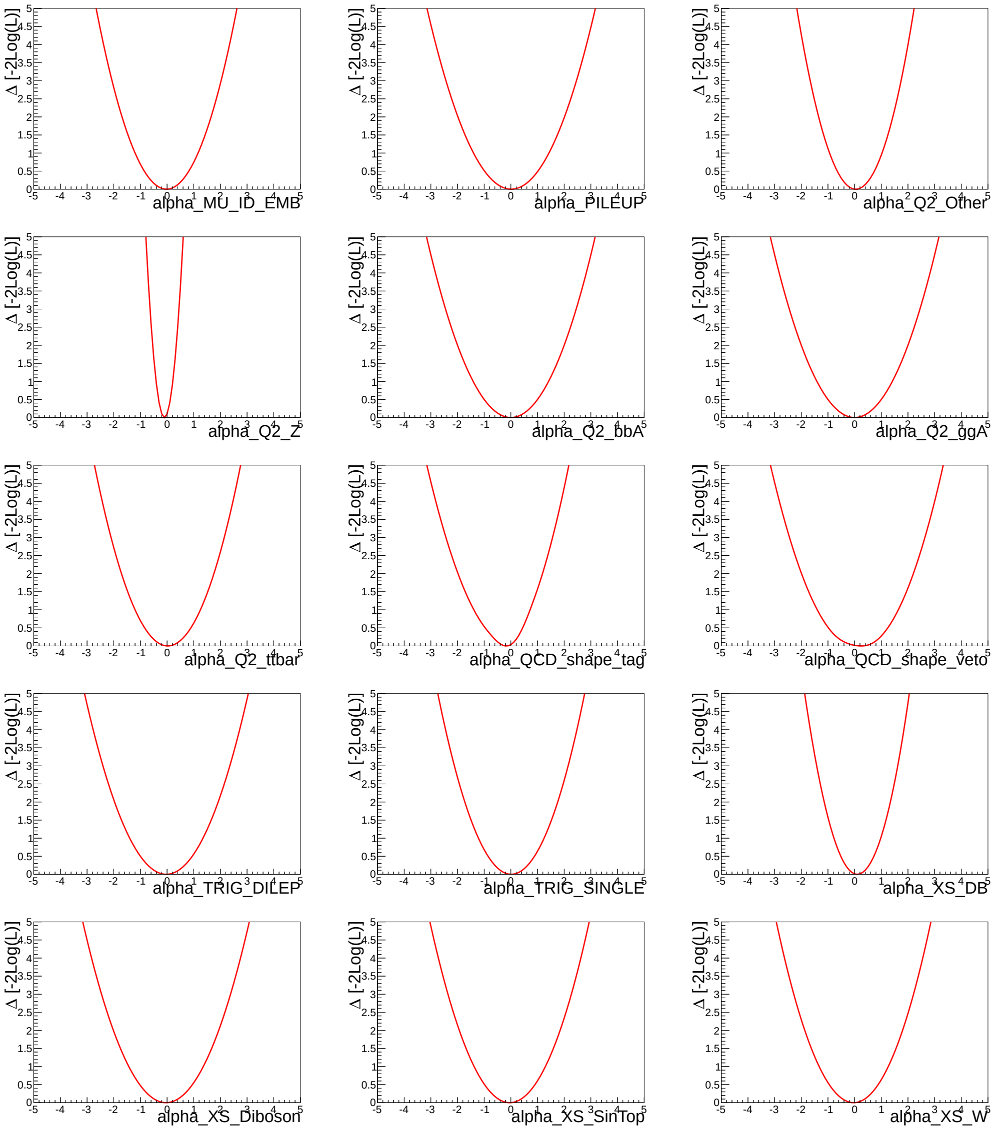

Figure C.6.: Likelihood scans for nuisance parameter considered in the fit, mA = 120 GeV, tanβ = 20, combination between the two channel.

C.3.1. Regularization of Signal Samples

In the b-tag channel of this analysis, it is observed that the MC prediction of the signal yield has a relatively large statistical uncertainty. This, in turn, leads to statistical fluctuations on the expected limits derived from the b-tag channel. To counteract this effect, the signal yield at each mass point is rescaled using a fourth order polynomial fitted to the uncorrected signal yields as a function of the mass m_A. The rescaled yeilds ar then used for both the cross section independent limits and those interpreted within the MSSM. Figure C.7 shows the uncorrected event yields as a function of m_A, normalised using a cross section of 1 pb. The red line shows the result of the fourth order polynomial fit to the signal yields. While the fit to the b-associated production signal yield leads to a smoothly varying function, the fit to the gluon fusion production yields is less so. However, since events from this production mode only have a small contribution to the total expected signal in the b-tag channel, the shape of this correction as a function of mA does not affect the final limits.

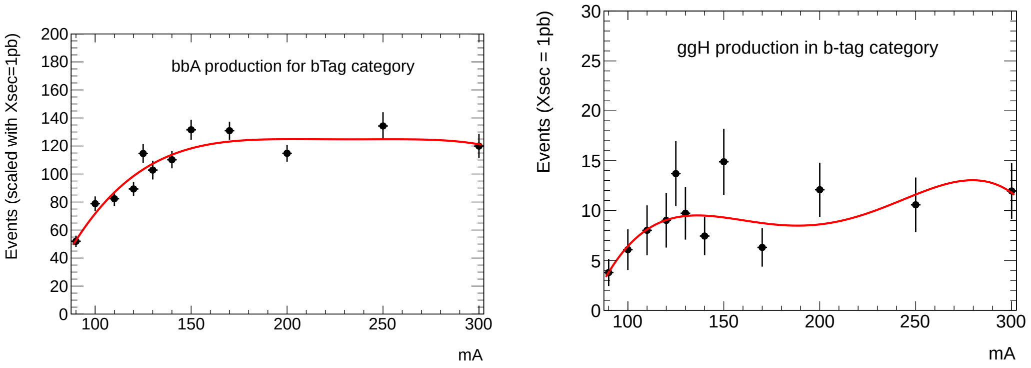

Figure C.7.: Fit of the uncorrected event yield for different mass points for the signal produced via b-associate production (top) and gluon-fusion (bottom) for the b-tag category. Each mass point is normalised using a signal cross section of 1 pb.

C.3.2. Pre Fit and Post Fit MMC mass Plots

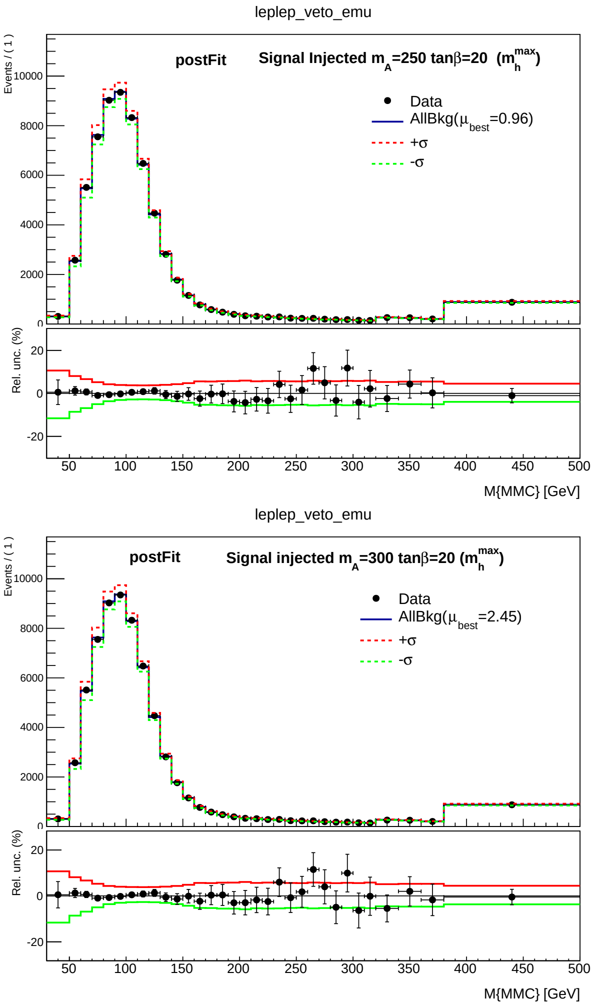

Figure C.8.: Post-fit $m_{\tau\tau}^{MMC}$ mass distribution for the veto category final selections. A signal is injected with $m_A = 250$ (top) and $m_A = 300$ (bottom) for $\tan\beta = 20$ assuming m_h^{max} scenario. The 1σ bands represent the statistical and systematic uncertainties.

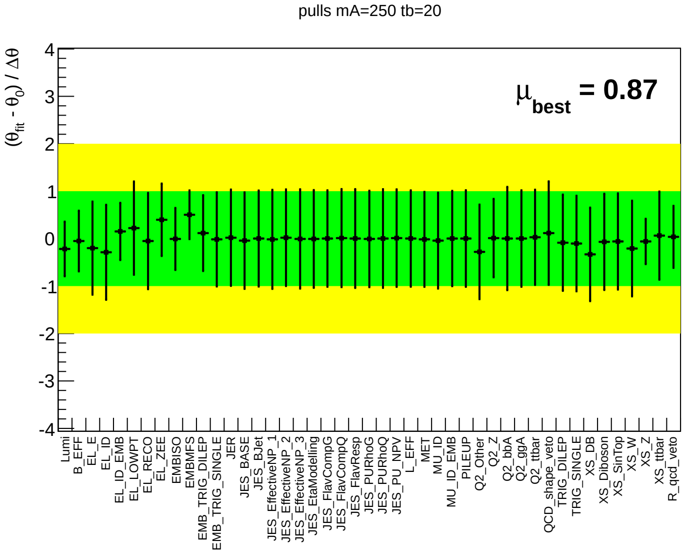

Figure C.9.: Pulls for unconditional fit for the b-veto category. A signal is injected with $m_A = 250$ and $\tan\beta = 20$ assuming m_h^{max} scenario. The pulls are obtained with NuissanceCheck package.

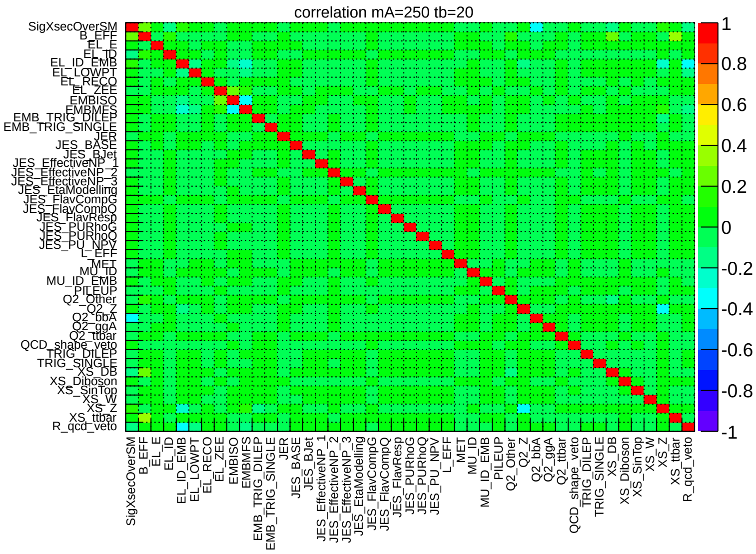

Figure C.10.: Correlation matrix for unconditional fit for the b-veto category. A signal is injected with $m_A = 250$ and $\tan\beta = 20$ assuming m_h^{max} scenario. The pulls are obtained with NuissanceCheck package.

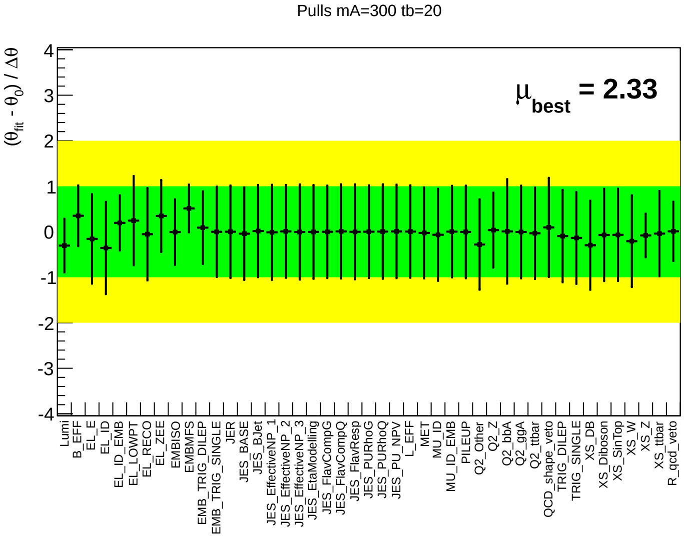

Figure C.11.: Pulls for unconditional fit for the b-veto category. A signal is injected with $m_A = 300$ and $\tan\beta = 20$ assuming m_h^{max} scenario. The pulls are obtained with NuissanceCheck package.

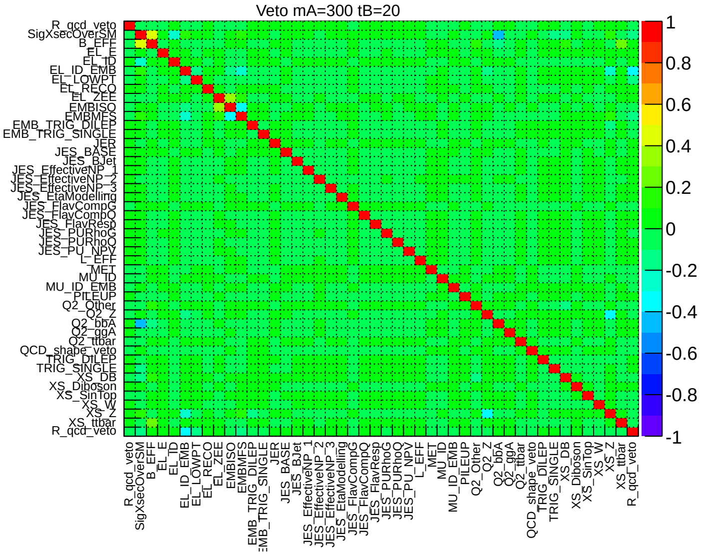

Figure C.12.: Correlation matrix for unconditional fit for the b-veto category. A signal is injected with $m_A = 300$ and $\tan\beta = 20$ assuming m_h^{max} scenario. The pulls are obtained with NuissanceCheck package.

C.3.3. Checks in Mass range 230-300 GeV

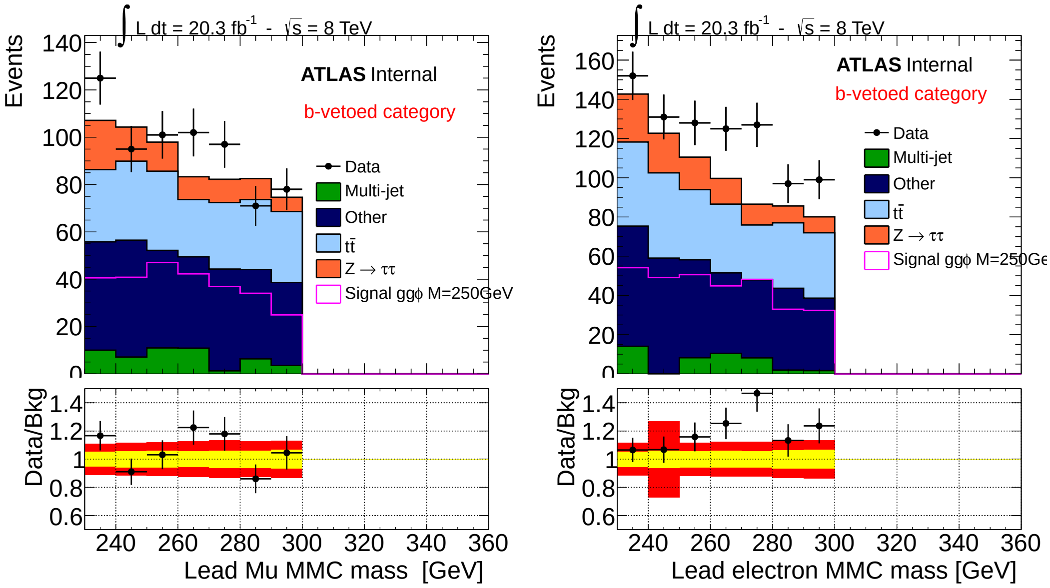

Figure C.13.: Pre-fit distribution of $m_{\tau\tau}^{MMC}$ mass for the veto category final selections. A mass vindow selection is applied selecting only the mass range $230 < m_{\tau\tau}^{MMC} < 300$ GeV. The case of muon or electron being the leading lepton are shown separately. A signal is injected assiuming gluon fusion production of a scalar boson ϕ with mass $m_\phi = 250$ GeV, its cross section is normalized to 2.4×5 *pb*. Since electron fakes are more likely than muon fakes, in case of W boson mismodeling an excess is expected in the distribution of leading muon events.

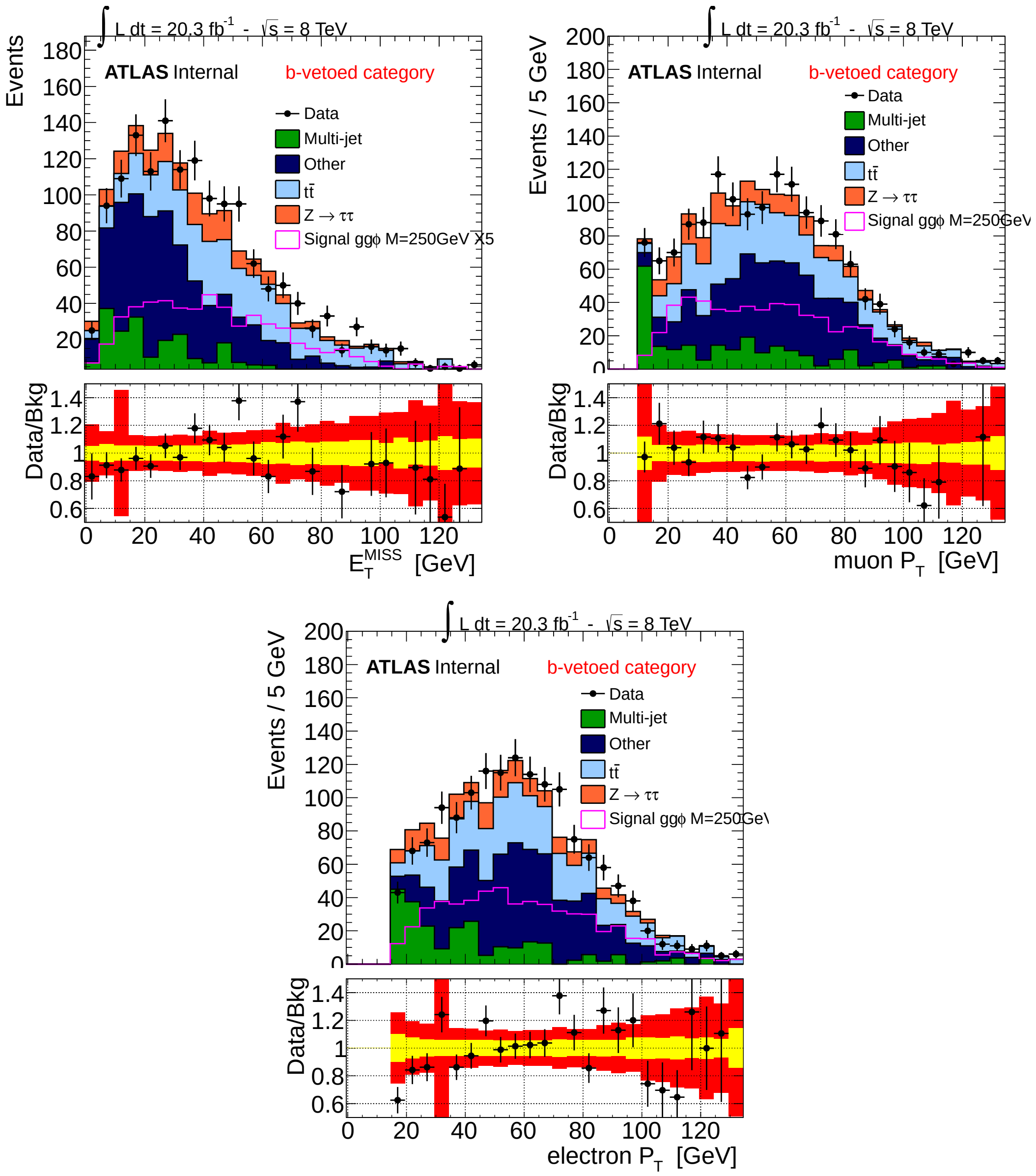

Figure C.14.: Pre-fit distribution of different kinematic variables for the veto category final selections. A mass vindow selection is applied selecting only the mass range $230 < m_{\tau\tau}^{MMC} < 300$ GeV. A signal is injected assiuming gluon fusion production of a scalar boson ϕ with mass $m_\phi = 250$ GeV, its cross section is normalized to 2.4×5 *pb*.